Characterisation and Analysis of an Open-loop Ground Source Heating System

Timothy M.A. Delport

Magdalen College

University of Oxford

A thesis submitted for the degree of

Doctor of Philosophy

Hilary 2022

Declaration of Authorship

I, Timothy M.A. Delport, declare that this thesis, titled "Characterisation and Analysis of an Open-loop Ground Source Heating System" and the work presented in it are my own. I hereby certify that the work presented in this project is all my own unaided work and that all material obtained from published or unpublished sources of any type, including the internet, have been fully acknowledged at the proper point in the text and included in the list of references.

Signed: 

Date: 14/05/2022

Acknowledgements

I am sincerely grateful for the supervision and intellectual direction I received during my DPhil studies from Prof. Christopher MacMinn and Dr. Luke Jenkins. Through my years of writing this thesis, I have found the thermogeological and hydrogeological industry to be full of wonderful people, many who share the common pursuit of furthering knowledge, sustainable practise and seeing renewable technology flourish. Thanks to those professionals who lent me their time, support, projects and experience – Dr. David Birks, Dr. David Banks, Michael Woods and Dr. John Barker.

Both with me and next to me through my Oxford journey has been my loving family – Michael Delport, Vicki Delport and Michelle Delport – my mates – Dr. Spencer Klavan, Dr. Timothy Vangsness, James McCouat, Tom Paine, Joe Sibley, Tom Trott, Sam Greenrod and Jeff Peo – my supportive girlfriend, Holly Keevil, and her family – David and Anna Keevil. A special mention to Dr. Spencer Klavan, Abhimangyu Arni for our shared love of scotch whisky – many a late-night conversation and dram served to replenish the coffers, before striking once more at the books the next day.

I am blessed to have had extraordinary mentors who have given me their time and support, without any official obligation, to inspire, mould, direct and challenge my intellectual, emotional and character-based journeys. I owe so much to Prof. David Williams, who gave an undeserving undergraduate the 'first break' they needed, followed by continued advocacy. David is joined by Prof. Jose Torero, Dr. Robert Day, Dr. Peter Chapman, Hon. John Anderson, and Mark Rasi.

I count myself privileged to have had the responsibility of being a Junior Dean of St Edmund Hall – a community I hold in such high regard, and whom have been integral in my journey at Oxford. The mentorship, friendship and camaraderie of two excellent college deans – Prof. Nicholas Davidson and Prof. Jonathan Yates – my outstanding fellow Decanal colleagues – Dr. Amber Gartrell, Abhimanyu 'Abni' Arni, Katie Mellor, and Ella Buys – and the entire St Edmund Hall staff, is dear to me.

Acknowledgement goes to the General Sir John Monash Foundation and Wesfarmers, whose support fundamentally made this thesis possible. Thanks to the many institutions and those within that have supported, trained, and no doubt sometimes endured me along my journey thus far as an engineer, intellectual and simply a person – The University of Queensland, Golder Associates, BHP BMA,

Red Earth Engineering, WSP UK & ANZ (in particular, the Newcastle team), hyperTunnel Ltd., and Magdalen College Oxford.

Finally, this thesis benefited from the continuation of a research agreement first established between Dr. David Birks and Hilton Wells of the Southbank Institute. We extend our gratitude to Mr. Wells and the Southbank Institute for their openness to permit these studies and hope that they have a positive impact on the field of open-loop GSHS.

Abstract

Open-loop ground source heating systems (GSHS) provide cooling and heating to a space with several positive sustainable and economical factors over fossil-fuel-based alternatives. The worldwide number of GSHS is increasing but they remain relatively rare compared to alternatives. Therefore the overall GSHS industry might still be considered young in its GSHS-specific experience of testing, design and modelling practises. Characterisation and analysis of an operational system, in light of past design assumptions, modelling and testing practices, remains a novel opportunity to provide key insights and learnings. Several studies have been conducted into the testing and operational performance of an open-loop GSHS. Historical operational data showed thermal fluctuations at an abstraction well in advance of predicted thermal breakthrough times. An explanation of these occurrences was sought by evaluating prior testing and modelling assumptions. Models were constructed to evaluate pump and tracer testing data, calibrating hydraulic and solute-transport properties of the host aquifer. Calibration of the thermal transport properties, not previously conducted, was pursued through isolating an early thermal event and several years of operational data. Work identified differing hydraulic and transport properties to those previously assumed in design. The significance and sensitivity of free parameters in each model variant was evaluated. Re-calibrated properties yielded inconclusive results; attributing thermal fluctuations to either regional groundwater temperature fluctuations (reinforcing earlier predictions that thermal breakthrough was not yet expected) and/or earlier than expected thermal breakthrough. Calibration efforts highlighted the importance of comprehensive testing and instrumentation to support design and modelling efforts — namely, careful consideration and increased density of sensor placement, along with geophysical investigation of down-hole well properties. Modelling of open-loop GSHS operational strategies (unidirectional and seasonally reversed) was conducted to provide quantitative support to the naive intuitive benefits of the latter. A seasonally reversed strategy was found to outperform unidirectional modes considering varying injection temperature, peak energy loads and seasonal imbalances in operation. Furthermore, the superior performance in both energy efficiency and predicted design life was observed without permitting the system to be responsive to detected thermal stores. A responsive seasonally reversed system is expected to further outperform its unidirectional counterpart.

Contents

List of Abbreviations

1D or 2D . . . One- or two-dimensional, referring in this thesis to spatial dimensions.

ATES . . . . . Aquifer thermal energy storage

BGS . . . . . British Geological Survey

BH1 or BH2 . Well identification for borehole 1 or borehole 2

CDF . . . . . Cumulative density function

CRT . . . . . Constant-rate test

DF . . . . . Darcy-Forchheimer

DR . . . . . Drift (geological unit)

EC . . . . . English Chalk (geological unit)

FVM . . . . . Finite volume method

GSHS . . . . . Ground source heating system. Also referred to as an ground source heat/heating pump (GSHP)

K-S . . . . . Kolmogorov–Smirnov

LC . . . . . London Clay (geological unit)

LTE . . . . . Local thermal equilibrium

LTNE . . . . . Local thermal non-equilibrium

MG . . . . . Made ground (geological unit)

ODE . . . . . Ordinary differential equation

PDE . . . . . Partial differential equation

RFH . . . . . Royal Festival Hall, London.

RTG . . . . . River Terrace Gravels (geological unit)

SDT . . . . . Step-drawdown test

TS . . . . . Thanet Sands (geological unit)

WRB . . . . . Woolwich and Reading Beds (geological unit)

List of Symbols

A . . . . . [L^2] Area

a . . . . . [L] Aperture of fracture

a_D . . . . . [-] Dispersion/Conductive factor

a_r . . . . . [-] Load reduction factor

α_{hydro} . . . . . [L^2T^{-1}] Hydraulic diffusivity

α_L . . . . . [L] Longitudinal dispersivity

α_T . . . . . [L] Transverse dispersivity

b . . . . . [L^{-1}] Forchheimer parameter

b_{BH1} . . . . . [L^{-1}] Forchheimer parameter associated with BH1

b_{BH2} . . . . . [L^{-1}] Forchheimer parameter associated with BH2

c . . . . . [ML^{-3}] Solute concentration

c_0 . . . . . [ML^{-3}] Initial/baseline solute concentration

c_s . . . . . [ML^{-3}] Solute concentration of rock surface sorption

c_w . . . . . [ML^{-3}] Solute concentration in fracture fluid

$c_{w,inj}$, $c_{w,abs}$ . . [ML^{-3}] Solute concentration of injected or abstraction fluid

$c_{w,o}$ . . . . . [ML^{-3}] Observed solute concentration in fracture fluid

$c_{w,s}$ . . . . . [ML^{-3}] Simulated solute concentration in fracture fluid

C_m . . . . . [$L^2\Theta^{-1}T^{-2}$] Specific heat capacity of rock matrix

C_w . . . . . [$L^2\Theta^{-1}T^{-2}$] Specific heat capacity of water

C_s . . . . . [$L^2\Theta^{-1}T^{-2}$] Specific heat capacity of solid rock

D_0 . . . . . [L^2T^{-1}] Solute diffusivity (molecular)

D_m . . . . . [L^2T^{-1}] Thermal diffusivity of rock matrix

D_s . . . . . [T^{-1}] Sorption coefficient

D_w . . . . . [L^2T^{-1}] Thermal diffusivity of fracture fluid

ΔT . . . . . [Θ] Design injection temperature

ΔT_a . . . . . [Θ] Available temperature difference

ΔT_{max} . . . . . [Θ] Maximum permitted change in temperature

E . . . . . [$\mathrm{ML^2T^{-3}}$] Power load

E_p . . . . . [$\mathrm{ML^2T^{-3}}$] Peak power load

e . . . . . [Θ] Temperature

e_0 . . . . . [Θ] Initial/baseline temperature

e_m . . . . . [Θ] Temperature of rock matrix

E_{total} . . . . . [$\mathrm{ML^2T^{-2}}$] Total energy injected

e_w . . . . . [Θ] Temperature of fracture fluid

$e_{w,inj}$, $e_{w,abs}$ . . [Θ] Temperature of injected or abstracted fluid

ϵ^{abs} . . . . . Absolute difference

$\left\langle \epsilon^{abs} \right\rangle$ . . . . . Mean absolute difference

ϵ^{rel} . . . . . [%] Relative difference

$\left\langle \epsilon^{rel} \right\rangle$ . . . . . [%] Mean relative difference

η . . . . . [-] Thermal efficiency

f . . . . . [$\mathrm{L^{-1}}$] Fracture frequency

g . . . . . [$\mathrm{LT^{-2}}$] Force per unit mass due to gravity

Γ . . . . . [$\mathrm{ML^{-1}T^{-3}\Theta^{-1}}$] Fluid-to-rock thermal exchange coefficient

H . . . . . [L] Thickness of an aquifer layer

H_B . . . . . [L] Thickness of matrix block

H_{EC} . . . . . [L] Thickness of English chalk aquifer layer

H_{TS} . . . . . [L] Thickness of Thanet Sands aquifer layer

H_{WRB} . . . . . [L] Thickness of Woolwich and Reading Beds aquifer layer

$\mathcal{I}$ . . . . . Source/sink term for solute or thermal energy

k . . . . . [$\mathrm{L^2}$] Permeability

k_h . . . . . [$\mathrm{L^2}$] Horizontal permeability

k_v . . . . . [$\mathrm{L^2}$] Vertical permeability

L_{BH} . . . . . [L] Distance between wells

L_x . . . . . [L] Size of domain in the x direction

L_y . . . . . [L] Size of domain in the y direction

λ_m . . . . . [$\mathrm{MLT^{-3}\Theta^{-1}}$] Thermal conductivity of rock matrix

λ_s . . . . . [$\mathrm{MLT^{-3}\Theta^{-1}}$] Thermal conductivity of solid rock

λ_w . . . . . [$\mathrm{MLT^{-3}\Theta^{-1}}$] Thermal conductivity of water

M_{inj} . . . . . [M] Mass of solute injected

μ . . . . . [$\mathrm{ML^{-1}T^{-1}}$] Dynamic viscosity of water

n . . . . . Normalised parameter value with respect to parameter range

N_r . . . . . [-] Discrete points in r direction

N_t . . . . . [-] Discrete intervals in time

N_x . . . . . [-] Discrete points in x direction

N_y . . . . . [-] Discrete points in y direction

p . . . . . [$\mathrm{ML^{-1}T^{-2}}$] Fluid pressure at aquifer datum

p_0 . . . . . [$\mathrm{ML^{-1}T^{-2}}$] Initial/baseline fluid pressure at aquifer datum

p_w . . . . . [$\mathrm{ML^{-1}T^{-2}}$] Fluid pressure within well at aquifer datum

ϕ . . . . . [-] Material porosity

ϕ_e . . . . . [-] Effective porosity or porosity attributed to fracture network

ϕ_m . . . . . [-] Porosity of rock matrix

ϕ_r . . . . . [-] Porosity attributed to intact rock mass

ϕ_s . . . . . [-] Porosity attributed to rock surface sorption

$\hat{Q}$ **or** Q_{id} . . . . [$\mathrm{L^3T^{-1}}$] Applied well flowrate

q . . . . . [$\mathrm{LT^{-1}}$] Flux

q_r . . . . . [$\mathrm{LT^{-1}}$] Radial flux

$q_{r,DF}$ . . . . . [$\mathrm{LT^{-1}}$] Darcy-Forchheimer flux

$q_{r,ss}$ . . . . . [$\mathrm{LT^{-1}}$] Steady-state radial flux

q_z . . . . . [$\mathrm{LT^{-1}}$] Vertical flux (normal to plane of horizontal aquifer)

r . . . . . [L] Radial distance

r_∞ . . . . . [L] Radial distance to computation boundary

r_c . . . . . [L] Radius of well casing

r_w . . . . . [L] Effective well radius

ρ . . . . . [$\mathrm{ML^{-3}}$] Density

ρ_m . . . . . [$\mathrm{ML^{-3}}$] Density of rock matrix

ρ_s . . . . . [$\mathrm{ML^{-3}}$] Density of solid rock

ρ_w . . . . . [$\mathrm{ML^{-3}}$] Density of fluid

S	[-] Aquifer storativity
s_w	[L] Well drawdown
$s_{w,o}$	[L] Observed well drawdown
$s_{w,s}$	[L] Simulated well drawdown
T	[L^2T^{-1}] Transmissivity of aquifer layer
t	[T] Time
$\bar{t}$	[T] Total time
t_f	[T] Failure time
t_{inj}	[T] Duration of injection
x,y,z	Spacial coordinates (horizontal, horizontal and vertical, respectively)

1 Introduction & Background

Contents

This thesis was motivated by a keen interest in open-loop ground source heating/cooling systems (GSHS) and their potential contribution to the heating and cooling needs of a society diverging from fossil-fuel dependency. Understanding these systems as they evolve is crucial to their continued and increased use, as is exploring methods to improve their sustainability and reliability.

1.1 Introduction

This section briefly introduces the concept of an open-loop GSHS, including their design, testing, modelling and operation. The study is predominantly focused on the subsurface evolution of an open-loop GSHS, and as such will not discuss the specifics of surface-based infrastructure (e.g., heat exchangers, building configurations).

1.1.1 GSHS

A ground source heating system (GSHS), or ground source heat pump (GSHP), is a type of geothermal system used to provide heating and/or cooling to an indoor space. A GSHS does not produce electricity, but is considered geothermal as it uses the latent heat of the ground as a resource. The scale of GSHSs varies from systems used for a single house or property to those servicing networks of buildings and homes.

Two general configurations of GSHS exist: closed-loop and open-loop. In a closed-loop system, a mixture of water and anti-freeze ('working fluid') circulates a closed network of pipes. The pipes can be buried or drilled into the ground, or alternatively might be placed in a body of water (e.g., pond, lake or river). Heat exchange occurs between the working fluid and the surrounding medium across the walls of the pipe. The working fluid never comes into direct contact with the surrounding medium, hence the loop is 'closed'.

In an open-loop GSHS, groundwater is taken from an aquifer (or body of water) and provided to the heat pump as the thermal source. The heat pump exchanges heat with the fluid, altering its temperature, and then the groundwater is returned to the aquifer or discharged elsewhere. An open-loop system is considered more economical for heating and cooling loads over 100 kW, since closed-loop is restricted by conduction and therefore requires increasing lengths of pipes to meet higher loads (Vourvoulias, 2022).

The temperature of the ground and its groundwater are relatively stable throughout the year at depths below approximately 10 m (Busby, 2015). However, in many urban settings the temperature of the ground and its groundwater can be influenced by the sealing of surfaces and heat losses from subsurface infrastructure. The natural temperature gradient of the ground and groundwater increases by approximately 2–3 °C per 100 m of depth (Pollack, Hurter, and Johnson, 1993; Dickson and Fanelli, 2013). Ground temperature mapping indicates subsurface (10–150 m) temperatures in the United Kingdom in the range of 9–14 °C (Busby, 2015). At these temperatures, open-loop systems can abstract fluid that is generally

colder than the ambient air during summer and warmer than the ambient air in winter. An open-loop GSHS uses these temperature differences to heat and/or cool.

This thesis focuses on an open-loop GSHS built in London. London ambient air temperatures fluctuate from an average daily temperature of 4.8 °C in January (winter) to 17.8 °C in July (summer), with an expected minimum of 2.1 °C and maximum of 21.8 °C (Data.org, 2022). As a result, a London-based systems performs cooling from April to September and heating from October to March.

Since an open-loop GSHS exchanges heat with the environment, they must be designed with environmental impact in mind. To avoid icing during winter, which can lead to damage and loss of functionality, fluid discharge temperatures are typically restricted to above 4–6 °C. In summer, the Environmental Agency limits discharge temperatures to below 25 °C (or no more than 8 °C above ambient groundwater temperature) due to the potential negative environmental impacts of hot effluent fluid (Environment Agency, 2011). The total quantity of fluid that can be sourced is also restricted by the Environmental Agency, in an effort to responsibly manage natural resources (Fry, 2009). Fry (2009) provides a detailed account of the practical considerations and licensing requirements of an open-loop GSHS in London.

To construct and operate an open-loop GSHS, investigation and testing must first be conducted to evaluate the presence and abundance of the intended thermal source. This informs designers whether the available source of groundwater will be able to meet the energy requirements of the proposed heat pump configuration.

1.1.2 Investigation, Testing and Characterisation

The commissioning of an open-loop GSHS goes through several stages of investigation, testing and characterisation. Ideally, these stages should at least include:

1. A desktop study to evaluate the preliminary feasibility,
2. Drilling, geophysical and geotechnical investigation,
3. Pump testing and hydrogeological characterisation,
4. Tracer testing and solute transport characterisation, and

5. Operational modelling.

Each of these stages are discussed below with respect to an open-loop GSHS well doublet (a GSHS system consisting of two wells in an aquifer).

Desktop study

To first establish whether the resource required for an open-loop GSHS is available at a given location, a desktop study is performed. The desktop study is interested in confirming that groundwater exists, at what depth it exists, whether it is likely to provide the water flows necessary for a system and what requirements the system might face from licensing. Large databases (such as those shown in Abesser et al., 2014) are consulted for information on aquifers and geology, whether other projects have accessed the aquifer and, if so, what flow rates of water they have achieved, and whether other systems exist nearby in an effort to estimate whether the crucial ingredients of a system exist at the proposed location. If the resource is suggested to be present, the process can proceed.

Drilling, geophysical and geotechnical investigation

Proving the physical existence of adequate thermal resource is the next stage of investigation and testing. This is done through drilling, geophysical and geotechnical investigations. To access and prove the existence of groundwater at the proposed location, a well must be drilled. During the process of drilling and well construction, information can be gathered on the ground which is being drilled and the conditions within the aquifer through geophysical and geotechnical methods. For wells drilled to depths of greater than 20 m, it is a legal requirement in England to submit the logged information to the BGS (e.g., depth of water strike, lithology). Further information gathered might include physical details about the ground type and its engineering, material and hydrogeological properties. Freeze and Cherry (1979) and Wilson (1990) both provide further details on wells, ground and aquifer properties. Thorough geophysical and geotechnical investigation of sites is unfortunately not common due to the associated costs. It is also common for selected drilling methods

to be destructive of geotechnical information (e.g., rock-rolling methods instead of wire-line HQ/NQ coring). Some examples and details on geophysical investigations can be found in Wang et al. (2015) and Boon et al. (2020).

Pump testing and hydrogeological characterisation

Once a well is constructed, pump tests are conducted to investigate the rate at which water can be pumped into and from the well, and the response of the water table to such pumping. To conduct the pump test, a pumping ensemble is installed within the well below groundwater level. The ensemble draws water from the ground and pumps it to the surface ('abstraction') while flow rates and water levels are monitored. In reverse, it can also inject water into the well from the surface ('injection'). Pump tests can be conducted at varying rates and for varying time frames - their design and considerations are discussed in BSI (2003) and BSI (2012). The data from the pump test is analysed and evaluated to understand the hydrogeological properties of the well and aquifer at the site. An abundance of analysis methods and theories exist, a detailed summary of which can be found in Kruseman, De Ridder, and Verweij (1970). If testing indicates that a sufficient quantity of water can be abstracted from the aquifer to meet the requirements of the system without negatively impacting/exhausting the aquifer, the design process can proceed.

Tracer testing and transport characterisation

If an open-loop system is to re-inject abstracted fluid into the aquifer, the transport properties of the aquifer require investigation. A second well for injecting fluid will need to be constructed at a distance from the abstraction well. The transport properties impact the rate and manner in which injected warmed (or cooled) water will travel within the aquifer. A key interest of this investigation is the rate at which the injected thermal energy is expected to travel toward the abstraction well. Injected thermal energy or thermal waste energy can be either above or below the background energy state of the aquifer. Thermal waste energy reaching the abstraction well and altering the temperature of abstracted fluid is known as 'thermal breakthrough' and is generally considered to be undesirable since it

can have an adverse impact on system performance. The transport properties of the aquifer can be investigated through a tracer test. A tracer test involves injecting a known quantity of a specific chemical into the aquifer at a known location and monitoring the concentration of said chemical at other locations in the aquifer. Various configurations and designs for tracer tests exist (see Shook, Ansley, and Wylie, 2004; Maurice et al., 2011). The test can be performed while the installed wells are pumping or simply under natural regional groundwater flow conditions. Once conducted, the observational data from the tracer test is analysed to determine transport properties of the aquifer (Shook, Ansley, and Wylie, 2004; Mathias et al., 2009; Axelsson, Bjornsson, and Montalvo, 2005; Bear, Tsang, and De Marsily, 2012; Adams and Davis, 1991; Adams et al., 2001). Analysis is typically conducted with the assistance of computational tools such as `MODFLOW/MT3D`. If the test results indicate that injected thermal waste fluid is likely to quickly arrive at the abstraction well, the open-loop GSHS may not be permitted to proceed to full design and construction. Alternatively, the results may indicate that thermal breakthrough is either unlikely or will take several years to occur. The system may therefore be viable and can proceed further in the design process.

The manner in which a chemical travels within the aquifer differs from how thermal energy might travel. The chemicals used in tracer tests are usually chosen because they have low interaction levels with the aquifer's soil/rock (i.e., adsorption), travelling predominantly in the pore space via advection and hydro-mechanical dispersion and with molecular diffusion. The following definitions for the various transport mechanisms are adopted: *advection* is the bulk motion of a quantity with flow of the carrier fluid (e.g. water flux), *hydro-mechanical dispersion* ('dispersion') is the spreading of a quantity along a concentration gradient due to pore-scale variations in the water flux, *molecular diffusion* ('diffusion') is the spreading of a quantity along a concentration gradient due to molecular-scale energy fluctuations, and *sorption* is a retarding factor that represents quantity exchange between ground with storage ability and pore fluid, along a concentration gradient (see Nield, Bejan, et al., 2006, for detailed explanations of each). In thermal transport, diffusive

spreading of heat is referred to as conduction. Chemical tracer tests and their evaluation can infer thermal transport properties due to the similar characteristics of solute transport and thermal transport, but do not explicitly determine the thermal dispersion and diffusion properties. To more precisely determine thermal properties, a thermal test must be conducted at the proposed open-loop GSHS location.

Thermal transport tests for an open-loop GSHS include material tests and thermal tracer tests. Material tests involve sampling the aquifer's soil/rock and testing its thermal properties in a laboratory (e.g., thermal conductivity, specific heat capacity, density, porosity). They can also be performed on site via geophysical methods (see Boon et al., 2019; Wang et al., 2015). A thermal tracer test involves the injection of thermal energy at a known location and monitoring temperature at the injection location and/or other locations. Thermal tests are not common due to their expense, but they are occasionally conducted (see Law and Mackay, 2010). Therefore, it is common for designers to adopt thermal transport properties inferred from tracer-test results and literature sources documenting thermal properties of the aquifer at the proposed location (e.g., Headon et al., 2009; Busby et al., 2009; Busby, 2015; Busby, 2018; Gelhar, 1993).

Operational modelling

Hydraulic and transport properties are then used in computational models, which are used to evaluate and forecast the thermal evolution of the proposed open-loop GSHS. An example of a popular commercial program for thermal modelling is `FEFLOW`. The tests and evaluated properties aid engineers to build a computational model that is representative of the host aquifer and wells. At this point in the design process, engineers will have established the likely cooling and heating loads of the space which will use the associated heat pump. Based on expected heating and/or cooling loads, engineers can determine the rate of fluid abstraction required and the temperature at which the effluent fluid will be returned to the aquifer. These flowrates and temperatures are applied to the computational model, which simulates the hypothetical GSHS under operational conditions. The simulated injected fluid

and the energy that it is carrying will migrate through the modelled aquifer over time. Engineers will evaluate whether the injected thermal 'plume' is expected to influence the temperature at the abstraction well, as well as how it may interact with and impact both the broader aquifer region and any adjacent wells/systems.

1.2 Background & Motivations

In this thesis we predominantly evaluate testing, calibration and operational performance information associated with an open-loop GSHS well doublet, constructed at Royal Festival Hall (RFH), London. Relevant details of this system are reported in each chapter. The system has previously been the subject of a technical report by Gale, Williams, and Mansour (2006) and publications by Clarkson et al. (2009) and Birks (2019).

Clarkson et al. (2009) and Gale, Williams, and Mansour (2006) establish the original testing results, design and modelling of the RFH system. Birks (2019) observed that the open-loop GSHS at RFH appeared to experience a number of thermal events throughout its operational life since commissioning. Birks (2019) attributed the events to 'thermal breakthrough' (the arrival of injected thermal energy at the abstraction well), and noted that their occurrence was a deviation from the expected behaviour outlined by Clarkson et al. (2009). The deviation from the modelled/expected behaviour remains unexplained, and could foreseeably result in unexpected operational adjustments and costs for RFH beyond those designed and budgeted for. The events at RFH are not disastrous and the system maintains its functionality, however they ought to be adequately addressed and explained where possible.

GSHS construction has a large front-end capital expenditure during design and feasibility stages, well before the system is commissioned and yields returns (Birks et al., 2015a; Banks, 2009a). Assurances around system performance and design life estimates are crucial to underpinning their financial case and consumers being willing to adopt their remaining risks. If GSHS are observed to deviate from their expected behaviour, trust in their predictability could erode, along with consumer

confidence. An increase to the perceived risk of adopting the technology could see fewer systems advance from feasibility studies through to full commissioning and operation. Therefore strong motivation exists to interrogate the thermal events at RFH, aiming to further our understanding of them and attempt to attribute cause.

Revisiting RFH's initial testing, calibration and performance predictions is most aptly named a back-analysis. Arthur and Streetly (2009) highlight the crucial need to revisit design assumptions and predictions for thermal systems, verifying their appropriateness for future designs. The installation and operation of open-loop GSHS is a relatively young industry, and it is believed that the back-analysis of RFH presented here is a first of its kind. Furthermore, lessons learned from revisiting design assumptions, testing and modelling could lead to improved front-end design and investigation techniques, potentially increasing both consumer confidence and the adoption of GSHS as a sustainable alternative to fossil fuel technologies.

Beyond RFH, the notion of materialising arguments for more sustainable operational strategies also motivated the thesis. In the United Kingdom, it is generally rare for commissioned systems to operate in a relative proximity to others that tap the same thermal reservoir. However, in London a large number of systems are operating and interaction between these systems is increasingly plausible. Increased proximity of systems will necessitate careful management of injected thermal plumes and calls for increased understanding of available operational strategies to achieve this. This thesis provides quantitative material to show the benefits of a seasonally reversed strategy (as theorised by Banks, 2011b) over unidirectional systems.

In summary, the aforementioned motivations have led to the following hypotheses being explored in this thesis:

1. The observed events at RFH are thermal breakthrough. Incorrect prediction of breakthrough time may be resulted from error(s) within the original testing, modelling and/or calibration efforts.

2. The ability to re-simulate observed behaviour will act to reinforce appropriate testing and modelling assumptions adopted by GSHS designers.

3. A seasonally reversed operational strategy is superior to a unidirectional strategy in predicted design life and energy efficiency, and with regard to sustainable practices.

1.2.1 Contribution

In addressing the above hypotheses, this thesis provides the following novel contributions to the open-loop GSHS field:

1. A re-calibration of hydraulic properties at RFH, adopting a Darcy-Forchheimer flow regime, as suggested by Mathias, Butler, and Zhan (2008) and Mathias and Todman (2010), and expanding the method to analyse grouped wells, multi-layered aquifers, flawed pumping data and well aging. Parameter sensitivity within the Darcy-Forchheimer approach is also explored to highlight the driving mechanisms behind simulated pump drawdown curves (Chapter 2).

2. A re-calibration of the apparent solute transport properties at RFH, taking into account hydraulic insights from Chapter 2. A parameter sensitivity analysis of the adopted solute transport model, permitted by computationally efficient construction of said model, was conducted and highlighted the driving mechanisms behind simulated tracer breakthrough curves (Chapter 3).

3. Isolation of a thermal event within an open-loop GSHS to perform a calibration of apparent thermal transport properties. Three simple models were shown to reproduce observed behaviour and highlighted the poorly constrained nature of the system. The three separate groups of calibrated properties were used to simulate several years of operational history. The modelling results were inconclusive, serving to highlight the critical importance of testing and instrumenting systems in a manner that supports monitoring and modelling efforts (Chapter 4).

4. A comparison of unidirectional and seasonally reversed operational strategies, quantifying the benefit of adopting the latter. This was followed by a parameter influence study of dispersion, matrix conduction and local thermal non-equilibrium on a RFH-sized system (Chapter 5).

Together, the above form a back-analysis of an installed open-loop GSHS, contributing to understanding of testing, calibration and modelling approaches beyond just RFH. The field of Aquifer Thermal Energy Storage (ATES) (see Dickinson et al., 2009, for introduction to ATES) bears many similarities with open-loop GSHS and potentially stands to benefit from these contributions also.

Across the studies conducted several simple models were constructed. The simple models permitted vast analysis while remaining relatively time efficient and computationally inexpensive. These models demonstrated an ability to capture observed behaviours and even highlight poorly constrained problems. This consequently highlights the under-constrained and computationally expensive nature of available complex modelling tools.

2

Hydrogeological Calibration

Contents

The contents of this chapter have been adapted from a manuscript in preparation for a submission to a journal. The manuscript is titled "Characterising a multi-well, layered aquifer and assessing well aging using a Darcy-Forchheimer model". For this reason a paper-style format is provided. The work is that of the main author's, with

co-authorship (through supervision) attributed to L.T. Jenkins and C.W. MacMinn

2.1 Abstract

Characterisation of hydraulic performance under pumping and/or injection is central to the design of engineering systems dependent on subsurface flow. The Darcy-Forchheimer equation has previously been shown as an equivalent method to the well-established, empirical Jacob's model for characterising the performance of individual wells and their host aquifers. Here, we apply the Darcy-Forchheimer equation to characterisation of a multi-well aquifer, recovery of flawed pumping data and the analysis of aging well performance, with the use of two case studies: data from Clark (1977) and Royal Festival Hall (RFH). A simplified hydraulic model is constructed and used to characterise multi-layer aquifer and well properties by calibrating a best-fit between simulate and observed testing data. A novel approach to the governing boundary conditions is adopted to enable the modelling of imperfect data resulting from the practicalities of industry-based site investigation processes. This novel approach, applied to both step and constant rate pumping tests, aids the isolation of human- and instrumentation-error to individual flow steps and/or testing periods. This may lead to a greater confidence in computed characterisation results and the improved ability to analyse imperfect pumping data that may previously have been discarded. The uniqueness of the calibrated best-fit, and corresponding physical parameters, is assessed for single- and multi-well, single- and multi-layer aquifer scenarios. The performance deterioration of a well due to aging is also assessed by the model and shown to be captured by the Darcy-Forchheimer parameter, which is used as a representation of aquifer properties in close proximity to the well. The simple modelling approach shows strong potential to aid design processes by quickly identifying appropriate site-specific parameters to be used as inputs to more complex modelling programs.

2.2 Introduction

A groundwater borehole or well is a shaft bored into the ground, typically vertically, for the purpose of extracting (abstracting) and/or injecting water from/to an aquifer. (Note that in this study we refer to 'borehole' and 'borehole-well' as 'well'.) To better understand the rate and volume of water that can be abstracted or injected by an operating well over time, characterising the hydraulic performance of the well and its host aquifer is required. Hydraulic performance encompasses the properties of the aquifer, the properties of the well, and their coupled properties. The properties of the aquifer describe its hydraulic response to pumping, and include its transmissivity/permeability and storativity; the properties of the well describe the physical dimensions and construction of the well within the aquifer. The coupling of these properties under operational flow conditions results in the shared apparent linear and non-linear hydraulic head-losses due to friction and inertia.

Techniques for analysing hydraulic performance include the step-drawdown test (SDT) and the constant-rate test (CRT). The SDT involves pumping at a steady rate and recording the observed water-level change in the well, which is known as drawdown for extraction and as uplift for injection. The water level in the well is expected to reach a quasi-steady state for a given pumping rate, upon which the pumping rate is 'stepped' to the next nominated flowrate. This process is repeated several times, typically at least four (Clark, 1977; BSI, 2003). The CRT instead involves imposing a single continuous pumping rate for an extended period of time. Together, these tests are used to develop insight into the hydraulic properties of the aquifer, observe the well's performance across a range of flows, and identify long-term 'sustainable' pumping rates.

Analysing the resulting testing data consists of fitting a suitable model to the observed drawdown or uplift, s_w [L]. The standard model is an empirical one proposed by Jacob (1947), who suggested that the non-linear increase in well drawdown with pumping rate $\hat{Q}$ [L^3T^{-1}] can be captured by:

$$s_w = A\hat{Q} + B\hat{Q}^2 \tag{2.1}$$

where A [$L^{-2}T$] is the formation-loss coefficient and B [$L^{-5}T^2$] is the well-loss coefficient. In Jacob's formulation, $A\hat{Q}$ represents linear hydraulic head-loss in the aquifer and $B\hat{Q}^2$ represents non-linear hydraulic head-loss specific to the well (Bierschenk, 1963). Houben and Treskatis (2007) and Houben (2015) discuss the various contributions to head-loss, including aquifer loss, skin loss, packing loss, convergence loss, and screen loss. The Darcy-Forchheimer (DF) equation (Forchheimer, 1901) similarly combines a linear Darcy term with a non-linear inertial (Forchheimer) term (see Equation (2.8)). The Forchheimer term includes a new coefficient, the Forchheimer parameter (b [L^{-1}]), which represents the head-loss due to fluid inertia. Recent work has illustrated the application of DF for capturing non-linear head-loss associated with fluid inertia during pump testing (Mathias, Butler, and Zhan, 2008; Mathias and Todman, 2010), converging flows (Şen, 1988) and flow within fractured rocks (Kohl et al., 1997; Kolditz, 2001). Mathias and Todman (2010) demonstrated that Jacob's formulation is essentially a large-time approximation to DF, and that DF provides a significantly better early-time fit to observed pumping drawdown data. The shortcomings of the Jacob equation, such as absent well storage, can be accounted for by additional coefficients and terms, but the resulting empirical equations are complex and over-parameterized (Rorabaugh, 1953; Helweg, 1994; Van Tonder, Botha, and Van Bosch, 2001).

Traditionally, Jacob's well-loss term ($B\hat{Q}^2$) is associated with pressure/head-losses within the well infrastructure, where flows have converged and are faster (Bierschenk, 1963; Barker and Herbert, 1992). However, B must also include the non-linear inertial losses associated with the surrounding aquifer, which also experiences greater flow velocities for the same reason (Şen, 1988; Mathias, Butler, and Zhan, 2008; Butler et al., 2009). In contrast, the DF equation nominally accounts for inertial losses within the aquifer while no longer explicitly accounting for hydraulic losses within the well infrastructure. The inertial losses are expected to be large in close proximity to the well, where flux velocities and magnitudes are at their greatest, and to decrease with increased distance from the well, trending toward an increasingly linear flow regime. This physical formulation of the DF equation means

that the importance of the Forchheimer term is primarily near the well (local), while the Darcy term reflects the flow properties of a wider region of the aquifer (regional).

Here, we adopt the DF non-linear term as an expression of well and near-well behaviour, and the DF linear term as a reflection of regional aquifer properties. This approach enables two previously unexplored applications of the DF equation:

1 - The DF equation can be used to couple multiple separate wells, in relative proximity, to characterise an aquifer using a single set of hydraulic parameters. The physical formulation of the DF equation allows for each well to have unique local non-linear behaviour, expressed through the Forchheimer parameter, while the well-group is assumed to share the same regional aquifer properties (i.e., transmissivity and storativity) and,

2 - The DF equation may be used to assess the evolution of the well and/or aquifer properties in time. By characterising the hydraulic properties at two points in time through pumping tests, changes in the characteristics will be representative of changes in the local and/or regional properties. These changes may be due to use of the wells or natural causes.

Hydrogeological modelling of multiple wells and large aquifers often takes the approach of dividing the domain somewhat arbitrary into sections characterised by distinct hydraulic performance (e.g., Allen et al., 1997; Soley et al., 2012). This approach introduces complexity, computational cost, and over-parameterisation associated with selecting the boundaries between sections. Associating a group of wells with a single set of regional aquifer parameters, as suggested here, avoids these problems. This approach is most appropriate for wells and systems of relatively small domain size, such that regional aquifer parameters can reasonably be expected to be similar and that crucial heterogeneity can be retained. The idea of associating wells and their tests to regional aquifer parameters ties to previously empirical or linear numerical work dating back to Toth (1966) and including Bibby (1977), Bibby (1979), Streltsova (1987), and Osiensky et al. (2000). Bibby (1979) discussed the meaning of estimated local and regional aquifer parameter averages derived from early and

late-time data. Streltsova (1987) suggested derived parameters represent between-well properties and properties directly surrounding the well, while also suggesting that heterogeneity in close proximity to the well exerts far greater influence than that further away. Finally, Osiensky et al. (2000) addressed the validity of averaging parameters over an increasingly large domain area and well separation, showing that accuracy relies on pumping times being large enough that the observed response is representative of a sufficiently large area of the aquifer to encompasses all wells.

Here, a simplified DF model is constructed to simulate SDT and CRT tests in single- and multi-layer confined aquifers (Section 2.3). The model is applied to two case studies: A single SDT published by Clark (1977)(Section 2.4) and multiple pumping tests from the site investigation of Royal Festival Hall (Clarkson et al., 2009)(Section 2.5). Local and regional properties are characterised through least-squares optimisation. The model conditions and calibration process are adapted to account for the practicalities of pump testing by considering errors stemming from site instrumentation, operations and reporting. The identifiability of the parameters is investigated by a progressive Monte-Carlo method and Kolmogorov-Smirnov score (K-S test), for single- and grouped-well scenarios. The model is also used to provide insight into a flawed and previously discarded pumping test. Finally, the calibrated well and aquifer parameters are used to assess the aging performance of a well.

2.3 Approach to Modelling and Calibration

The below sections detail the governing equations used to construct the simplified DF model, followed by its application to calibrate hydraulic properties through simulating the observed pump test data.

2.3.1 Model

A model is developed to represent a layer sequence of confined aquifers with axisymmetric flow toward a well. All layers are taken to be uniform, homogeneous, isotropic and laterally infinite. The model is shown in Figure 2.1.

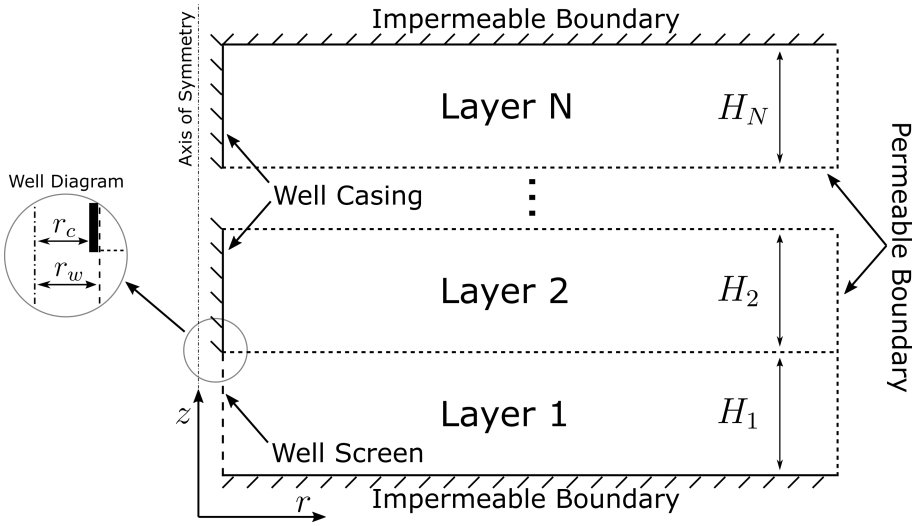

Figure 2.1: Model schematic illustrating impermeable confining and well-casing boundary conditions, as well as inter-layer and well screen permeable conditions. The impermeable boundary below Layer 1 is nominal as further layers can be added below if desired. Likewise, a 'fully penetrating' connection or impermeable casing condition can be assigned to each layer. The well diagram shows the measurement of well radius (r_w) and casing radius (r_c).

The continuity equation for weakly compressible, axisymmetric flow around a well may be written:

$$\frac{S}{\rho g H}\frac{\partial p}{\partial t} + \frac{1}{r}\frac{\partial}{\partial r}(r q_r) + \frac{\partial}{\partial z} q_z = 0, \tag{2.2}$$

where S [-] is the storativity, g [LT^{-2}] is the force per unit mass due to gravity, ρ [ML^{-3}] is the density of water, H [L] is the thickness of the aquifer, p [$\mathrm{ML}^{-1}\mathrm{T}^{-2}$] is pressure, t [T] is time, r [L] is the radial distance from the centre of the well, z [L] is the vertical position (see Figure 2.1), q_r [LT^{-1}] is the radial flux, and q_z [LT^{-1}] is the vertical flux. Integrating Eq.(2.2) over the thickness of aquifer layer n gives:

$$\frac{S^n}{\rho g}\frac{\partial p^n}{\partial t} + \frac{1}{r}\frac{\partial}{\partial r}(r H^n q_r^n) + q_z^{n,T} - q_z^{n,B} = 0, \tag{2.3}$$

where S^n [-] is the storativity of layer n, H^n [L] is the thickness of layer n, p^n [$\mathrm{ML}^{-1}\mathrm{T}^{-2}$] is the mean pressure in layer n, q_r^n is the mean radial flux in layer n, and $q_z^{n,B}$ and $q_z^{n,T}$ [LT^{-1}] are the vertical fluxes into the layer at its bottom and out of the layer at its top, respectively. This formulation allows for the three-dimensional flow domain to be modelled with a series of vertically coupled,

one-dimensional partial differential equations (PDEs). The governing PDEs are subject to initial and boundary conditions, which differ between pumping (uncased) and non-pumping (cased) layers:

$$\begin{gathered} p^n = p_0, \quad \text{for} \quad r \geqslant r_w,\ t = 0, \\ p^n = p_w \quad \text{at} \quad r = r_w,\ t > 0, \quad \text{or} \quad q_r^n = 0 \quad \text{at} \quad r = r_w,\ t > 0, \\ p^n = p_0 \quad \text{for} \quad r \to \infty,\ t > 0, \end{gathered} \tag{2.4}$$

where r_w [L] is the radius of the well, p_0 [$\mathrm{ML^{-1}T^{-2}}$] is the initial and far-field pressure and p_w [$\mathrm{ML^{-1}T^{-2}}$] is the pressure in the well at the same datum. Note that non-pumping layers are subject to a no-flux condition at the well and that the background hydrostatic gradient has been eliminated from all layers.

The relationship between p_w and the flow into or out of the well is known as a well model. A simple and established well model is that of Papadopulos and Cooper Jr (1967):

$$\frac{\pi r_c^2}{\rho g}\frac{\mathrm{d}p_w}{\mathrm{d}t} + \hat{Q}(t) + \sum_{n=1}^{N} 2\pi H^n r_w q_r^n(r_w, t) = 0, \tag{2.5}$$

where r_c [L] is the internal radius of the well casing, $\hat{Q}$ is the volume rate of pumping (abstraction for $\hat{Q} > 0$ and injection for $\hat{Q} < 0$), and $p_w = p_0$ at $t = 0$. Assuming hydrostatic pressure within the well, the well pressure is related to the drawdown s_w [L] via

$$s_w(t) = \frac{p_w(0) - p_w(t)}{\rho g}. \tag{2.6}$$

Previous approaches to modelling pumping tests have relied on the idealised condition of a known steady pumping rate $\hat{Q}$ to drive the well pressure equation and the simulated drawdown. In practise, pumping rates and flowmeter readings suffer from fluctuations, noise, and instrumentation- and human-error (BenBarka, 1982; Paul, 1993; Renard, Glenz, and Mejias, 2009). Therefore, the need may arise to simulate flawed or noisy pumping data, or to omit such periods without forfeiting observations at later times (such as the post-test recovery period). During testing, p_w itself is measured directly by installed down-hole devices (e.g., pressure

transducers) and cross-referenced with manual measurement of s_w via dipping (Paul, 1993). These simple logging and verification methods lead to a high confidence in data integrity, and can therefore be imposed as an alternative boundary condition in place of Eq.(2.5):

$$p_w = p_{w,o}(t) \quad \text{or} \quad p_w = p_0 - s_{w,o}(t)\rho g, \tag{2.7}$$

where $p_{w,o}(t)$ is the observed pressure and/or $s_{w,o}(t)$ [L] is the observed drawdown.

For a single aquifer, the radial component of the DF equation can be written

$$\frac{\mu}{k_h^n} q_r^n + \rho b^n q_r^n |q_r^n| = -\frac{\partial p}{\partial r}, \tag{2.8}$$

where μ [$\mathrm{ML^{-1}T^{-1}}$] is dynamic viscosity, k_h^n [$\mathrm{L^2}$] is horizontal permeability and b^n [$\mathrm{L^{-1}}$] is the Forchheimer parameter. Note that we have assumed axisymmetry and predominantly horizontal flow, such that $|\mathbf{q^n}| \approx |q_r^n|$. Eq.(2.8) can be solved for q_r^n:

$$q_r^n = c^n d^n \left(-1 + \sqrt{1 + \frac{2k_h^n}{c^n \mu} \left| \frac{\partial p^n}{\partial r} \right|} \right), \tag{2.9}$$

where,

$$c^n = \frac{\mu}{2\rho b^n k_h^n} \quad \text{and} \quad d^n = -\text{sign}\left(\frac{\partial p^n}{\partial r} \right). \tag{2.10}$$

In the absence of inertial losses ($b^n \to 0$), Eq.(2.8) reduces to Darcy's Law. The small vertical flow between layers is expressed as a Darcy flux (no inertial loss) using the harmonic mean of the associated physical properties:

$$q_z^{n,T} = -q_z^{n+1,B} = -\frac{1}{\mu} \left[\frac{H^{n+1} + H^n}{H^{n+1}/k_v^{n+1} + H^n/k_v^n} \right] \left[\frac{2(p^{n+1} - p^n)}{H^{n+1} + H^n} + \rho g \right], \tag{2.11}$$

where k_v^n [$\mathrm{L^2}$] is the vertical permeability. For horizontal flow in a confined aquifer, horizontal permeability k_h^n is related to transmissivity T^n [$\mathrm{L^2T^{-1}}$] via

$$T^n = \frac{\rho g H^n k_h^n}{\mu}. \tag{2.12}$$

We use both quantities (T^n and k_h^n) when comparing to previous work, but note that transmissivity is traditionally defined without the presence of vertical flow (Freeze and Cherry, 1979). The common use of hydraulic conductivity (K [$\mathrm{LT^{-1}}$]) in hydrogeological assessment is acknowledged but not adopted by the present

study which uses fundamental terms (i.e., permeability). Conversion of permeability to hydraulic conductivity is performed by

$$K^n = \frac{\rho g k^n}{\mu}. \tag{2.13}$$

We solve the above problem numerically by discretising in space using a finite-volume method and integrating in time using `MATLAB`'s built-in adaptive implicit solver for stiff ordinary differential equations, `ODE15s` (Shampine and Reichelt, 1997; Mathias, Butler, and Zhan, 2008). To approximate an infinite domain, the far-field boundary is placed at a multiple of the characteristic length-scale for pressure diffusion,

$$r_\infty = a\sqrt{2\alpha_{hydro}\bar{t}}, \tag{2.14}$$

where a [-] is a constant multiple, $\alpha_{hydro} = T/S$ [$\mathrm{L^2T^{-1}}$] is the hydraulic diffusivity, and $\bar{t}$ [T] is the total pumping time. A multiple of $a = 5$ was selected based on a sensitivity analysis that identified appropriate values of a to be greater than unity. In the case of multiple layers, the layer of greatest hydraulic diffusivity governs the selection of r_∞. The resulting radial domain $r_w \leqslant r \leqslant r_\infty$ was discretised into 1000 grid blocks with logarithmic spacing based on a convergence analysis. Figure 2.2 illustrates domain size and convergence analysis results, with reference to past work by Mathias and Todman (2010) and Upton et al. (2019). The present analysis adopts a relative error of approximately 0.005% in computed drawdown measurements.

2.3.2 Calibration

The model is applied to pump testing data from two case studies. The first case study, initially presented by Clark (1977), features a single SDT and is used to benchmark the present model against the work of Mathias and Todman (2010). Clark's SDT was also used by Upton et al. (2019) to qualitatively validate their model, but they did not report their best-fit parameters. The second case study includes calibration based on SDT and CDT data from Royal Festival Hall (RFH). Details on RFH are published by Clarkson et al. (2009). Additional independent

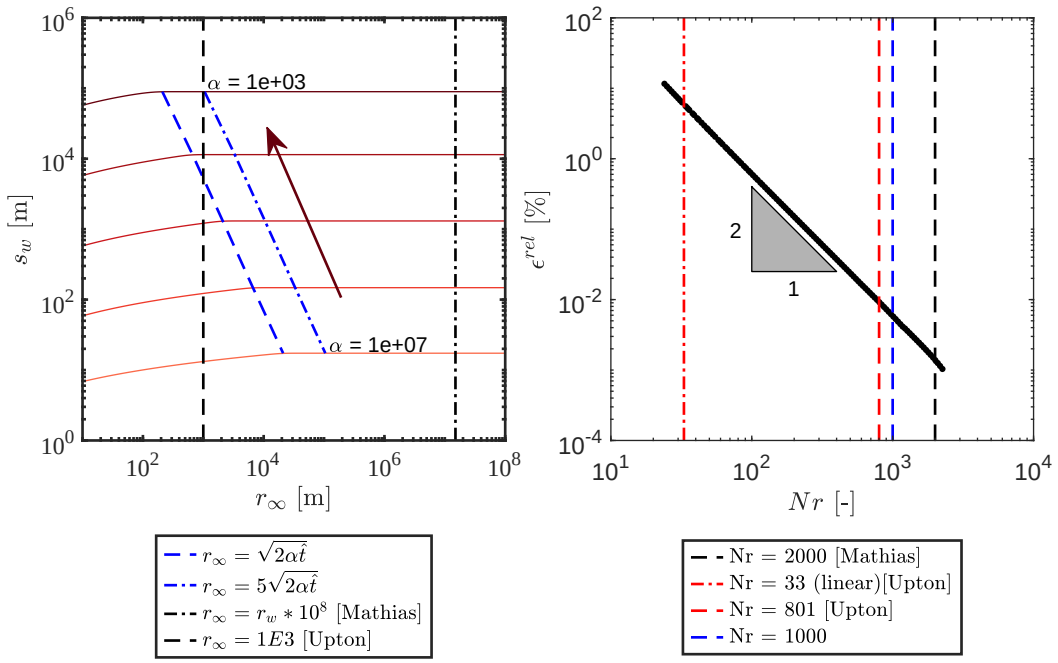

Figure 2.2: (Left) Analysis of domain size. Final simulated drawdown of single-layer aquifer subject to an abstraction rate of 10 L/s for 89 hours, for a given hydraulic diffusivity, α [m^2/day], well radius $r_w = 0.15$ m, and far-field boundary distance, r_∞ [m]. Hydraulic diffusivity values are $log_{10}(\alpha) = 3$, 4, 5, 6 and 7. (Right) Convergence of solutions relative to $Nr = 5000$, and where Nr [-] is the number of discrete points, showing second order convergence. Values used by Upton et al. (2019) and Mathias and Todman (2010) are shown for reference.

data sets for RFH are not available for a site-specific validation process, thus it is assumed that, as per prior studies, the model's benchmark application to Clark suffices. These case studies are used to explore various approaches to calibration and degrees of freedom within the calibration procedure:

Standard Method

A standard approach to calibrating hydraulic properties from pumping tests is conducted. This involves using case-study data to simulate pumping tests and calibrate a best-fit curve with the observed drawdown data. Three calibration methods are used, as detailed in Sections 2.4.1, 2.4.2 and 2.4.3.

Back-Analysis of Flow Rates

Opposite to the standard manner that pump testing data is used, the model is used to back-calibrate average pumping rates (RFH only) by solving for $\hat{Q}$ with assumed T, S, b, r_w, r_c and H. This analysis is detailed in Section 2.5.3.

Well Aging

Well aging is analysed by calibrating hydraulic properties based on pumping tests conducted a year apart (RFH only). The calibration methods detailed in Sections 2.4.1, 2.4.2 and 2.4.3 are adopted. This analysis is detailed in Section 2.5.4.

To calibrate a best-fit curve, the model is nested within `MATLAB`'s bounded non-linear minimization function `FMINSEARCHBND`. The bounded minimizing function is responsible for seeding parameter values (e.g., k_h, k_v, S, b, r_w, r_c and $\hat{Q}$) between prescribed lower and upper limits which are then used to simulate a pumping test. The error is assessed by calculating the mean absolute error $\langle \varepsilon^{abs} \rangle$ [L] between observed and simulated drawdown:

$$\langle \varepsilon^{abs} \rangle = \frac{1}{N_t} \sum_{i=1}^{N_t} \mid s_{w,o}(t_i) - s_w(t_i) \mid, \tag{2.15}$$

where $\langle \varepsilon^{abs} \rangle$ [L] is the mean absolute error, N_t [-] is the total number of data points and $s_w(t_i)$ [L] and $s_{w,o}(t_i)$ [L] are the simulated and observed drawdown at time t_i, respectively. The minimizing function continuously alters parameter values and evaluates the resulting simulation accuracy until a minimum $\langle \varepsilon^{abs} \rangle$ is achieved. The parameter set corresponding to the minimum $\langle \varepsilon^{abs} \rangle$ is reported as the best fit. Where suggested best-fit parameter values were in close proximity to their prescribed lower or upper limits, the limits were extended to allow additional evaluation.

For reference, we also report the value of the mean relative error $\langle \varepsilon^{abs} \rangle$ [%] for each calibration. The mean relative error is calculated as

$$\langle \varepsilon^{rel} \rangle = \frac{100}{N_t} \sum_{i=1}^{N_t} \frac{\mid s_{w,o}(t_i) - s_w(t_i) \mid}{s_{w,o}(t_i)}. \tag{2.16}$$

Method	T [m^2/day]	S [-]	b [m^{-1}]	r_w [m]	r_c [m]	$\langle\varepsilon^{abs}\rangle$ [m]	$\langle\varepsilon^{rel}\rangle$ [%]
Theis	357	1.20E-4	-	-	-	-	-
Bierschenk & Wilson	362	-	-	-	-	-	-
Hazel	380	5.70E-4	-	-	-	-	-
Eden and Hazel	362	1.30E-4	-	-	-	-	-
Jacob	468	0.20E-4	-	-	-	-	-
Darcy-only	402	0.05E-4	0.00E+0	0.250	0.250	0.611	5.82
Mathias	393	2.34E-4	6.39E+8	0.250	0.250	0.254	-
Cal.1	405	1.35E-4	6.39E+8	0.250	0.250	0.238	1.93
Cal.2	399	1.69E-4	6.67E+8	0.261	0.169	0.219	1.86
Cal.3	401	1.59E-4	6.73E+8	0.260	0.176	0.227	1.91

Table 2.1: Summary of calibration results for Clark (1977). Horizontal permeability (k_h) values from calibrations have been converted and reported in terms of transmissivity (T) for comparison with previous work. Transmissivity and storativity results from various analytical methods (Theis, 1935; Beirschenk and Wilson, 1961; Hazel, 1973; Eden and Hazel, 1973) are as calculated by Clark (1977). Jacob (1947) analytical result calculated excluding the recovery period. An equivalent Forchheimer parameter (b) has been produced for Mathias and Todman (2010) using their Eq.8.

2.4 Case Study: Clark (1977)

As a benchmark, the model was first applied to the hydraulic test presented in Clark (1977). Clark (1977) provides drawdown and flowrate data from a SDT comprising six three-hour steps in a confined sandstone aquifer with an effective well radius of $r_w = 0.25$ m. We model the case study as a single-layer confined aquifer. For this scenario, the possible calibration parameters include horizontal permeability (k_h), storativity (S), well radius (r_w), well casing radius (r_c) and Forchheimer parameter (b). The bench marking effort addresses three distinct points: a comparison with the linear method of Clark (1977), a comparison with the DF approach of Mathias and Todman (2010) (Calibration 1, Section 2.4.1) and the introduction of additional approaches to calibration (Calibration 2 and 3, Sections 2.4.2 and 2.4.3, respectively). The results of the benchmark analysis are summarised in Table 2.1 and drawdown curves are illustrated in Figure 2.3.

The model was first used to establish best-fit parameters for purely linear flow (i.e., $b = 0$). k_h and S were calibrated while other parameters were fixed to nominal values. The best-fit k_h (reported here in terms of T) is comparable with analytical calculations by Clark (1977), while the best-fit S is substantially smaller. As noted by Clark (1977), a low accuracy and dependability is placed

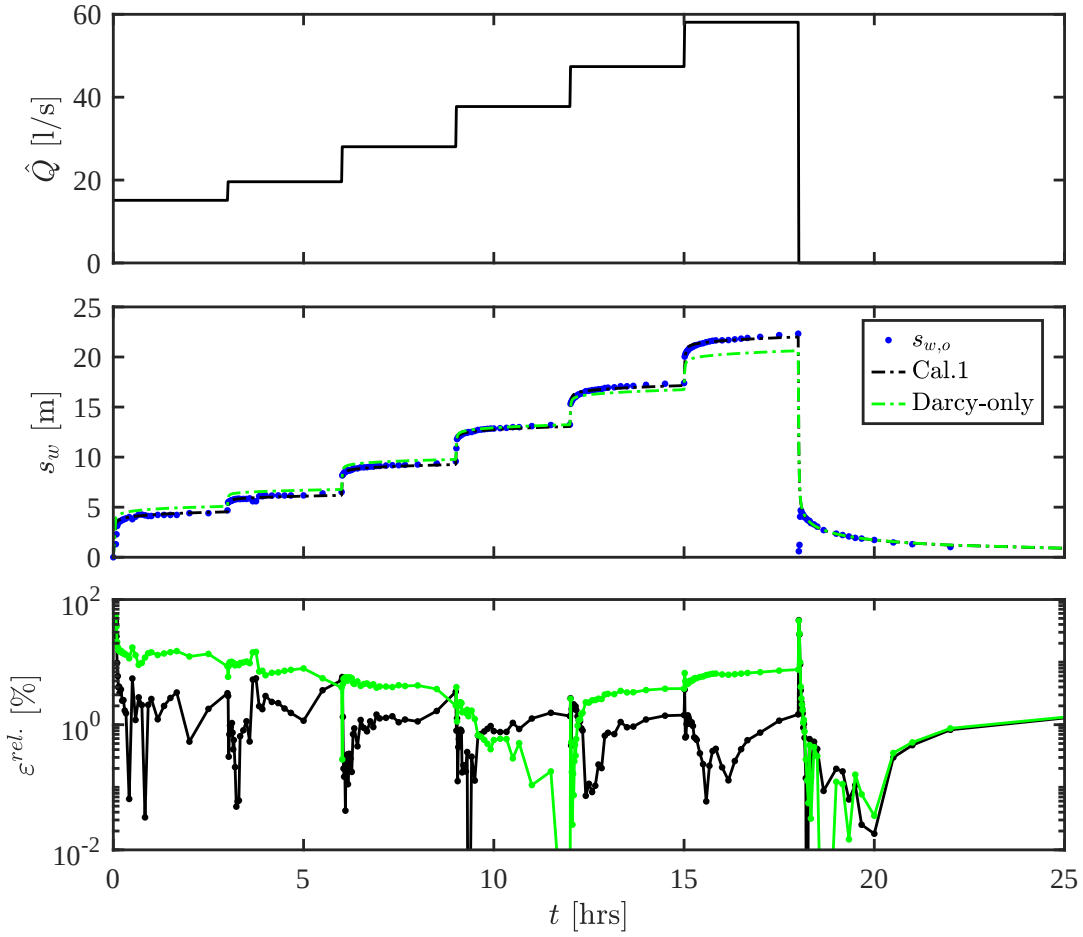

Figure 2.3: Best-fit results to the SDT from Clark (1977). The top panel shows the observed average flowrates (averaged over each step). The middle panel shows the observed drawdown and the simulated drawdown for the Darcy-only model and for Cal.1. The bottom panel plots the relative error in drawdown for Darcy-only and Cal.1. The results of Cal.2 and Cal.3 (not shown) are qualitatively and quantitatively similar to those of Cal.1.

on the calculation of S in the absence of an observation well serving to constrain the evaluation (or model). Therefore, we conclude that the linear model is in agreement with previous analytical work.

2.4.1 Calibration 1: Unknown k_h, S and b

The purpose of Calibration 1 (Cal.1) is to benchmark against the results of Mathias and Todman (2010) and Mathias, Butler, and Zhan (2008). To do so, the parameters r_w, r_c, H and $\hat{Q}$ are fixed to nominal values, as in Mathias and Todman (2010), and k_h, S and b are calibrated. The result is a replication of the model and

approach of Mathias and Todman (2010) and Mathias, Butler, and Zhan (2008) with the exception of numerical error tolerance (see above). The resulting calibration identifies comparable best-fit parameters to Mathias and Todman (2010) accounting for boundary and discretisation differences between models.

2.4.2 Calibration 2: Unknown k_h, S, b, r_w and r_c

In Calibration 2 (Cal.2) the parameters r_w and r_c are added to the calibration (H and $\hat{Q}$ are fixed to nominal values). The two radii are responsible for capturing the storage behaviour of the well under pumping and recovery conditions, which is reflected in the early drawdown behaviour. The ability to calibrate the two parameters is an advantage over analytical approaches which are limited to a finite well radius assumption (i.e. neglect well storage) (Theis, 1935; Beirschenk and Wilson, 1961; Hazel, 1973; Eden and Hazel, 1973).

Cal.2 yields a small improvement on the results of Mathias and Todman (2010) courtesy of the two additional degrees of freedom. The model trends toward a 4% larger well radius (r_w) and a 56% smaller casing radius (r_c) than the nominal values. The larger well radius may allude to a slightly-larger-than-drilled well diameter representative of a complex well-to-aquifer interface and/or well-development processes such as acidisation. The smaller casing radius may imply the presence of down-hole pumping infrastructure. Both values suggest that Clark (1977) simply reported the nominal drilled diameter of the well. Further validation is difficult since Clark (1977) provides no explicit measurements of the installed testing infrastructure or testing equipment, nor drilling records.

2.4.3 Calibration 3: Unknown k_h, S, b, r_w and r_c, with $\hat{Q}$ accuracy in doubt

Calibration 3 (Cal.3) is introduced on the idea that the observed flow rates $\hat{Q}$ may be unreliable over certain time intervals due to human or instrument error. As a result, it is desirable to be able to simulate individual steps (or portions of steps) independently of the observed flow rates during the rest of the SDT. The

difficulty in doing so is that the steps are coupled by the pressure field in the aquifer, with the pressure at the end of one step serving as the initial condition for the next step. As noted above, however, we expect the observed drawdown to be substantially more reliable than the observed (and averaged) flow rates in most cases. It is proposed that any desired portion of an SDT can be simulated in isolation via the following procedure:

1. Given a set of parameter values, simulate the entire SDT based on observed drawdown rather than observed flowrate – that is, by using $s_{w,o}$ with Eq.(2.7) rather than $\hat{Q}$ with Eq.(2.5) – thus producing a simulated pressure field throughout the aquifer for the duration of the SDT.

2. For the desired portion(s) of the SDT, use the pressure field from step 1 as the initial condition and then proceed with the simulation using the observed $\hat{Q}$ with Eq.(2.5). The resulting simulated drawdown can then be compared against the observations.

For Cal.3, we perform the procedure above for each step of the SDT in isolation and calculate $\langle \varepsilon^{abs} \rangle$ for the entire set. This error is then the basis for optimisation in order to calibrate the desired parameter values. Note that this procedure can be used to calibrate any individual step or time period in isolation, or to omit certain time periods from the calibration; the latter features are exploited below, in the second case study. For the first case study, Cal.3 yields comparable values of $\langle \varepsilon^{abs} \rangle$ and $\langle \varepsilon^{rel} \rangle$ to Cal.2, suggesting that the observed averaged flowrates are of relatively good quality.

Comparing the various bench marking efforts and calibration procedures, we make several observations and conclusions. Firstly, restricting the model to Darcy flow worsens the best-fit and highlights the importance of non-linear behaviour within the SDT. The use of the non-linear flow model, based on parameters suggested by Mathias and Todman (2010), immediately results in a 58% reduction in $\langle \varepsilon^{abs} \rangle$ relative to the linear approach. Secondly, the model, as constructed, calibrates best-fit parameters that are in agreement with both prior works and provides additional

calibrated parameters (r_w and r_c) that are physically plausible. Therefore, the uniqueness of the best-fit parameters and general sensitivity of the drawdown curve to calibration parameters is of interest and investigated in Section 2.4.4

2.4.4 Sensitivity Analysis

To assess the sensitivity of the model to each parameter, and hence the identifiability of each parameter, a progressive Monte-Carlo analysis was conducted. Since Cal.3 did not offer a significant advantage for Clark's SDT data and is more computationally expensive, Cal.2 was used. An *a priori* (prior) probability distribution was assigned to each of the five calibration parameters (k_h, S, b, r_w and r_c). Uniform random distributions were assigned to $\log(k_h)$, $\log(S)$, $\log(b)$, r_w and r_c. *Posteriori* (posterior) probability distributions for the calibration parameters were acquired using the GLUE methodology (Beven and Binley, 1992) as follows:

1. Values of k_h, S, b, r_w and r_c are randomly sampled from their *a priori* distributions.

2. The SDT is simulated with the selected values.

3. The resulting $\langle \varepsilon^{abs} \rangle$ is calculated.

4. Steps 1–3 are repeated 20,000 times. Results were observed to be insensitive to a greater sample size.

5. Posterior parameter distributions are calculated for each of the calibrated parameters based on the smallest 1% of $\langle \varepsilon^{abs} \rangle$ scores.

Steps 1–5 complete one stage of the progressive analysis. The result of the first stage of Monte Carlo analysis is seen in Figure 2.4, showing all $\langle \varepsilon^{abs} \rangle$ for 20,000 unique parameter sets. In the first stage, k_h (in the form of T) and b are shown to be governing the model accuracy: both trend toward noticeable peaks that are in agreement with the optimised values. The remaining parameters (S, r_w and r_c) show no discernible trend at this stage.

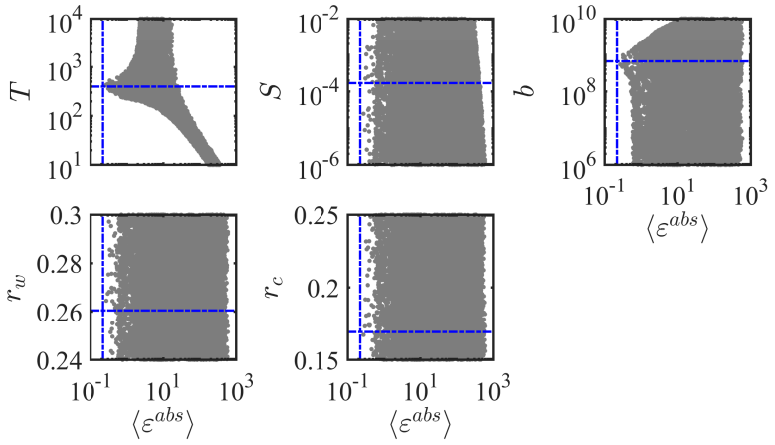

Figure 2.4: Monte-Carlo results for Clark (1977) for the first stage of the progressive procedure (20,000 unique parameter combinations; grey dots) and the position corresponding to best-fit results (blue). A similar illustration was used by Upton et al. (2019) for an unconfined aquifer with varying radius

Following the completion of a stage, the prior and posterior cumulative distribution functions (CDFs) are compared using a standard Kolmogorov–Smirnov test (K-S score). The uniform distribution of the 20,000 sample pool is adopted as the prior CDF and the parameter sets associated with the smallest 1% of $\langle \varepsilon^{abs} \rangle$ scores are isolated to form the posterior CDFs. The K-S score is traditionally used to assess whether an empirical distribution (the posterior) agrees with a hypothesized distribution (the prior). The test is a measure of the maximum vertical distance between two CDFs, with a low score indicating good agreement. Here we reverse the intention of the test, using the highest K-S score of each stage to indicate the leading parameter sensitivity — that is, a narrow and near vertical posterior CDF results from the simulation's accuracy being sensitive to a select parameter's value. Consecutive stages (steps 1–5) are then performed, with each additional stage fixing the previously identified sensitive parameters at their best-fit values from Table 2.1. The maximum $\langle \varepsilon^{abs} \rangle$ from the smallest 1% $\langle \varepsilon^{abs} \rangle$ sample range is calculated for each stage and indicates the contribution that each fixed/calibrated parameter provides to the simulation's accuracy. A summary of the K-S scores and maximum $\langle \varepsilon^{abs} \rangle$ from each stage is provided in Table 2.2.

Variable/Stage	1	2	3	4	5
k_h or T	***0.49***				
S	0.11	0.36	***0.49***		
b	0.21	***0.63***			
r_w	0.03	0.06	0.22	***0.64***	
r_c	0.05	0.07	0.41	0.71	***0.81***
$max(\langle\varepsilon^{abs}\rangle)$	0.76	0.35	0.23	0.22	0.22

Table 2.2: K-S score results of progressive Monte Carlo analysis on SDT data from Clark (1977). The most sensitive parameter of each stage is shown in bold and italic, proceeding to being a fixed parameter at following stages. The maximum $\langle\varepsilon^{abs}\rangle$ from the smallest 1% $\langle\varepsilon^{abs}\rangle$ of the sample range is shown for each stage.

Figure 2.5 shows the results of the five-stage Monte-Carlo analysis for each of the calibration parameters. At the conclusion of the staged analysis, each variable is clearly identified as trending toward a well-defined best-fit value. Confirming the trends observed in Figure 2.4, the accuracy of the solution was mostly attributed to the fluid-flux characteristics, seen directly through the permeability (k_h or T) and Forchheimer parameter (b). The aquifer's storativity (S), well radius (r_w) and casing radius (r_c) are found to be secondary contributors to the simulation's accuracy. The Monte-Carlo results also clearly indicate agreement with suggested best-fit parameters provided by the optimisation of $\langle\varepsilon^{abs}\rangle$, as outlined above.

2.5 Case Study: Royal Festival Hall

We next consider a site with two wells and potentially multiple contributing aquifer layers to assess the viability of grouped-well characterisation and the identifiability of parameters within this more complex setting. The site is a shallow GSHS well-doublet, installed in the English Chalk (EC) aquifer at the Royal Festival Hall (RFH) in south-east England; we refer to this system as 'RFH'.

The design, configuration, and licensing of RFH, as well as the original pump tests and tracer tests, are described in Clarkson et al. (2009). Clarkson et al. (2009) details that the hydraulic performance assessment from the RFH pumping data was originally performed by Gale, Williams, and Mansour (2006). Their results are adopted by Clarkson et al. (2009) for hydrogeological and thermogeological

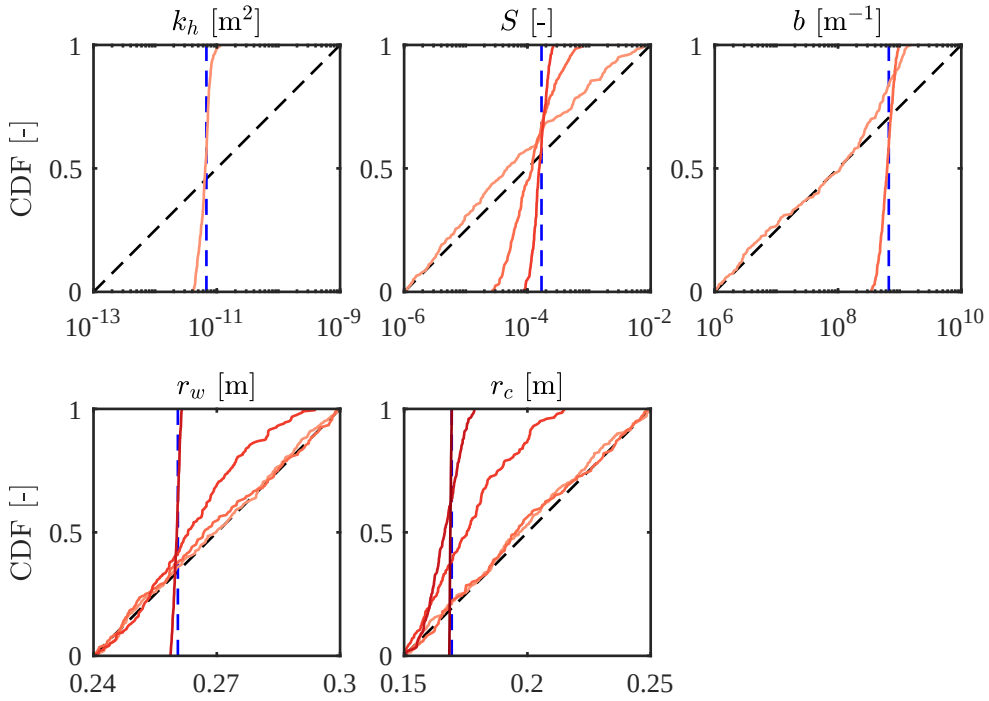

Figure 2.5: Progressive Monte Carlo results for Clark SDT data, showing prior and posterior CDFs for each calibration parameter. The prior in each case is a uniform distribution (dashed black). Increasingly darker shades of red indicate later stages. Calibrated best-fit values are shown in dashed blue.

modelling with `MODFLOW` and `FEFLOW`, including analysis of the tracer tests. The assessments, modelling and conclusions of Clarkson et al. (2009) contribute to thermogeological modelling by Arthur and Streetly (2009) and Arthur et al. (2010), as well as other studies. More recently, elements of the site's operational performance were evaluated by Birks (2019).

The system consists of two wells of 0.3 m diameter, drilled into the EC, approximately 150 m apart. The wells are commonly referred to as BH1 and BH2. Each well was cased from the surface down to 3–5 m into the EC and then extended, uncased, approximately 68 m further.

The geology of the site is described in Table 2.3. Only the EC is in direct hydraulic connection with the uncased well section. The resting groundwater level is found to reside in the uppermost levels of the Woolrich Reading Beds (WRB) and in the London Clay (LC), and appears to have continually risen into the LC due to the overall rising levels within the EC in the region (Environment Agency,

Geological Unit	Description	Depth Range [m]	Approx. Thickness [m]
Made Ground (MG)	Varying deposits	0 - 2.5	2.5
Drift (DR)	Alluvium deposits	2.5 - 7.5	5
River Terrace Gravels (RTG)	Sand & gravel deposits	7.5 - 12.5	5
London Clay (LC)	Stiff blue-grey & grey-brown clay	12.5 - 47.5	35
Woolwich and Reading Beds (WRB)	Mottled clay interbedded with sand and pebbles	47.5 - 62.5	15
Thanet Sands (TS)	Fine-grained sand with some flint beds	62.5 - 72.5	10
English Chalk (EC)	Fractured limestone with abundant flints	72.5 - 140.5	68

Table 2.3: Summary of geological conditions at the RFH site (adapted from Clarkson et al. (2009) and site records). RFH wells are cased from the surface to the top of the EC layer and uncased for the remaining depth of EC.

2018; Birks, 2019). For the purpose of this study, the EC, Thanet Sands (TS) and WRB are considered to be confined by the LC, which acts as an aquitard. Therefore, only the geological units below the LC are considered as potential aquifer layers, contributing flow to the installed wells.

The properties of the EC are well documented (Bloomfield, 1996; MacDonald and Allen, 2001; Allen et al., 1997; Ellison et al., 2004; Sumbler, 1996; Bell, 1977). The EC is typically considered to comprise a high-permeability network of small-aperture (low porosity), semi-continuous, lateral fractures and a low-permeability and moderately high-porosity chalk matrix (Bloomfield, 1996). It is therefore a dual-porosity geological unit: high transmissivity and low storativity fracture network, combined with low transmissivity and high storativity porous matrix (Bloomfield, 1996; Allen et al., 1997). Physical and chemical effects are known to nominally widen fractures within the chalk fracture network causing karstic flow regions, thus adding a third degree of permeability (i.e., porous, fracture and karstic)(Maurice et al., 2006). The frequency of fractures, and thus also the transmissivity, decreases with depth. As a result, aquifer layers below the base of the wells will not be considered. The complex dual-porosity and heterogeneous permeability of the EC are not explicitly captured by the model, which adopts a single effective porosity and permeability for the entire layer. This approach has been shown to be an acceptable modelling simplification for capturing the hydraulic behaviour of the EC and similarly formed aquifers (Freeze and Cherry, 1979; Barker, 1991; Snow, 1968; Domenico, Schwartz, et al., 1998). Note also that the combination of the EC and the TS is the principal aquifer in the London Basin; these layers are differentiated here to capture the isolated well connection within the EC.

Well ID-Test No.	Test Type	Flowrates [l/s]	Time Duration
BH1-1	SDT	5.00, 9.45, 13.89, 18.61, 22.50	1 hr per step + recovery
BH1-2	CRT	22.69	54.17 hrs + recovery
BH2-3	SDT	12.78, 20.00, 23.89	1.5 hr per step + recovery
BH2-4	CRT	23.00	72 hrs + recovery
BH2-5	SDT	9.37, 13.84, 16.61	1.5 hr per step (before failure) + recovery
BH2-6	SDT	1.8, 3.6, 5.4, 7.2, 10.8	Varied

Table 2.4: Summary of pumping tests conducted at RFH, including measured flowrates and test duration. Values are taken or derived from Clarkson et al. (2009), original flowmeter data, or engineering design reports.

Four separate pumping tests were originally conducted to characterise RFH, comprising a CRT and an SDT in each well (tests 1–4). Two additional pumping tests were also performed: a failed SDT on BH2 during the original testing efforts (test 5), disregarded due to pump cut-out/issues, and a separate SDT on BH2 (test 6) performed a year later. All pumping tests are summarised in Table 2.4, and are identified by the well and test number. Tests 1 to 4 are used below for characterisation. Test 5 is used to evaluate the pumping flaw which caused the test to fail. Test 6 is used to assess the evolution of local and regional characteristics by comparison to tests 1 to 4. Unfortunately, neither well was operated as a passive monitoring well at any point.

2.5.1 Single-Well vs. Grouped-Well Hydraulic Characterisation

Considering the hydrogeological conditions, the model will be applied in single-, double- and triple-layer aquifer configurations by progressively including the EC, TS and WRB layers, respectively. As noted above, additional aquifer layers are not considered (i.e., above the WRB or below the base of the well). The model is used to simulate the first four pump tests (tests 1 to 4). Two calibration procedures are considered: Cal.2 and Cal.3 (see Section 2.4.2 and 2.4.3). Both procedures involve calibrating k_h^n, S^n, b^n, k_v^n, r_w and r_c for fixed values of H^n for each layer; Cal. 2 used the observed values of $\hat{Q}$ as given, whereas Cal.3 decouples the steps and can be used to omit periods of flawed data. Site records suggest that the well radius and casing radius are $r_w = 0.15$ m and $r_c \approx 0.13$ m, but we initially allow both values to vary in our analysis.

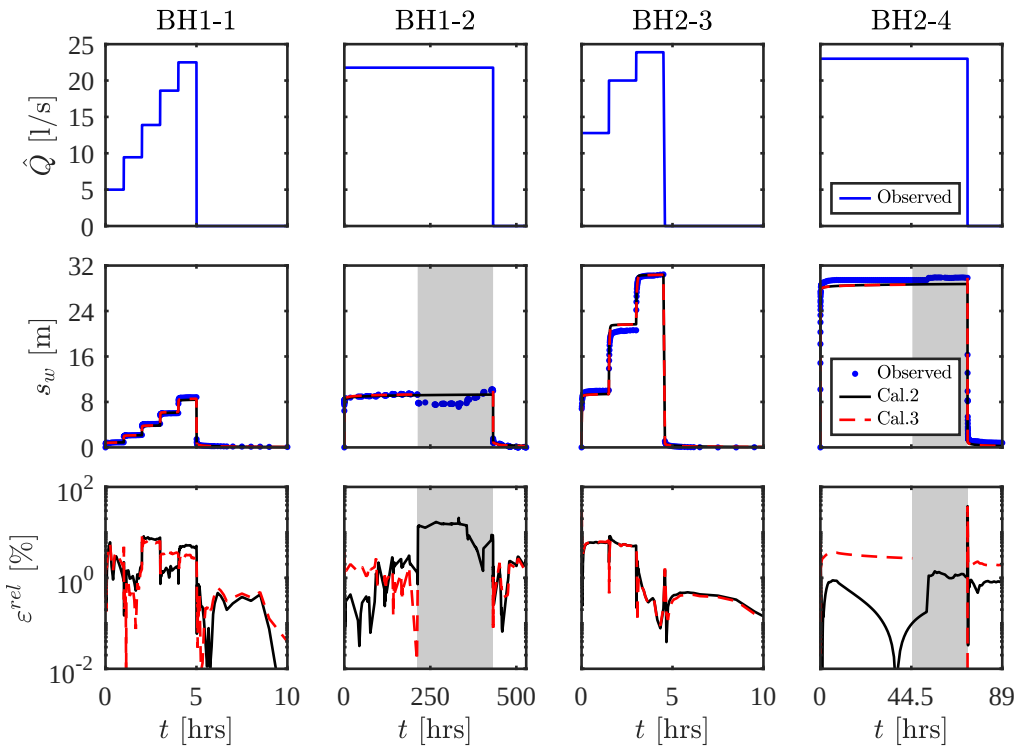

Figure 2.6: Simulation of four pump tests using calibrated parameters for the single-layer model, from Cal.2 (black) and Cal.3 (magenta) compared with observations (blue) along with Cal.3's windows of omission (grey band)

Single-Well Calibration

The two wells are initially calibrated independently, producing two separate sets of calibrated parameters — a standard method. The simulated best-fit drawdown curves from Cal.2 and Cal.3 for the single-layer scenario (EC only) are shown in Figure 2.6. The calibrated parameters for Cal.3 scenarios are summarised in Table 2.5, along with the $\langle \varepsilon^{abs} \rangle$ and $\langle \varepsilon^{rel} \rangle$ results of Cal.2.

Calibrated permeabilities for the TS and WRB are within (although near the upper ends of) the range of previously reported values (Menkiti et al., 2015a; Entwisle et al., 2013; Jones et al., 2000). It remains unclear whether the additional layers can provide significant hydraulic contributions during the timescale of these tests, given that the single-layer model achieves comparable $\langle \varepsilon^{abs} \rangle$ and $\langle \varepsilon^{rel} \rangle$ to the multi-layer models. Note that the horizontal-to-vertical permeability ratios are also consistent with literature values (Menkiti et al., 2015a; Entwisle et al., 2013).

Geology	*Layers*	1				2				3			
	Test No.:	1	2	3	4	1	2	3	4	1	2	3	4
	Test Type:	SDT	CRT	SDT	CRT	SDT	CRT	SDT	CRT	SDT	CRT	SDT	CRT
	Parameter/Well:	BH1		BH2		BH1		BH2		BH1		BH2	
WRB	k_h [m^2]	-				-				4.97E-12		5.24E-12	
	S [-]	-				-				4.69E-05		9.52E-05	
	b [m^{-1}]	-				-				9.55E+07		1.32E+08	
	k_v [m^2]	-				-				5.63E-14		5.95E-14	
TS	k_h [m^2]	-				4.07E-11		4.71E-11		3.69E-11		2.47E-11	
	S [-]	-				4.22E-05		1.00E-05		6.24E-05		1.00E-05	
	b [m^{-1}]	-				2.03E+07		1.21E+08		9.47E+07		8.59E+07	
	k_v [m^2]	-				3.94E-12		5.78E-12		4.06E-12		2.76E-12	
EC	k_h [m^2]	1.90E-11		1.31E-11		1.30E-11		1.26E-11		1.30E-11		1.28E-11	
	S [-]	2.32E-05		1.03E-04		3.34E-04		4.98E-06		8.04E-05		2.35E-05	
	b [m^{-1}]	3.09E+09		1.33E+10		3.01E+09		1.30E+10		3.00E+09		1.31E+10	
	k_v [m^2]	-		-		1.20E-12		1.46E-12		1.58E-12		1.24E-12	
	r_w [m]	0.148		0.158		0.150		0.149		0.150		0.150	
	r_c [m]	0.135		0.129		0.130		0.134		0.131		0.131	
Cal.3:	$\langle\varepsilon^{abs}\rangle$ [m]	0.110	0.124	0.509	0.630	0.110	0.118	0.512	0.609	0.115	0.123	0.500	0.615
	$\langle\varepsilon^{rel}\rangle$ [%]	2.629	1.218	2.993	2.163	2.397	1.158	2.888	2.090	2.643	1.202	2.831	2.111
Cal.2:	$\langle\varepsilon^{abs}\rangle$ [m]	0.130	0.590	0.510	0.590	0.130	0.590	0.530	0.560	0.130	0.590	0.490	0.590
	$\langle\varepsilon^{rel}\rangle$ [%]	2.630	5.831	2.988	2.023	2.376	5.798	2.965	1.916	2.394	5.764	2.844	2.017

Table 2.5: Summary of single-well parameter calibration from Cal.3 for 1, 2 and 3 layer modelling scenarios. Values of $\langle\varepsilon^{abs}\rangle$ and $\langle\varepsilon^{rel}\rangle$ from Cal.2 are shown for comparison.

The calibrations converge on the documented well radius ($r_c = 0.15$ m) and casing radius ($r_c \approx 0.13$ m), providing further verification that the models are identifying known hydraulic mechanisms and their scale of contribution. The identifiability of parameters within particular layers is addressed in the next section.

The usefulness of Cal.3 becomes evident when viewing the imperfect operational data of RFH (see Figure 2.6, grey bands). Site records state that both CRTs experienced pump power supply and tuning issues toward the end of their duration. Similarly, SDTs experienced flow fluctuations as pump operators adjusted equipment to achieve desired test flowrates. Such occurrences are not uncommon in practise, due in part to SDTs often being treated as 'pre-tests' to CRTs, rather than as comprehensive studies in their own right. These operational circumstances make Cal.3 the preferred method of calibration for this particular data set, since it enables the omission of problematic periods without requiring that all subsequent data be discarded. The calibration at RFH benefits from improved accuracy and confidence through Cal.3, as shown by the $\langle\varepsilon^{abs}\rangle$ and $\langle\varepsilon^{rel}\rangle$ in Table 2.5.

Geology	*Layers*	1				2				3			
	Test No.:	1	2	3	4	1	2	3	4	1	2	3	4
	Test Type:	SDT	CRT	SDT	CRT	SDT	CRT	SDT	CRT	SDT	CRT	SDT	CRT
	Parameter/Well:	BH1		BH2		BH1		BH2		BH1		BH2	
WRB	k_h [m^2]	-				-				5.41E-12			
	S [-]	-				-				1.77E-05			
	b [m^{-1}]	-				-				2.13E+08			
	k_v [m^2]	-				-				6.66E-14			
TS	k_h [m^2]	-				4.02E-11				3.75E-11			
	S [-]	-				6.29E-05				2.25E-05			
	b [m^{-1}]	-				2.33E+08				1.06E+08			
	k_v [m^2]	-				7.03E-12				4.66E-12			
EC	k_h [m^2]	1.86E-11				1.31E-11				1.29E-11			
	S [-]	3.12E-05				3.06E-05				6.72E-05			
	b [m^{-1}]	3.16E+09		1.33E+10		2.93E+09		1.31E+10		2.97E+09		1.32E+10	
	k_v [m^2]	-				1.38E-12				1.32E-12			
	r_w [m]	0.152				0.149				0.150			
	r_c [m]	0.133				0.132				0.132			
Cal.3:	$\langle\varepsilon^{abs}\rangle$ [m]	0.110	0.125	0.529	0.618	0.117	0.124	0.509	0.614	0.117	0.130	0.522	0.610
	$\langle\varepsilon^{rel}\rangle$ [%]	2.254	1.228	3.206	2.123	3.065	1.220	2.908	2.107	3.232	1.278	2.995	2.096
Cal.2:	$\langle\varepsilon^{abs}\rangle$ [m]	0.130	0.620	0.560	0.650	0.140	0.590	0.510	0.550	0.130	0.610	0.490	0.570
	$\langle\varepsilon^{rel}\rangle$ [%]	2.899	6.058	3.175	2.245	3.286	5.800	3.002	1.902	2.740	5.984	2.842	1.968

Table 2.6: Summary of grouped-well parameter calibration results from Cal.3, for 1, 2 and 3 layer models. Values of $\langle\varepsilon^{abs}\rangle$ and $\langle\varepsilon^{rel}\rangle$ from Cal.2 are shown for comparison. Cal.2 calibrated parameters comparable but not shown.

Grouped-Well Calibration

As pumping times increase, the observed drawdown behaviour of individual wells in relative proximity becomes increasingly representative of overlapping aquifer regions (Osiensky et al., 2000). The diffusive length scale of each test is calculated from the calibrated hydraulic diffusivity and elapsed pumping times (see Eq.(2.14)). The resulting length scales, expanding radially from the wells, were 2.2, 19.6, 2.1 and 8.2 km for Tests 1 to 4, respectively. These distances imply that the observed drawdown behaviours are representative of an aquifer domain significantly larger than the 150 m between the wells, suggesting that it is potentially unrealistic to assign completely independent aquifer properties for the two wells.

A grouped-well calibration was conducted, assuming in-plane isotropic aquifer properties. The calibration assigned regional values of k_h^n, S^n, k_v^n, r_w and r_c and local well-specific values of b^n (b_{BH1}^n and b_{BH2}^n) in the EC layer (i.e., $n = 1$). The calibrated parameters are summarised in Table 2.6, which also details the comparable values of $\langle\varepsilon^{abs}\rangle$ and $\langle\varepsilon^{rel}\rangle$ from Cal.2 for a grouped-well assessment. The grouped-well calibrations yield comparable parameter values to the single-well approach, and Cal.3 retains its improved accuracy over Cal.2.

Across all calibrations (i.e., single- and grouped-well, single- and multi-layer), Cal.3 suggests a permeability in the EC that is 2.5 to 14.8 times that suggested by Gale, Williams, and Mansour (2006). The technical report by the British Geological Survey (BGS) adopted a linear (Darcy) flow model and determined from the CRTs and a 68 m aquifer height that the transmissivity of the EC layer was 306 and 75 m^2/day for BH1 and BH2, respectively (Gale, Williams, and Mansour, 2006).

The re-evaluation of the site's apparent transmissivity by appreciating the non-linear well behaviour and operating conditions has implications for operational forecasts and thermogeological modelling (see Clarkson et al., 2009; Arthur et al., 2010).

2.5.2 Single- and Grouped-Well, Single- and Multi-layer Aquifer Parameter Sensitivity

A progressive Monte-Carlo approach is now adopted, as above, to assess the identifiability of RFH parameters for single-layer (EC-only) and dual-layer (EC and TS aquifers) grouped-well models using Cal.3. Despite the inclusion of the TS aquifer providing little additional accuracy (see $\langle \varepsilon^{abs} \rangle$ and $\langle \varepsilon^{rel} \rangle$ values in Table 2.6) it remains of interest to assess the identifiability of the parameters in a dual-layer model. The analyses were performed with well and casing radii fixed to their nominal values.

The single-layer aquifer K-S scores are summarised in Table 2.7. Unlike for the Clark (1977) data, the progressive analysis for RFH is more sensitive to the Forchheimer parameter (b_{BH1} and b_{BH2}) than to the permeability (k_h). As for the Clark (1977) data, the storativity is the next parameter of importance after the permeability and Forchheimer terms. These results indicate a greater importance of inertia at RFH in comparison to Clark (1977). The maximum $\langle \varepsilon^{abs} \rangle$ of each stage shows the progressive reduction of increased calibration accuracy as progressively less sensitive parameters are evaluated.

Results for the dual-layer models are summarised in Table 2.8. Figure 2.7 illustrates the posterior CDFs for each parameter prior to being fixed for proceeding stages, for single- and grouped-well models. The progressive analysis again highlights the importance of the Forchheimer parameters of the EC layer (b^{EC}_{BH1} and b^{EC}_{BH2})

Well/s	Variable/Step	1	2	3	4
BH1 Only	k_h	0.48	***0.55***		
	S	0.06	0.29	***0.64***	
	b_{BH1}	***0.60***			
	$max(\langle\varepsilon^{abs}\rangle)$	0.471	0.146	0.119	
BH2 Only	k_h	0.36	***0.49***		
	S	0.06	0.15	***0.50***	
	b_{BH2}	***0.74***			
	$max(\langle\varepsilon^{abs}\rangle)$	1.650	0.702	0.644	
Grouped	k_h	0.38	0.47	***0.52***	
	S	0.04	0.08	0.12	***0.54***
	b_{BH1}	0.22	***0.62***		
	b_{BH2}	***0.76***			
	$max(\langle\varepsilon^{abs}\rangle)$	2.346	0.975	0.444	0.421

Table 2.7: Summary of K-S test values of single-layer aquifer (EC-only) with single- and grouped-well models, for progressive Monte Carlo analysis. The maximum $\langle\varepsilon^{abs}\rangle$ from the smallest 1% $\langle\varepsilon^{abs}\rangle$ of the sample range is shown for each stage.

over the horizontal permeability (k_h^{EC}). The progressive analysis next emphasised the horizontal permeability (k_h^{TS}) and storativity coefficients (S^{EC} and S^{TS}). The variables with the lowest significance are the vertical permeability and the Forchheimer parameter of the TS layer (b^{TS}). This suggests negligible inertial effects in the TS layer, which is reasonable since much lower flow velocities are expected in the TS layer, and that the TS layer provides minimal volumetric contribution to the drawdown. In most cases, the horizontal permeability and storativity of the second layer (k_h^{TS} and S^{TS}) are identified prior to the storativity of the primary layer. The later two observations suggests the model identifies marginal benefits from the second layer's hydraulic diffusivity, despite the layer's Forchheimer parameter sensitivity. Within the grouped-well models, the greatest Forchheimer value dominates the grouped calibration process. Once this value is identified the remaining parameters can be determined.

The calibration results show that the inclusion of additional layers leads to a marginal reduction in $\langle\varepsilon^{abs}\rangle$ relative to the single-layer model, but this small improvement comes at the cost of several additional degrees of freedom. Physically, the presence of additional layers appears to allow the EC to have slightly lower

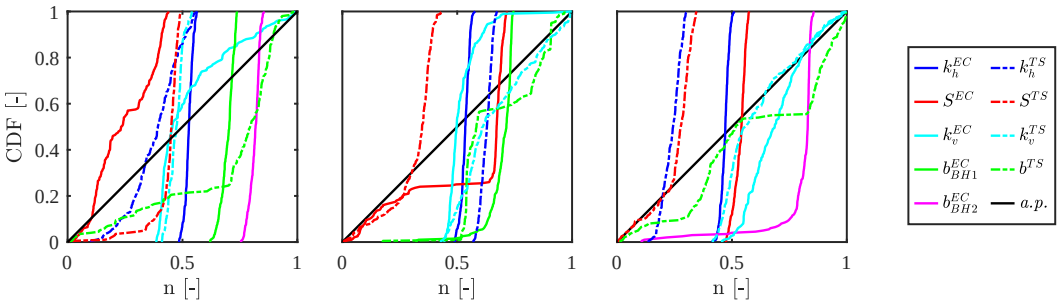

Figure 2.7: Illustration of parameter CDFs for a dual-layer progressive Monte-Carlo analysis, showing grouped-well (left), BH1-only (middle) and BH2-only (right) models. CDFs correspond to parameters at the stage prior to being fixed at their best-fit values. Parameter CDFs normalised with respect to the lower and upper bound of the prior distribution, denoted by n [-].

Well/s	Geology	Variable/Stage	1	2	3	4	5	6	7	8	9
BH1 Only	TS	k_h	0.08	0.20	***0.56***						
		S	0.06	0.14	0.50	***0.57***					
		b	0.07	0.10	0.05	0.04	0.15	0.46	***0.51***		
		k_v	0.07	0.05	0.04	0.16	0.05	0.10	0.37	***0.43***	
	EC	k_h	0.39	***0.49***							
		S	0.05	0.08	0.24	0.29	***0.38***				
		b_{BH1}	***0.56***								
		k_v	0.06	0.05	0.09	0.17	0.54	***0.44***			
		$max(\langle\varepsilon^{abs}\rangle)$	0.475	0.171	0.124	0.119	0.119	0.119	0.119	0.118	
BH2 Only	TS	k_h	0.04	0.37	0.64	0.63	***0.69***				
		S	0.06	0.11	***0.65***						
		b	0.06	0.06	0.11	0.10	0.07	0.10	0.13	***0.27***	
		k_v	0.04	0.04	0.06	0.05	0.17	***0.42***			
	EC	k_h	0.24	***0.49***							
		S	0.07	0.04	0.44	***0.47***					
		b_{BH2}	***0.65***								
		k_v	0.03	0.08	0.06	0.04	0.14	0.30	***0.48***		
		$max(\langle\varepsilon^{abs}\rangle)$	1.524	0.717	0.646	0.646	0.644	0.644	0.644	0.644	
Grouped	TS	k_h	0.09	0.07	0.28	***0.44***					
		S	0.04	0.06	0.11	0.44	***0.51***				
		b	0.09	0.05	0.14	0.03	0.05	0.06	0.06	0.06	***0.46***
		k_v	0.05	0.05	0.04	0.06	0.20	0.15	0.15	***0.46***	
	EC	k_h	0.34	0.43	***0.49***						
		S	0.05	0.08	0.04	0.26	0.31	***0.56***			
		b_{BH1}	0.22	***0.62***							
		b_{BH2}	***0.75***								
		k_v	0.06	0.04	0.09	0.19	0.26	0.39	***0.39***		
		$max(\langle\varepsilon^{abs}\rangle)$	2.314	0.983	0.468	0.422	0.419	0.417	0.417	0.417	0.417

Table 2.8: Summary of K-S test results from progressive Monte Carlo analysis using a dual-layer aquifer with single- and grouped-well models. The maximum $\langle\varepsilon^{abs}\rangle$ from the smallest 1% $\langle\varepsilon^{abs}\rangle$ of the sample range is shown for each stage.

	$\hat{Q}_{cal}$ [L/s]		
Step	Grouped-well	BH2-only	BH2-4 only
1	12.60 (35.5%)	12.42 (32.6%)	12.49 (33.3%)
2	17.71 (27.9%)	17.65 (27.5%)	17.63 (27.4%)
3	21.33 (28.4%)	21.31 (28.3%)	21.29 (28.3%)
$\langle \varepsilon^{abs} \rangle$ [m]	0.358	0.360	0.291

Table 2.9: Summary of re-calibrated averaged step flowrates, $\hat{Q}_{cal}$. The ε^{rel} of the calibrated flows to flawed reported flows ($\hat{Q}_o$) is documented in brackets. The reported $\langle \varepsilon^{abs} \rangle$ is of the newly simulated drawdown curve to observed drawdown data.

permeability. The calibrated parameters and assessed sensitivities of the dual-layer model are consistent with the mechanics of a 'leaky' confined aquifer. The $max(\langle \varepsilon^{abs} \rangle)$ are consistent with the expected hydraulic behaviour of the TS and WRB layers overlying the EC (Allen et al., 1997; Bloomfield, 1996; Ellison et al., 2004). Given the marginal volumetric contribution and error reduction, we deem a single-layer model to be most appropriate for RFH.

2.5.3 Re-calibration of Flowrate

During initial site testing, a failed SDT occurred prior to test BH2-3. The pump was reported to have prematurely stopped during the third step due to unspecified difficulties; as a consequence, the data was disregarded. The pumping issue was addressed, allowing for the site works to continue with tests BH2-3 and BH2-4. We next use the calibrated model (see Table 2.5 and 2.6) to analyse the pumping data, assessing the nature of the pumping flaw and whether the data can be salvaged for inclusion with the other pumping tests.

To do so, the failed test BH2-5 is simulated as a single-layer aquifer with known values of k_h, S, b, r_w, r_c, H and s_w, and unknown $\hat{Q}$. The average flowrate for each step is then calibrated to produce a best-fit drawdown curve. Three different parameter sets from Tables 2.5 and 2.6 were considered: the grouped-well parameters (BH1-1, BH1-2, BH2-3 and BH2-4 combined), the BH2-only parameters (BH2-3 and BH2-4 combined), and the BH2 CRT-only parameters (from test BH2-4). The results for each of these cases are shown in Figure 2.8 and summarised in Table 2.9.

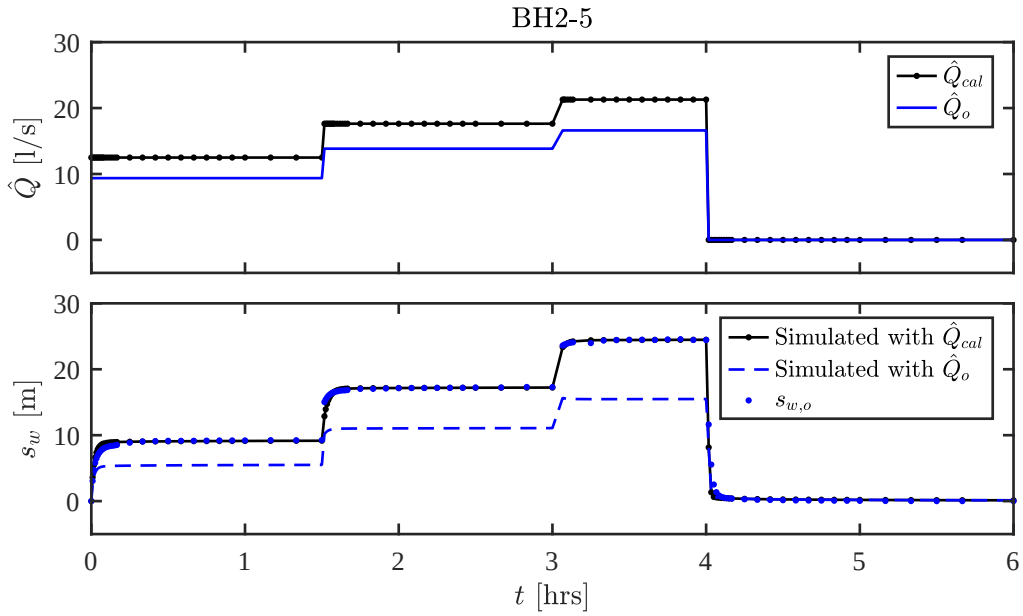

Figure 2.8: Comparison of calibrated and re-calibrated best-fit simulations for test BH2-5, based on single-layer aquifer parameters calibrated with test BH2-4 (see Table 2.5). The top panel shows the reported and calibrated average flow rates ($\hat{Q}_o$ and $\hat{Q}_{cal}$, respectively). The bottom panel shows the initial drawdown simulation based on $\hat{Q}_o$, the simulated drawdown based on $\hat{Q}_{cal}$, and the observed drawdown.

The exact nature of the pumping error is not known due to a lack of records specific to the issue. However, the results indicate that the error was a relatively consistent under-measurement of the flowrate by about 30% across the testing period. A variety of mechanical issues can cause pumps to stop during operation (e.g., debris or cavitation), whereas few would cause a consistent increase in flow not detected by a flowmeter (Yedidiah, 2012). Therefore, it is inferred that the flowmeter suffered a calibration error and thus that the pump was operating at higher flowrates than reported during the SDT. The inability to conclusively determine the fault means that the BH2-5 SDT should not be used directly in calibration of hydraulic properties. However, the ability of the calibrated model to infer the flowrates for BH2-5 with relatively consistent error serves as an indirect validation of the prior calibrations based on BH1-1 to BH2-4.

		$\langle \varepsilon^{rel} \rangle$ (%)							
Re-Cal.	***Description/Flow Step***	***1***	***2***	***3***	***4***	***5***	***6***	***7***	***Wt.*** $\langle \varepsilon^{rel} \rangle$ ***(%)****
-	Original BH2 Parameters Applied	26.61	25.56	22.23	29.10	3.65	28.66	2.51	27.30
1	Incorrect Flows Reported	18.17	4.58	3.39	6.28	4.38	2.17	2.18	5.30
2	Change in well characteristics	21.97	5.57	3.88	10.57	4.55	2.08	1.63	6.34
3	Change in aquifer and well characteristics	22.38	6.19	3.76	10.71	4.71	2.08	1.56	6.49

*Omitting recovery periods (steps 5 & 7) due to zero flowrates

Table 2.10: $\langle \varepsilon^{rel} \rangle$ by flow step of BH2-6 for each re-calibration effort. The weighted average of the combined steps is calculated based on the number of data points recorded in each step, omitting recovery periods (steps 5 and 7).

Re-Calibration	2^{nd}	3^{rd}		
Parameter	b_{BH2} [m^{-}1]	b_{BH2} [m^{-}1]	k_h [m^2]	S [-]
Calibrated	1.33E+10	1.33E+10	1.31E-11	1.04E-04
Re-calibrated	2.17E+10	2.19E+10	1.37E-11	1.23E-04
% difference	63.2%	64.7%	4.6%	18.3%

Table 2.11: Summary of key variable changes in aged-well analysis. The second and third re-calibration efforts are observed to rely heavily on altering the Forchheimer parameter, despite their differing variable freedoms.

2.5.4 Aged Well Analysis

One year after the initial calibration efforts, RFH was subject to another SDT (BH2-6) to assess the ability of BH2 to act as an injection well, having previously been designated for abstraction only. The SDT was performed by site engineers at various flowrates with two recovery periods. The SDT was simulated using calibrated parameter values from the BH2-only characterisation for a single-layer aquifer using Cal.3 (BH2-3 and BH2-4; see Table 2.5). The results suggests that, for a given flowrate, the well is experiencing a 27.3% increase in drawdown compared with pump tests the year prior. This increase is considered a reduction in well performance (see Table 2.10). A similar result was observed when using calibrated values from the grouped-well characterisation (based on BH1-1 to BH2-4; see Table 2.6). To capture this change in hydraulic performance over time, the model is used to perform a re-calibration of parameters to assess which have evolved in time. Three different re-calibration approaches were assessed, each testing a different hypothesis. The results are summarized in Figure 2.9 and Tables 2.10 and 2.11, and described below.

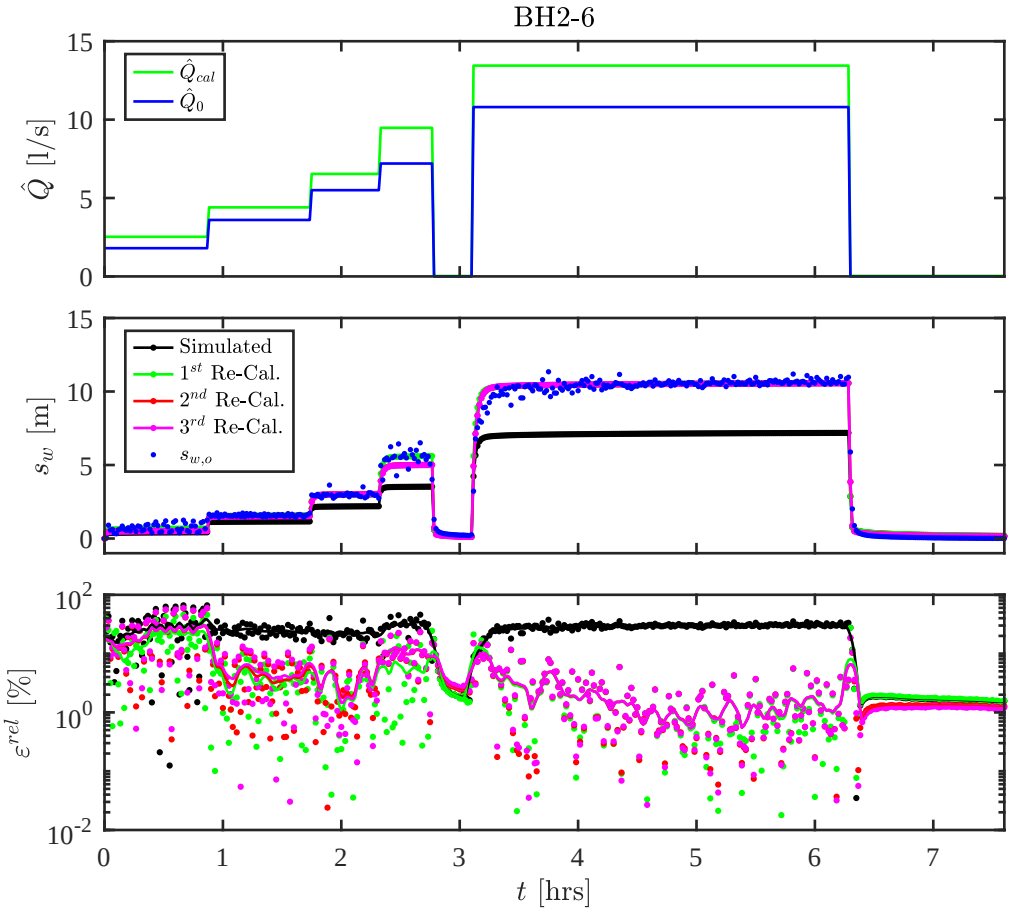

Figure 2.9: Best-fit Transient Analysis for Aged Well, test BH2-6, RFH. The top panel shows the reported average flowrates ($\hat{Q}_o$) compared with averaged flowrates suggested by the recalibration ($\hat{Q}_{cal}$, 1^{st} re-calibration effort). The middle panel illustrates the ability of the model to fit the observed drawdown data for each re-calibration effort. The bottom panel shows the ε^{rel} of each simulated drawdown curve as discrete points and as 3-point moving average.

1^{st} Re-calibration: a flawed flowmeter

The first re-calibration assumed that the reported averaged flowrates were flawed. As in Section 2.5.3, we therefore fixed all parameters and allowed $\hat{Q}$ to vary. The result was a reasonable match to the observations, but the errors in the flowrate were inconsistent, ranging from 21.1 to 40.6% greater than those initially reported. Records also indicate that site operations independently calibrated flowrates with an ultra-sonic flowmeter, so it is unlikely that the observed deviations are due to flawed reported flowrates.

2nd Re-calibration: a change in local aquifer parameters

It is possible that the permeability and storativity evolved due to physical and chemical weathering of the EC (Maurice et al., 2006; Butler et al., 2009). It is also possible that converging flow paths around the well have accelerated these weathering processes local to the well. We expect changes in the regional aquifer to be shown by changes in the calibrated permeability and storativity values, while changes in the local aquifer (near the well) will be reflected in changes to the Forchheimer parameter. Changes to the well and casing radii are not considered since they are regarded as physically unlikely and prior assessments have shown the simulations to be relatively insensitive to these parameters in comparison to the Forchheimer parameter.

Therefore, the second re-calibration assumed that the aquifer local to the well had deteriorated in time and a new Forchheimer parameter (b_{BH2}) would adequately account for the observed change in behaviour. The regional aquifer properties of permeability and storativity were fixed, and the reported flow rate ($\hat{Q}_o$) was adopted. The model is shown to achieve a fairly low relative error, having used its single degree of freedom to increase the Forchheimer parameter by 63.2%.

3rd Re-calibration: a change in both local and regional aquifer parameters

The third re-calibration assumed both the local and regional aquifer properties had changed in time, requiring entirely new parameter calibrations (k_h, S and b_{BH2}). A simulated fit with slightly greater relative error to the second re-calibration effort is observed in Table 2.11. The results reported in Table 2.11 omitted recovery period in test BH2-6. If included, the 3rd re-calibration effort results in marginally less relative error than the second re-calibration. Despite the additional freedoms of the model to change the regional aquifer properties, little change is observed. Again, the predominant change is within the Forchheimer parameter, arriving at a very similar value to that suggested by the second re-calibration effort. The second greatest change comes from the storativity parameter. This parameter has a strong impact on the early-time shape of the drawdown curve and thus its change may partly be

explained by the model's desire to fit the unusual early-time shape observed in the final pumping step (step 6, between hours 3 and 4). This is an unusual early-time drawdown curve in comparison to all previous RFH data analysed here. The curve suggests that the pump flow was gradually increased instead of stepped relatively quickly, but site records only report averaged flowrates instead of incremental flowmeter data, meaning this assertion cannot be more strictly confirmed.

The small changes in the k_h and S suggest that changing the regional aquifer characterisation appears largely unwarranted. In contrast, the larger change in the Forchheimer parameter suggests a small amount of near-well deterioration can result in large changes to inertial losses. Together, these observations highlight the usefulness of the DF equation in expressing local characteristics and their evolution. Further ground survey and investigation would be required to confirm the causes of the observed drawdown behavioural change.

2.6 Discussion and Conclusions

A simple model based on the Darcy-Forchheimer equation was constructed for analysing single- and grouped-well pumping tests in a confined aquifer. Three calibration procedures were introduced and used to characterise hydraulic properties from the pumping tests, via an optimisation algorithm which minimised the mean absolute error between simulated and observed drawdown data. The first two calibration procedures differed in the parameters that were allowed to vary: Cal.1 calibrated k_h, S and b, with fixed r_w, r_c, H and $\hat{Q}$, while Cal.2 additionally calibrated r_w and r_c. The third procedure, Cal.3, used the same degrees of freedom as Cal.2 but added a novel variation to separate individual pumping steps and omit periods of testing data to avoid human- and instrumental-error.

The calibration procedures were applied to a SDT in a single-layer aquifer, originally published by Clark (1977), as a benchmark. Calibrated values were similar to the values calculated by the analytical/empirical methods of Clark (1977) and the numerical results by Mathias and Todman (2010).

The sensitivity of the calibrated values was assessed with a progressive Monte-Carlo analysis. The analysis was performed by progressively fixing the most identifiable parameter after each iteration. For the Clark (1977) data, the analysis found the order of identifiability to be the permeability (k_h), the Forchheimer parameter (b), storativity (S), well radius (r_w), and well casing radius (r_c). The results of the combined analyses indicate that the optimisation algorithm successfully identified the best-fit parameters.

The model was then applied to Royal Festival Hall (RFH): a site with two wells 150 m apart and six pump tests in a potentially multi-layer aquifer. RFH data was used to assess whether two wells, a relatively small distance apart, could be calibrated under the same regional aquifer properties (permeability and storativity) or whether each well required unique properties. The properties of the local and regional aquifer were assessed for one-, two- and three- layer aquifer models. The novel Cal.3 approach was shown to be more accurate than Cal.2 due to operational errors/complexities in the RFH data. The grouped-well model produced comparable calibrated parameters and error to the single-well model, resulting in common regional aquifer parameters (k_h, S and k_v) and unique localised aquifer properties (b_{BH1} and b_{BH2}). These results emphasise the necessity for practitioners to account for non-linear head-losses when calibrating hydraulic properties from pumping tests.

The sensitivity of the simulation to parameter values and the identifiability of each parameter was assessed by progressive Monte-Carlo analysis on single- and dual-layer models, for single- and grouped-well configurations. Differing from the Clark (1977) data, the analyses showed that simulations were most sensitive to the Forchheimer parameters of each well, resulting in b_{BH1} and b_{BH2} being strongly identifiable. The parameters of the second aquifer layer were shown to be identifiable prior to some parameters of the primary layer, despite no direct connection to the well. In each of the analyses, the parameters were shown to be identifiable and contribute a degree of sensitivity to the simulated drawdown curve. Additionally, the results agreed with calibrated best-fit identified by the optimisation algorithm.

The calibrated parameters from single- and grouped-well, single-layer models for RFH were then applied in an analysis of a disregarded, failed pump test. The pump test was found to most likely have suffered from both a pump cut-out and flawed flowmeter measurements. The calibrated parameters were successfully used to re-calibrate averaged flowrates for the test.

Finally, the calibrated hydraulic properties at RFH were used to analyse a further SDT, conducted a year after the original calibration tests. Calibrated parameters were found to no longer accurately simulate the observed drawdown of the new test, which showed a $\sim$27.3% increase in drawdown for a given flowrate. A re-calibration procedure was conducted to identify which parameter values had evolved during the elapsed year between tests. The re-calibration of the Forchheimer parameter (b) was found to most successfully account for the change, followed by small changes in permeability (k_h) and storativity (S). It was suggested that this represented physical changes to the localised aquifer near the well, suggesting that the regional aquifer had not experienced the same degree of change. However, it is possible that this is merely a reflection of the sensitivity of the Forchheimer parameter in the RFH calibration.

The presented calibration procedures show strong promise for aiding practitioners in quickly performing site-specific characterisation of hydraulic properties based on pump test. These procedures might be adopted in preference to literature-based values and applied in platforms such as `MODFLOW` and `FEFLOW` for more detailed site-specific modelling. The novel Cal.3 process is particularly valuable as it can be used to assess pump tests which have experienced periods of error. Likewise, the ability to calibrate parameters in a grouped-well configuration avoids the need to divide an aquifer into arbitrary sub-domains with distinct properties. However, the level of manual data acquisition, processing and cleaning required to perform the presented analyses would currently be vastly inefficient outside of a research-based environment.

2.7 Acknowledgements

Thanks to Prof. Simon Mathias (Durham University), Em.Prof. John Barker (University of Southampton), David Banks (SRF, University of Glasgow), and Dr. David Birks for their insight and discussion. Thanks to Mr. Hilton Wells and the South Bank Centre for their contribution and support of research into Royal Festival Hall.

3

Solute Transport Characterisation

Contents

3.1 Introduction

Following the characterisation of the apparent hydraulic properties of the EC aquifer at RFH (see Chapter 2), the design engineers performed a characterisation of the associated solute transport properties. The purpose of this characterisation is to identify the apparent effective porosity of the aquifer and the apparent dispersion and diffusion characteristics. These properties inform forecasts of the thermal performance of the aquifer under GSHS operating conditions, which themselves enable evaluation of the physical and financial feasibility of the GSHS. As well as informing parameterisation, the solute transport tests help to identify the presence of

a hydraulic 'short circuit' between nearby wells due to a high-permeability pathway such as a fracture. These 'short-circuits' can lead to rapid transit of effluent water between injection and abstraction wells, which can severely compromise the performance of an open-loop GSHS. The solute transport test at RFH is presented and discussed in Clarkson et al. (2009). Clarkson et al. (2009) describe the original testing and modelling using `MODFLOW/MT3D` and proceeded to conduct their own thermal modelling and analysis using `FEFLOW`.

In Chapter 2, it was found that the apparent hydraulic properties suggested by calibration against the available pump test data and operational notes differed greatly from those adopted by RFH design engineers. In this chapter, we revisit the solute transport tests that were conducted at RFH. A simplified 2D solute-transport model is developed and used to calibrate the apparent transport properties of the host aquifer by comparing simulated and observed test results. The results of Chapter 2 indicated little to no volumetric contribution from additional layers above the EC aquifer (e.g., the TS and WRB); therefore, the solute transport model adopts a single-layer approach. The identifiability of the best-fit parameters is also considered.

The re-analysis of the RFH tracer test and calibration follows the hypothesis that incorrect assumptions, modelling or testing may have underpinned inaccurate thermal breakthrough predictions at RFH. More precisely, its envisaged that injected effluent fluid is responsible for the thermal breakthrough and that a re-calibration of transport properties may solve the disagreement between predicted and observed behaviour.

3.1.1 Tracer Tests at Royal Festival Hall

The full details of the tracer tests, as published in Clarkson et al. (2009), are summarised below.

The GSHS at RFH was designed and licensed in 2006 with the intention of abstracting water from the EC via both BH1 and BH2 and then discharging the effluent fluid into the River Thames. In 2007, the system was re-designed to operate as a well-doublet, with abstraction at BH1 and injection at BH2. For this purpose,

the design engineers at RFH conducted a second round of pump testing in 2007 to evaluate the potential to use BH2 for injection.

Tracer testing was performed by a well-doublet method. This method involves pumping a pair of wells at equal and opposite flow rates, injecting a solute tracer into one and monitoring the concentration of tracer abstracted at the other. Two tests were performed at RFH with tracers: a sodium chloride test and a fluorescein test. Both tests were conducted during an approximately month-long period of constant-rate pumping, with solute injected via BH2 and monitoring and sampling conducted via BH1.

The sodium chloride tracer test was conducted on 25 June 2007, several days after the commencement of constant-rate pumping, to test for the presence of a short-circuit between the two wells. The monitoring involved measuring the conductivity of the abstracted water; the results are published in Clarkson et al. (2009). The observed changes in conductivity were within the range of typical background variation. The lack of a distinct, measurable breakthrough was taken to mean that no short-circuit was present. The sodium chloride tracer test is not discussed further in this chapter and therefore 'tracer' is adopted to solely refer to the fluorescein tracer test.

The fluorescein tracer test was conducted on 28 June 2007, 8 days after the commencement of constant-rate pumping. Pumping rates were reported to be approximately 8.3 L/s. A 15 g mass of tracer contained within 242 mL of solution was introduced into a bypass chamber and then released into the main discharge pipeline for injection into BH2. Fluorescein levels at BH1 were monitored with a Seapoint Fluorescein Fluorometer from 20 June 2007, gathering background concentration readings prior to the test. In addition to the fluorometer readings, more than 100 samples were collected from abstracted fluid for laboratory analysis at regular intervals during the test.

Breakthrough at BH1 began approximately 4.5 hours after the start of fluorescein injection. Peak concentration was measured 14 hours after initial breakthrough. Fluorescein concentration at BH1 returned to background levels approximately

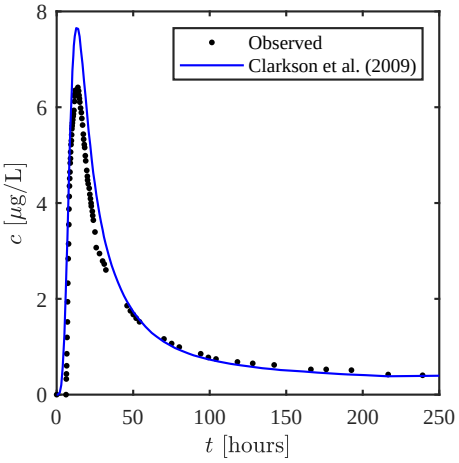

Figure 3.1: Comparison of observed tracer breakthrough data with best-fit `MODFLOW/MT3D` simulation results of Clarkson et al. (2009)

4 days after the start of the test (according to fluorometer readings). Laboratory analysis of samples indicate the return to background levels by approximately 11 July 2007 (13 days) and take precedence due to concerns over precipitations observed on the fluorometer (Clarkson et al., 2009). Clarkson et al. (2009) estimated that 20.6% to 40.97% of the injected tracer mass was recovered at BH1 by integrating the breakthrough curve with respect to time. Clarkson et al. (2009) simulated the tracer test using a 3D `MODFLOW/MT3D` model, adopting the hydraulic parameters from Gale, Williams, and Mansour (2006) and literature. Clarkson et al. (2009) report that they allowed their `MODFLOW/MT3D` model to calibrate a simulated tracer curve to the observed results, iterating the program over a period of 7 days. They assumed that the tracer was conservative and non-dispersive, with negligible diffusion into the EC matrix. Their best-fit calibration resulted from assigning 100% of the transmissivity of the EC to its uppermost 5 m and adopting an effective porosity of 0.0025. A comparison of the observed and simulated breakthrough curves is shown in Figure 3.1.

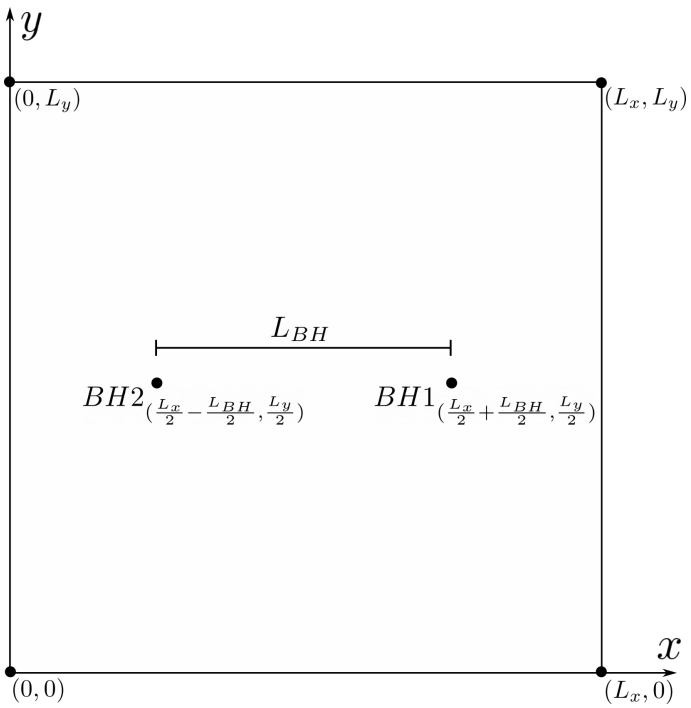

Figure 3.2: Model schematic illustrating the square horizontal domain with two wells. During the CRT and tracer test at RFH, fluid and solute are injected at BH2 and abstracted at BH1.

3.2 Modelling Approach and Governing Equations

A 2D model is constructed to represent the horizontal plane of a single-layer confined aquifer, with two wells positioned within the domain. The model is used to simulate the transport of the fluorescein tracer within the domain under a well-doublet flow field, assuming steady-state flow conditions. The model assumes that the aquifer is continuous, homogeneous, isotropic, horizontal, of uniform thickness, and confined by impermeable and non-absorbing strata. As a result, flow and transport are horizontal only.

3.2.1 Assumption of Steady-state flow

The 2D transport model assumes steady-state flow conditions within the domain. This assumption allows the governing equations to be simplified from what would otherwise be a coupled transient pressure-transport model, eliminating domain-size and time-stepping constraints related to pressure evolution. To show that

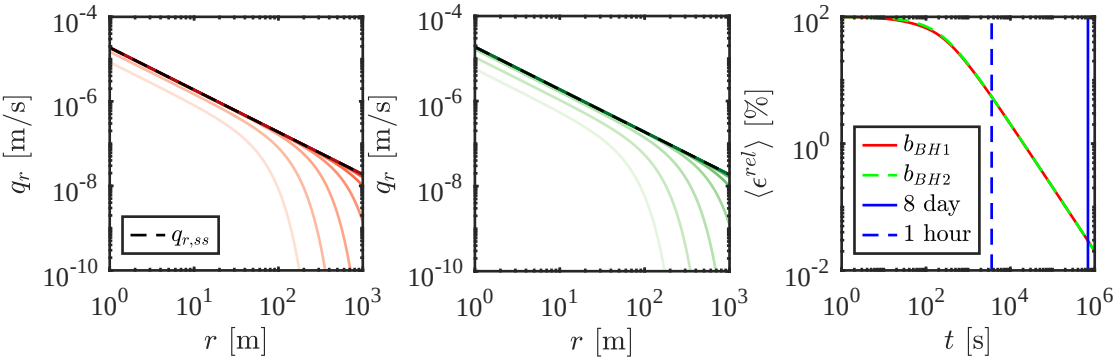

Figure 3.3: Comparison of $q_{r,ss}$ and $q_{r,DF}$ given the Forchheimer parameters of BH1 (left panel) and BH2 (middle panel), for various points in time and a domain of $r_w \rightarrow r_\infty$. Both panels show ten points spaced logarithmically in time from $t = 0$ to 1E6 (shades of light to dark, respectively), with later times converging over $q_{r,ss}$ (black, dashed). Right panel shows the $\langle \epsilon^{rel} \rangle$ between $q_{r,DF}$ and $q_{r,ss}$ for $t \leqslant 1E6$ [s] and both Forchheimer parameters.

this assumption is reasonable, given the size of the domain and the duration of the tracer test, three fluxes are compared: the 1D radial steady-state flux ($q_{r,ss}$), and the 1D transient Darcy-Forchheimer (DF) fluxes ($q_{r,DF}$) of each of the two wells. The radial steady-state flux is

$$q_{r,ss} = \frac{-\hat{Q}}{2\pi r H}. \tag{3.1}$$

where r is the radial distance from the well, $\hat{Q}$ [L^3T^{-1}] is the imposed pumping rate and H [L] is the height of the aquifer. The transient DF fluxes are calculated by using the radial model from Chapter 2 and the calibrated single-layer aquifer parameters (see Table 2.6). The transient fluxes are evaluated and compared against the steady-state flux for the duration of a $1E6$ second CRT (Figure 3.3). Calculations assessed points isolated to the relevant domain by comparing the fluxes at 1000 evenly spaced points between $r_w = 0.15$ m and $r = 1$ km, linearly interpolating from the 1D log-grid spanning r_w to r_∞.

The transient and steady-state fluxes converge over time and more rapidly at larger values of r. At the commencement of the main tracer test, 8 days after the start of the CRT, the mean relative difference between $q_{r,ss}$ and $q_{r,DF}$

is <0.03% for both wells. We therefore consider the steady-state assumption to be acceptable for this tracer test.

The flux components q_x and q_y for a single well at point (x_{well}, y_{well}) are

$$\begin{aligned} q_x(x,y) &= q_r \cos\theta = \frac{\hat{Q}}{2\pi H} \frac{x - x_{well}}{(x - x_{well})^2 + (y - y_{well})^2} \\ q_y(x,y) &= q_r \sin\theta = \frac{\hat{Q}}{2\pi H} \frac{y - y_{well}}{(x - x_{well})^2 + (y - y_{well})^2} \end{aligned} \tag{3.2}$$

where $\theta = \tan^{-1}(y/x)$ [rad]. For a mass conservative flow in 2D Cartesian domain, the mean flux through each grid-cell edge must be calculated (see Appendix A for finite-volume method and grid naming conventions). For a grid with centred indices (i, j), where x varies with i and y varies with j, the fluxes at an arbitrary edge $(i + 1/2, j)$ are given by:

$$\begin{aligned} \bar{q}_{x_{i+1/2,j}} &= \frac{-\hat{Q}}{2\pi H \delta y} \tan^{-1}\left(\frac{y}{x}\right) \Big|_{x_{i+1/2,j-1/2},\, y_{i+1/2,j-1/2}}^{x_{i+1/2,j+1/2},\, y_{i+1/2,j+1/2}} \\ \bar{q}_{y_{i+1/2,j}} &= \frac{-\hat{Q}}{2\pi H \delta x} \tan^{-1}\left(\frac{y}{x}\right) \Big|_{x_{i,j},\, y_{i,j}}^{x_{i+1,j},\, y_{i+1,j}} \end{aligned} \tag{3.3}$$

Where multiple active wells exist within the model domain, the 2D flow field can be derived by superposing the axisymmetric flow fields of the individual wells.

3.2.2 Solute Transport

Solute transport is assumed to take place within the fracture network of the EC, volumetrically modelled as the effective porosity of the aquifer, with no diffusion into the rock matrix. Solute transport occurs via advection, diffusion, dispersion and sorption to the fracture walls. The 2D domain is illustrated in Figure 3.2. Conservation of solute mass can then be written as (see Nield, Bejan, et al., 2006):

$$\phi_e \frac{\partial c_w}{\partial t} + \underline{\nabla} \cdot \left(\underline{q} c_w - \phi_e \underline{\underline{D}}_w \cdot \underline{\nabla} c_w\right) - \mathcal{I}_c - D_s(c_s - c_w) = 0 \tag{3.4}$$

and

$$\phi_s \frac{\partial c_s}{\partial t} - D_s(c_s - c_w) = 0, \tag{3.5}$$

where ϕ_e [-] is the effective porosity of the fracture network (fracture volume per unit bulk volume), c_w [ML^{-3}] is the solute concentration in the fracture network in excess

of background (mass of dissolved solute per unit volume of water), $\underline{q}$ [LT^{-1}] is fluid flux, $\mathcal{I}_c$ [$\mathrm{ML}^{-3}\mathrm{T}^{-1}$] is the solute source/sink at the wells, ϕ_s [-] is the effective porosity available for sorption (volume containing sorbed solute per total volume), c_s [ML^{-3}] is the sorbed solute concentration, D_s [T^{-1}] is the sorption coefficient, and $\underline{\underline{D}}_w$ [$\mathrm{L}^2\mathrm{T}^{-1}$] is the diffusive/dispersive tensor in the fracture network. The latter is expressed as

$$\underline{\underline{D}}_w = \begin{bmatrix} D_{xx} & D_{xy} \\ D_{yx} & D_{yy} \end{bmatrix}. \tag{3.6}$$

We model the dispersion tensor (Bear, 1961; Scheidegger, 1961; De Jong and Bossen, 1961), so that

$$D_{xx} = D_0 + \frac{1}{\phi_e |\mathbf{q}_w|}(\alpha_L q_{w,x}^2 + \alpha_T q_{w,y}^2), \tag{3.7}$$

$$D_{yy} = D_0 + \frac{1}{\phi_e |\mathbf{q}_w|}(\alpha_T q_{w,x}^2 + \alpha_L q_{w,y}^2), \tag{3.8}$$

$$D_{xy} = D_{yx} = (\alpha_L - \alpha_T)\frac{|q_{w,x} q_{w,y}|}{\phi_e |\mathbf{q}_w|}, \tag{3.9}$$

where D_0 [$\mathrm{L}^2\mathrm{T}^{-1}$] is the molecular diffusivity of the tracer and α_L [L] and α_T [L] are the longitudinal and transverse dispersion coefficients, respectively. Going forward, we assume for simplicity that the effective sorption volume of the rock surface is equal to the effective fracture volume so that $\phi_e = \phi_s$. Although not rigorously justified, this assumption is physically reasonable for a network of small-aperture, rough-walled fractures. The source/sink term, $\mathcal{I}_c$, is

$$\mathcal{I}_c = \frac{\hat{Q} c_w}{AH}\delta(x - x_{inj/abs}, y - y_{inj/abs}) \tag{3.10}$$

where A [L^2] is the area of the discrete cell containing the well and δ is the Dirac delta function identifying the discrete cells that represent the injection and abstraction wells.

The above formulation and assumptions represent transport in the aquifer via two coupled 2D conservation laws (Eq.(3.4) and (3.5)). These PDEs are subject to the initial and boundary conditions:

$$\begin{gathered} c_w(x, y, 0) = c_s(x, y, 0) = 0, \\ c_w(0, y, t) = c_w(L_x, y, t) = c_s(0, y, t) = c_s(L_x, y, t) = 0, \\ c_w(x, 0, t) = c_w(x, L_y, t) = c_s(x, 0, t) = c_s(x, L_y, t) = 0, \end{gathered} \tag{3.11}$$

and the injection conditions:

$$\begin{aligned} c_w(x_{inj}, y_{inj}, 0 \leqslant t \leqslant t_{inj}) &= M_{inj}/(\hat{Q}t_{inj}), \\ c_w(x_{inj}, y_{inj}, t > t_{inj}) &= 0 \\ c_w(x_{abs}, y_{abs}, t) &= c_w(x_{abs}, y_{abs}, t) \end{aligned} \tag{3.12}$$

where M_{inj} [M] is the total mass of the solute injected above the background concentration and t_{inj} [T] is the duration of solute injection.

The width of the domain in both directions is taken to be $L_x = L_y = 450$ m. A boundary analysis indicated less than 0.04% relative difference between generated breakthrough curves from $L_x \geqslant 450$ m and $L_x = 1000$ m, suggesting that the elected domain captures the majority of transporting flow paths. The model is solved numerically by discretising in space using a standard finite-volume method and integrating in time using `MATLAB`'s built-in adaptive implicit solver for stiff ordinary differential equations, `ODE15s` (Shampine and Reichelt, 1997). A regular grid of $N_x = N_y = 101$ is selected, and the well locations indexed accordingly (see Appendix A for finite-volume methods). A convergence analysis indicated approximately 0.1% relative difference between the elected resolution (~ 4.5 m square cells) and a finer grid of 1 m squares cells.

The concentration within the fluid abstracted from BH2 is observed in time. The parameters are calibrated by minimising the mean absolute error $\langle \varepsilon^{abs} \rangle$ [ML^{-3}] between the observed and simulated abstracted concentrations,

$$\langle \varepsilon^{abs} \rangle = \frac{1}{N_t} \sum_{i=1}^{N_t} \mid c_{w,o}(t_i) - c_{w,s}(t_i) \mid, \tag{3.13}$$

where N_t [-] is the total number of data points for a time period, and $c_{w,s}(t_i)$ [ML^{-3}] and $\hat{c}_{w,o}(t_i)$ [ML^{-3}] are simulated and observed concentrations at the i^{th} time point, respectively. To do so, the model was nested within `MATLAB`'s bounded non-linear minimization function `FMINSEARCHBND`. This minimizing function is responsible for seeding parameter values (e.g., $\hat{Q}$, ϕ_e, α_L, α_T, D_s and t_{inj}) between prescribed upper and lower limits, which are then used to simulate a tracer test. The minimizing function continuously alters parameter values until a minimum $\langle \varepsilon^{abs} \rangle$ is achieved. The parameter set corresponding to the minimum $\langle \varepsilon^{abs} \rangle$ is reported as the best

fit. Bounded minimisation was chosen instead of unbounded minimisation to constrain the search to physically reasonable parameter values. If resulting best-fit parameter values were close to their prescribed upper or lower limits, the limits were extended to check that a smaller $\langle \varepsilon^{abs} \rangle$ did not lie outside the original range. The mean relative error $\langle \varepsilon^{rel} \rangle$ [%] between observed and simulated concentrations is also reported. It is calculated as:

$$\langle \varepsilon^{rel} \rangle = \frac{100}{N_t} \sum_{i=1}^{N_t} \frac{\mid c_{w,o}(t_i) - c_{w,s}(t_i) \mid}{c_{w,o}(t_i)}. \tag{3.14}$$

3.3 Calibration of Transport Parameters

With the constructed model, the fluorescein tracer test of RFH was simulated to re-characterise the apparent transport properties of the EC. Six parameters were calibrated with the bounded minimising algorithm: ϕ_e, α_L, α_T, $\hat{Q}$, D_s and t_{inj}. The nominal (documented) injection rate during the tracer test was 8.3 L/s. However, fluctuations in the associated drawdown data (Figures 5 and 6 in Clarkson et al. (2009)) suggest that the injection rate may have deviated during the test. As a result, the injection rate was treated as a calibration parameter. Two calibration efforts were conducted; one assuming $H = 5$ m, as in Clarkson et al. (2009), and on taken as $H = 68$ m to represent the full uncased height of the two wells.

The best-fit simulated breakthrough curves and the corresponding parameters, as well as those of Clarkson et al. (2009)), are shown in Figure 3.4 and Table 3.1, respectively. Clarkson et al. (2009) neglect dispersion and sorption ($\alpha_L = \alpha_T = D_s = 0$) and used the nominal values of $\hat{Q}$ and t_{inj}.

The present calibrations agree most strongly with the observations during the peak of the breakthrough curve, while under-predicting the late-time tail. A calibrated ϕ_e similar to that of Clarkson et al. (2009) was found for the model when assuming the same height ($H = 5$ m), which Clarkson et al. (2009) associated with a higher permeability zone within the EC. Best-fit dispersion coefficients are relatively consistent typical rule-of-thumb estimates of $\alpha_L = L_{BH}/10$ and $\alpha_T = L_{BH}/100$ (Arthur and Streetly, 2009; Gelhar, 1993). The calibration procedure is insensitive to

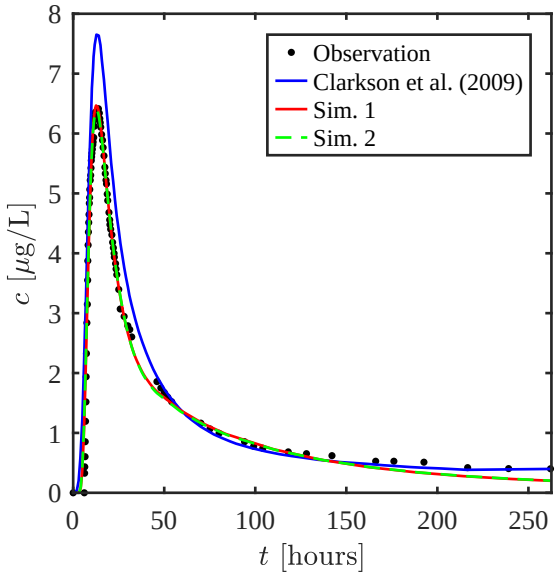

Figure 3.4: Comparison of simulated best-fit curve with output from `MODFLOW/MT3D` model (Clarkson et al., 2009) and the observed tracer breakthrough data. Simulations 1 and 2 correspond to $H = 5$ m and $H = 68$ m, respectively.

	Clarkson et al. (2009)	**Calibration 1**	**Calibration 2**	**Unit**
$\langle \varepsilon^{abs} \rangle$	0.91	0.18	0.17	[μg/L]
$\langle \varepsilon^{rel} \rangle$	21.04	7.80	7.70	[%]
H	5.00	5	68	[m]
ϕ_e	2.50E-03	4.46E-03	3.28E-04	[-]
α_L		$L_{BH}/18.6$	$L_{BH}/15.6$	[m]
α_T		$L_{BH}/192$	$L_{BH}/230$	[m]
$\hat{Q}$	8.3	10.5	10.5	[L/s]
D_s		4.35E-08	3.20E-09	[s^{-1}]
t_{inj}		0.92	0.77	[s]
$\phi_e H$	1.25E-02	2.2E-02	2.2E-02	[m]
D_s/ϕ_e		9.8E-06	9.8E-06	[s^{-1}]

Table 3.1: Comparison of best-fit parameters from Clarkson et al. (2009) and from the present analysis.

α_T for values less than $\alpha_L/10$, suggesting that transverse dispersion is unimportant. The calibrated value of $\hat{Q} = 10.5$ L/s is large but not improbably so.

Of the three parameters H, ϕ_e, and D_s, only two are strictly independent; that is, the model can be written in terms of the two groups $\phi_e H$ and D_s/ϕ_e. The values of these groups are reported in Table 3.1. For comparison with the results of Clark (1977), reported values of ϕ_e and D_s are calculated from the values of these groups and the assumed values of H.

Several other physical variables/mechanisms were investigated for their contribution to the breakthrough curve. These mechanisms/variables, such as transit time and dispersion within surface piping, total tracer mass, and the potential injection of abstracted solute, added complexity without commensurate improvement to the best-fit simulated breakthrough curve. In the case of variable total tracer mass, for example, the best-fit value was in agreement with the nominal reported mass of 15 g.

3.4 Identifiability of Solute Transport Characteristics

As in Chapter 2, the identifiability of each free parameter within the solute calibration procedure was investigated via progressive Monte-Carlo analysis. The progressive analysis incorporated six stages, accounting for the six free parameters (ϕ_e, α_L, α_T, $\hat{Q}$, D_s and t_{inj}). The associated procedure was as outlined in Section 2.4.4. The analysis adopted $H = 68$ m, representing the full height of the EC aquifer.

K-S scores are summarised in Table 3.2, while the prior and posterior distributions are illustrated in Figure 3.5. The effective porosity and the longitudinal dispersion coefficient appear to be strongly identifiable, followed by rock surface sorption, flow rate and the transverse dispersion coefficient, respectively. The results are insensitive to the solute injection time, which was assumed to be between 0.5 and 5 seconds.

These results should be viewed in light of the mechanisms behind the calibration process. The timing and frequency of solute concentration readings, combined

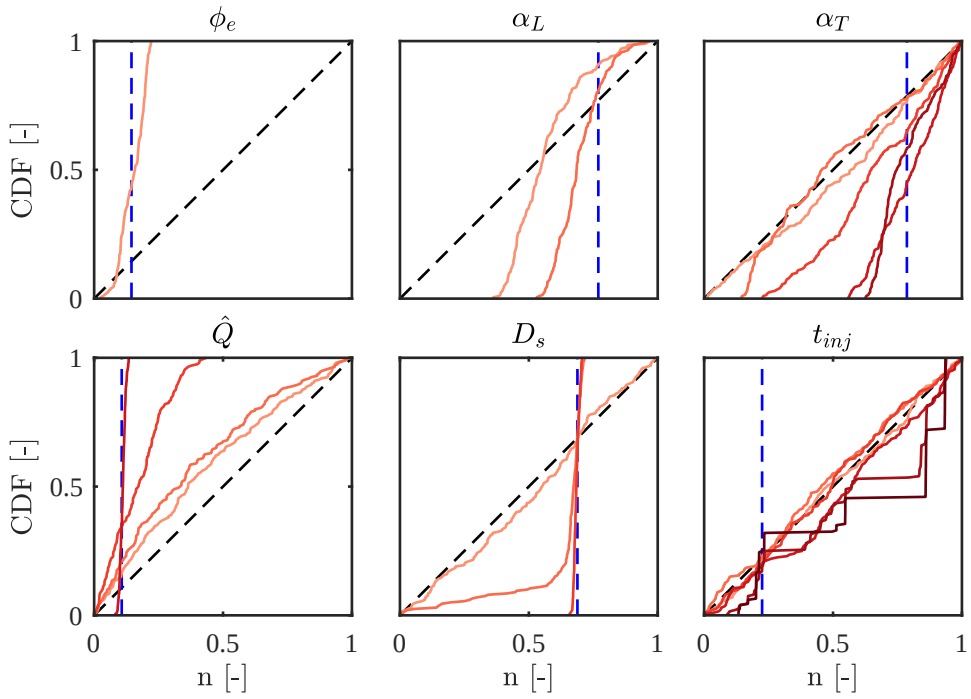

Figure 3.5: Posterior CDFs for progressive Monte-Carlo analyses, showing the progression of each individual parameter (red, light to dark) and respective best-fit parameters (blue) within normalised ranges, with prior uniform distribution hypothesis (black).

Stage	1	2	3	4	5	6
ϕ_e	***0.776***					
α_L	0.373	***0.537***				
α_T	0.090	0.144	0.279	0.557	***0.627***	
$\hat{Q}$	0.149	0.214	0.602	***0.866***		
D_s	0.070	0.458	***0.657***			
t_{inj}	0.045	0.065	0.055	0.134	0.294	***0.398***
$max(\langle\varepsilon^{abs}\rangle)$	0.906	0.624	0.411	0.182	0.179	0.179

Table 3.2: Summary of progressive Monte-Carlo K-S test for RFH Fluorescein Tracer Calibration, recording the maximum $\langle\varepsilon^{abs}\rangle$ observed within the top 1% of 20,000 results at each stage.

with the goal of minimising the mean absolute difference, result in an emphasis on matching the peak of the breakthrough curve. The late-time tail of the breakthrough curve comprises fewer observations of smaller magnitude. As a result, the analysis is most sensitive to the speed of the advective front (via the effective velocity q/ϕ_e) and the shape of said front (via α_L).

Rock surface sorption is often attributed with tailoring the late-time tail of the breakthrough curve. Transverse dispersion has a similar ability to aid the spread of solute into slower flow paths, thus delaying arrival time. We attribute the insensitivity of the calibration to transverse dispersion to either a lack of significant transverse characteristics in the applied model conditions (e.g., the continuum flow field smoothing-out flow paths) or the EC aquifer at RFH (e.g., a lack of transverse connection between physical flow paths). MacDonald and Allen (2001), Bloomfield (1996), Odling et al. (2013), and Younger and Elliot (1995) identify a primary fracture- or karstic-based flow regime within the EC. These regimes can feature flow paths disconnected from each other, whereby transverse dispersion characteristics would be less apparent. The continuum flow field is an approximation of these flow regimes, that neglects their distorted flow paths.

3.5 Discussion and Conclusion

A 2D solute transport model was constructed and used to simulate a well-doublet solute tracer test that was conducted at RFH in 2007. The simplified model used a curve-matching calibration procedure with six free variables, providing a best-fit solution between simulated and observed breakthrough curves at an observation well. Overall, the model provides a best-fit calibration with good agreement between the observed and simulated solute breakthrough curves. The accuracy of the fit is somewhat improved over the fit of Clarkson et al. (2009) (based on $\langle \varepsilon^{abs} \rangle$ and $\langle \varepsilon^{rel} \rangle$ values), particularly for the peak, and the suggested parameter values appear both reasonable and identifiable (except t_{inj}). The calibrated dispersion coefficients were consistent with typical 'rules of thumb' (Arthur and Streetly, 2009; Gelhar, 1993).

The agreement between the observed and simulated data appears to support the decision to neglect additional layers above the EC, but note that the inclusion of rock surface sorption is mathematically similar to the inclusion of additional layers. Additional layers would foreseeably provide additional flow paths within the area of influence, delaying arrival at the abstraction well and contributing to the tail of the breakthrough curve. A larger domain size would have the same effect.

Similarly, diffusion into and within the chalk matrix is potentially a non-negligible or alternative contributory mechanism. Auxiliary analysis of the expected rates of diffusion into matrix blocks of differing sizes was conducted in an effort to evaluate the potential role of matrix diffusion (see Appendix B). The associated rates of half-equilibrium for solute diffusion were observed to be on the order of years, and thus matrix diffusion was neglected. Rock surface sorption is regarded as suitable and representative of the discrete, tactile surfaces of a fracture network, contributing a storage component to transport between the wells.

The suggested best-fit parameters were investigated for their uniqueness and identifiability through a progressive Monte-Carlo analysis. For given values of H, the model identified unique values for the effective porosity, longitudinal and transverse dispersion, rock surface adsorption coefficient and CRT flow rate. The results were insensitive to the transverse dispersion coefficient as long as it was sufficiently small (one order of magnitude less than the longitudinal dispersion coefficient or smaller). Results were completely insensitive to the duration of solute injection (t_{inj}) within the range of values tested.

The simplicity of the model and relative ease with which it identified parameters is promising for further analyses and applications, such as the calibration and adoption of site-specific parameters in favour of literature-based values. Further geotechnical and hydrogeological analysis of the subsurface properties at RFH would be required to increase confidence in the purported transport mechanisms and best-fit parameters. This would most aptly include down-hole and cross-hole geophysical techniques, geotechnical logging and further tracer testing, aimed at investigating the apparent persistence of geological characteristics present at and

between the wells. Simulating the tracer test with the best-fit parameters using `MODFLOW/MT3D` could also yield further insights.

At the conclusion of this analysis, both hydraulic and solute transport models have identified parameters that differ from those initial adopted in design efforts at RFH. The re-calibrated parameters can be applied to thermal transport modelling at RFH to study whether observed operational behaviour can be reproduced. The identifiability analyses have highlighted the sensitivity of parameters and their associated mechanisms, greatly informing the proceeding thermal modelling efforts by indicating which parameters and mechanisms are likely to be key contributors to the thermal evolution of injected effluent water at RFH.

4

Thermal Transport Characterisation

Contents

4.1 Introduction

Historically, few open-loop GSHS have undertaken calibration of their apparent thermal transport properties, although such efforts have increased in recent years (see Boon et al., 2020; Law et al., 2007; Law and Mackay, 2010; Law, 2010; Park, Bae, and Lee, 2015; Busby, 2018). Calibrating the thermal transport properties of an installed system provides the ability to accurately model and manage the evolution of the system under operational conditions. In particular, it provides more accurate

means than the chemical tracer test for evaluating the time for injected thermal energy to migrate to the abstraction well ('thermal breakthrough'). This capacity could enable greater sustainability through increased power efficiency and design life while reducing associated risks (Birks, 2019; Younger, 2008). Unfortunately, no thermal tracer test, geophysical investigation, or core recovery were performed at RFH during its commissioning and design phases.

In the absence of thermal calibration, analytical and numerical approaches have been suggested for predicting thermal breakthrough times between coupled wells and the thermal evolution of injected effluent fluid (see Banks, 2009b; Banks, 2011b; Clyde and Madabhushi, 1983; Lippmann, 1980; Barker, 2010; Barker, 2012; La Bernardie et al., 2018; Milnes and Perrochet, 2013). Several studies have reviewed thermal migration and its impacts, geological considerations and resource mapping (Piga et al., 2017; Le Brun et al., 2011; Busby et al., 2009; Abesser et al., 2014). Other assessments have reviewed regional integration of thermal systems (Arthur and Streetly, 2009; Arthur et al., 2010; Clarkson et al., 2009) and lessons learned from existing systems (Fry, 2009; Birks, 2019; Birks et al., 2022; Younger, 2008; Abesser, 2010). But, as aptly pointed out by Arthur and Streetly (2009) and Arthur et al. (2010), it is the revisiting of previous operational behaviour that will ultimately enable further understanding and verification of proposed solutions, models and assumptions.

For RFH, several years of operational data are available through publications and reports (Birks, 2019; Clarkson et al., 2009). The intention of this chapter is to utilise the available data, in combination with modelling, to evaluate the apparent thermal evolution of RFH over several years of operation. The hydraulic and solute transport characterisations from Chapter 2 and 3, respectively, will be used to inform parameter values. Thermal parameter calibration and the simulation of historical operational data will be used to provide insight into the thermal evolution of the system.

4.1.1 Thermal Evolution of Royal Festival Hall

During commissioning, thermal modelling of RFH was conducted by Clarkson et al. (2009) following calibration using the solute tracer test (see Chapter 3) and assuming hydraulic properties from Gale, Williams, and Mansour (2006) and Ellison et al. (2004)(see Chapter 2). The thermal modelling indicated minimal movement of the resultant thermal plume from injected warmed effluent water, concluding that detectable temperature changes at the abstraction well ('thermal breakthrough') were not expected to occur until after 2 years of operation with re-injection.

Since commissioning in 2006, the open-loop GSHS at RFH has been operating in various capacities and configurations. Figure 4.1 provides a summary of flowmeter and temperature data from published site records and reports for the period June 2006 to January 2012. Key features of this operational history include:

- Prior to June 2007, the GSHS operated by abstracting fluid from the EC aquifer via BH1 and then discharging effluent to the River Thames. No effluent fluid was injected into the EC during this period. BH2 was not operational.

- During June and July 2007, pump tests and tracer tests were conducted using BH1 and BH2. As shown in the Figure 4.1, flowmeter data show equal and opposite flowrates while temperature data show 'baseline' temperatures in BH1 during abstraction and elevated readings in BH2 due to re-injection of warmed effluent fluid.

- From July 2007 to January 2009, the GSHS operated by abstracting fluid from the EC via BH1 and discharging effluent to the River Thames. Baseline temperatures were observed in BH2, confirming that no re-injection occurred during this period.

- From January to May 2009, the GSHS operated by abstracting fluid from the EC via both BH1 and BH2 and discharging effluent to the River Thames. No re-injection occurred during this period. Temperature data for BH2 shows that abstracted fluid from the EC was at baseline temperatures.

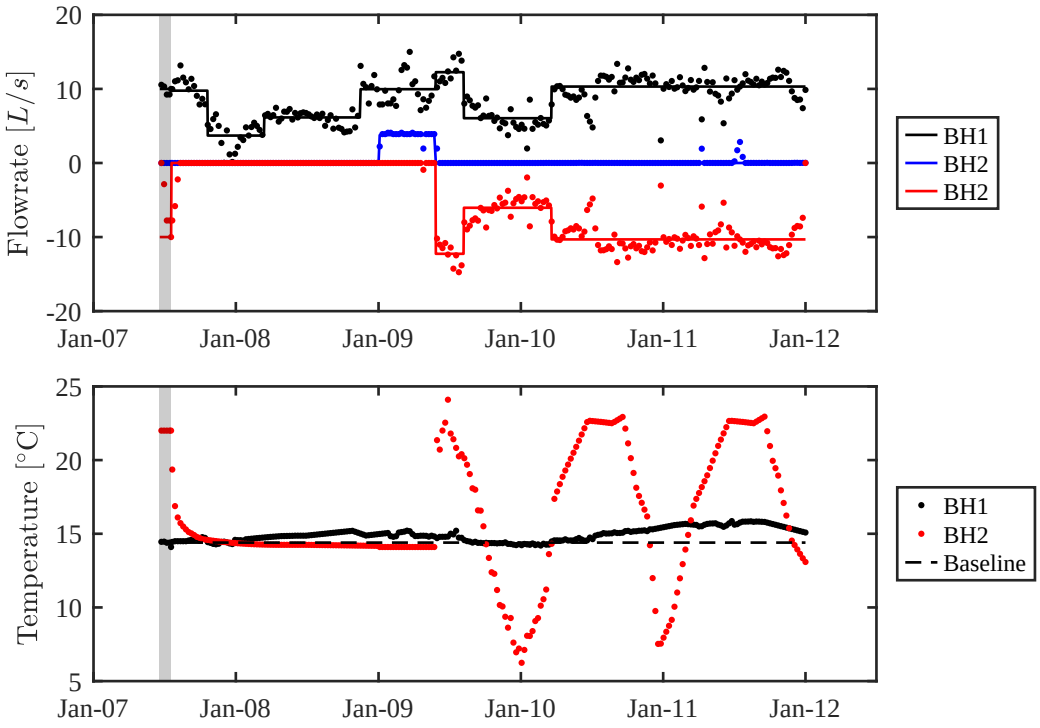

Figure 4.1: Summary of recorded flowmeter and temperature data for both wells at RFH (BH1 and BH2) for a period of 4.5 years following the start of the 2007 re-injection tests. The top panel shows average weekly flow rates (dots), which are further averaged to constant flow rates over several distinct operational periods (lines). Positive and negative flow rates indicate abstraction and injection, respectively.BH1 is used exclusively for abstraction (black), whereas BH2 has periods where abstraction and injection are recorded (blue and red, respectively). The bottom panel shows average weekly fluid temperatures, along with the 2006–2007 baseline abstracted fluid temperature. The June–July 2007 test period is indicated with a grey band. Data produced through a combination of published site records and reports (Clarkson et al., 2009; Birks, 2019).

- From May 2009 onward, GSHS began operating in a well-doublet configuration, abstracting at BH1 and injecting effluent at BH2 semi-continuously for both cooling and heating (i.e., operating in both winter and summer).

Two unexpected thermal events are visible in the temperature data from BH1. Firstly, starting in January 2008 and peaking around January 2009, temperatures gradually increased to a few degrees above baseline. By January 2010, temperatures at BH1 returned to baseline. Secondly, starting in June 2010 and peaking around August 2011, temperatures again gradually drifted well above baseline before trending back toward baseline in late 2011. These thermal events were noted

by Birks (2019), who also speculated an additional, shorter period of elevated temperature around September 2007. We consider the additional event's deviation from the background temperature to lie within sensor tolerances and do not investigate it further.

These elevated thermal readings may indicate disagreement with the initial modelling assertions. Following the 2007 trial period, the first thermal event developed about 6 months after initial injection (January 2008) and peaked about 12 months later (January 2009). Likewise, following an injection period in the summer of 2009, the second event developed 6–8 months afterwards (January to March 2010) and peaked 12–18 months later (January to July 2011). If these thermal readings were caused by the migration of injected effluent, then they represent thermal breakthrough approximately 4 times faster than initially predicted.

The GSHS heat exchangers were operational during the 2007 pump and tracer tests (see Chapters 2 and 3), meaning that the water injected via BH2 was warmed effluent fluid. The management systems and installed testing infrastructure monitored the temperature of the injected and abstracted fluid prior to, during and after the pump and tracer tests (Figures 10 to 15 of Clarkson et al., 2009). Clarkson et al. (2009) provides a summary of the installed infrastructure, noting that temperature sensors are installed at 90 m below ground level in each well, within an installed bypass unit, and within the discharge line following the heat exchangers.

Figure 4.2 shows the temperature history at the abstraction well (BH1) and injection well (BH2), during and after the June–July 2007 testing period. The injected fluid temperature varied, with daily minimum and maximum temperatures coinciding with midnight and midday demands, respectively. For unknown reasons, temperature data for the fluid injected at BH2 is missing from records from approximately days 19 to 29 of testing. Following day 29 (the end of the pumping test), BH2 data resumes with a thermal decay from an elevated temperature back to baseline over the next ∼70 days. By assuming an average injection temperature of 22 °C and an average flow rate of 8.3 L/s Clarkson et al. (2009) estimated that a total of 194.1 MWh of energy was injected into the aquifer during the testing period.

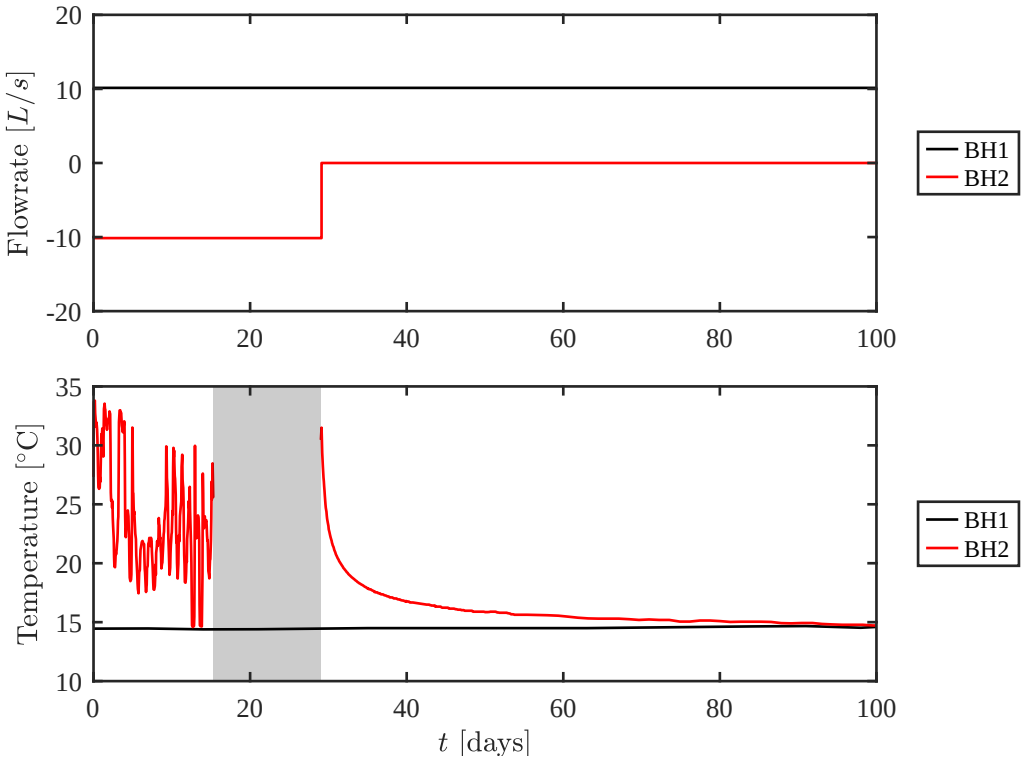

Figure 4.2: Injection (BH2, red) and abstraction (BH1, black) flow rates and recorded temperatures during and after the month-long pumping test (20 June to 19 July). Temperature data is missing between approximately day 19 and day 29 of testing (grey band).

In the present study, this thermal decay period is isolated and used for thermal calibration. Following calibration, the best-fit thermal transport parameters will be adopted in an attempt to simulate the observed operational history of RFH and provide insight into the observed thermal events.

4.2 Modelling and Calibration Approach

4.2.1 Governing Equations

To investigate the thermal events at RFH by performing a thermal calibration, the 2D solute transport model from Chapter 3 is adapted for thermal transport. The model domain, illustrated in Figure 3.2, remains a representation of the horizontal plane of the EC aquifer and features the two wells within its domain. The thermal model is constructed to allow for the horizontal domain to be divided into two

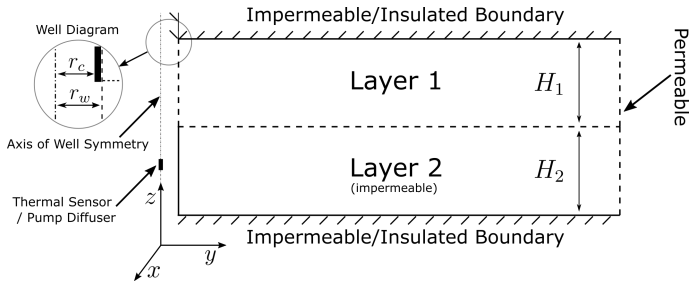

Figure 4.3: Illustration of two-layer domain, showing permeable/impermeable and insulated boundary conditions in the y-z plane. The location of the thermal sensor and pump diffuser are shown in the well in the lower layer. Injected fluid travels up to the permeable upper layer.

horizontal layers. Figure 4.3 shows a cross-section of the aquifer, illustrating the impermeable/permeable and insulating conditions applied to the thermal model.

The following assumptions and conditions are applied:

- The aquifer layers are continuous, homogeneous, isotropic and of uniform thickness.
- The aquifer is confined by impermeable and perfectly insulated strata.
- The aquifer consists of fractured chalk, which can be modelled as a dual-porosity continuum. The two continua represent the fractures and the chalk matrix, the latter comprising rock and 'dormant' pore water.
- Thermal transport in the fractures occurs via advection, dispersion and conduction. Transport in the matrix occurs only via conduction.
- The upper layer consists of fractures and matrix. The lower layer is matrix only.
- Simplified steady-state flow fields: The doublet flow field is derived as outlined in Chapter 3.2.1.
- Transport between layers is via matrix conduction. Non-dispersive vertical flow is only permitted in the grid locations of the wells.

- The fluid viscosity and density are constant and uniform. Note, however, that the operational temperature ranges are expected to result in a 30–40% variation in fluid viscosity and a $\sim 0.2\%$ variation in fluid density.
- The temperatures within the layers are vertically uniform.
- The layer heights conserve the total height of the EC ($H_{EC} = H_1 + H_2$). Where a single layer model is used, $H_{EC} = H_1$ (in which case the sensor will be located in the 'upper' layer).

Each layer is governed by two continuity equations for thermal energy transported through a saturated porous medium, allowing the fractures and the matrix to be at different temperatures (local thermal non-equilibrium, or LTNE)(see Nield, Bejan, et al., 2006):

$$\phi_e \frac{\partial e_w}{\partial t} + \boldsymbol{\nabla} \cdot (\mathbf{q}_w e_w - \phi_e \mathbf{D}_w \cdot \boldsymbol{\nabla} e_w) - \mathcal{I}_w - \frac{\Gamma}{C_w \rho_w}(e_m - e_w) = 0, \tag{4.1}$$

and,

$$(1 - \phi_e)\frac{\partial e_m}{\partial t} - (1 - \phi_e) D_m \cdot \boldsymbol{\nabla}^2 e_m + \frac{\Gamma}{C_m \rho_m}(e_m - e_w) = 0, \tag{4.2}$$

where subscripts w and m denote the fracture water and porous matrix, respectively, ϕ_e [-] is the effective porosity of the fracture network, e [Θ] is temperature, t [T] is time, $\mathbf{q}_w$ [LT^{-1}] is the steady-state fluid flux, $\mathcal{I}_w$ [T^{-1}] is the source/sink due to injection/abstraction, C [$\mathrm{L}^2\Theta^{-1}\mathrm{T}^{-2}$] is the specific heat capacity, ρ [ML^{-3}] is the density, Γ [$\mathrm{ML}^{-1}\mathrm{T}^{-3}\Theta^{-1}$] is the thermal transfer coefficient for exchange between fracture and matrix, and $\mathbf{D}_w$ [$\mathrm{L}^2\mathrm{T}^{-1}$] is the conduction/dispersion tensor,

$$\mathbf{D}_w = \begin{bmatrix} D_{xx} & D_{xy} \\ D_{yx} & D_{yy} \end{bmatrix}, \tag{4.3}$$

where

$$D_{xx} = D_w + \frac{1}{\phi_e |\mathbf{q}_w|}(\alpha_L q_{w,x}^2 + \alpha_T q_{w,y}^2), \tag{4.4}$$

$$D_{yy} = D_w + \frac{1}{\phi_e |\mathbf{q}_w|}(\alpha_T q_{w,x}^2 + \alpha_L q_{w,y}^2), \tag{4.5}$$

$$D_{xy} = D_{yx} = (\alpha_L - \alpha_T)\frac{|q_{w,x} q_{w,y}|}{\phi_e |\mathbf{q}_w|}. \tag{4.6}$$

In the above equations, D_w [L^2T^{-1}] and D_m [L^2T^{-1}] are the thermal diffusivity of the fracture water and porous matrix, respectively, and α_L [L] and α_T [L] are the longitudinal and transverse dispersion coefficients, respectively. The thermal diffusivities are

$$D_w = \frac{\lambda_w}{C_w \rho_w} \quad \text{and} \quad D_m = \frac{\lambda_m}{C_m \rho_m}, \tag{4.7}$$

where λ [$MLT^{-3}\Theta^{-1}$] is the thermal conductivity. The material properties of the matrix are taken to be the volume-weighted mean of the solid matrix and dormant pore fluid:

$$\begin{aligned} \phi &= \phi_e + \phi_m, \\ \lambda_m &= \phi_m \lambda_w + (1 - \phi_m)\lambda_s, \\ \rho_m C_m &= \phi_m \rho_w C_w + (1 - \phi_m)\rho_s C_s, \text{ and} \\ \rho_m &= \phi_m \rho_w + (1 - \phi_m)\rho_s. \end{aligned} \tag{4.8}$$

where the subscript s denotes the solid mineral and ϕ_m is the porosity of the matrix. The source/sink term, $\mathcal{I}_w$, is defined as:

$$\mathcal{I}_w = \frac{\hat{Q} e_w}{AH} \delta(x - x_{inj/abs}, y - y_{inj/abs}) \tag{4.9}$$

where, $\hat{Q}$ [L^3T^{-1}] is the imposed pumping rate, A [L^2] is the area of the discrete cell containing the well, H [L] is the height of the aquifer, and δ is the Dirac delta function identifying the discrete cells that represent the injection and abstraction wells.

4.2.2 Calibration Efforts

Initial thermal-calibration efforts focus on the thermal decay observed in BH2 during the ~70 days following the CRT in 2007, as discussed above (Figure 4.2). To focus on BH2, the domain is shifted so that BH2 is located in the center. BH1 remains within the domain and is located a distance L_{BH} from BH2. Due to the missing thermal data during a portion of the CRT, it is not possible to replicate the exact thermal injection history; instead, the history will be constrained by the estimated cumulative energy injected during the test. The simulation features

two stages: one stage to simulate the injection of thermal energy under doublet-flow conditions and a second stage to simulate the decay period, during which only BH1 was active (abstracting).

For the first stage, the following initial and boundary conditions are adopted:

$$\begin{aligned} e_w(x,y,n,0) = e_m(x,y,n,0) = e_0, \\ e_w(0,y,n,t) = e_w(L_x,y,n,t) = e_m(0,y,n,t) = e_m(L_x,y,n,t) = e_0, \\ e_w(x,0,n,t) = e_w(x,L_y,n,t) = e_m(x,0,n,t) = e_m(x,L_y,n,t) = e_0, \\ Q_{BH2} = -Q_{BH1} = \hat{Q}_1, \end{aligned} \tag{4.10}$$

where e_0 [Θ] is the baseline temperature of the aquifer and $\hat{Q}_1$ [$\mathrm{L}^3\mathrm{T}^{-1}$] is the design flowrate for the first stage of simulation. The simulation is terminated once the cumulative injected thermal energy is equal to 194.1 MWh, as estimated by Clarkson et al. (2009). The cumulative energy of each layer is calculated as

$$E_{total} = \int_0^{L_y} \int_0^{L_x} \phi_e \rho_w C_w H(e_w - e_0) + (1-\phi_e)\rho_m C_m H(e_m - e_0)\,\mathrm{d}x\,\mathrm{d}y. \tag{4.11}$$

Where a two layer model is used the cumulative energy of each layer is summed to evaluate the total energy within the domain.

The second stage of simulation is seeded by the result of the first. The following initial and boundary conditions are adopted:

$$\begin{aligned} e_w(x,y,n,0) = e_{w,1}(x,y,n) \quad \text{and} \quad e_m(x,y,n,0) = e_{m,1}(x,y,n), \\ e_w(0,y,n,t) = e_w(L_x,y,n,t) = e_m(0,y,n,t) = e_m(L_x,y,n,t) = e_0, \\ e_w(x,0,n,t) = e_w(x,L_y,n,t) = e_m(x,0,n,t) = e_m(x,L_y,n,t) = e_0, \\ Q_{BH2} = 0 \quad \text{and} \quad -Q_{BH1} = \hat{Q}_2 \end{aligned} \tag{4.12}$$

where $e_{w,1}$ and $e_{m,1}$ [Θ] are the resultant temperature distributions from the first stage and $\hat{Q}_2$ [$\mathrm{L}^3\mathrm{T}^{-1}$] is the design flowrate for the second stage.

As in previous chapters, this problem is solved numerically by discretising in space using a standard finite-volume method and integrating in time using `MATLAB`'s built-in adaptive implicit solver for stiff ordinary differential equations, `ODE15s` (Shampine and Reichelt, 1997). An event function is incorporated into the solver to terminate the first stage at the prescribed energy storage condition. The domain is

discretised into 101×101 rectangular grid blocks, logarithmically increasing in size with distance from BH2. The grid block containing BH2 is of size $\mathrm{d}x = \mathrm{d}y = 2r_w$.

To calibrate a best-fit curve between the observed and simulated temperature of BH2, the model was nested within `MATLAB` 's bounded non-linear minimization function `FMINSEARCHBND`. The bounded minimizing function is responsible for seeding parameter values between prescribed upper and lower limits, which are then used to simulate the injection and then decay of thermal energy in BH2. As per the previous analysis, the accuracy of each simulation and associated parameter set is assessed by calculating the mean absolute error $\langle \varepsilon^{abs} \rangle$ [Θ] between observation and simulation temperatures:

$$\langle \varepsilon^{abs} \rangle = \frac{1}{N_t} \sum_{i=1}^{N_t} \mid e_{w,o}(t_i) - e_{w,s}(t_i) \mid, \tag{4.13}$$

where N_t [-] is the total number of data points for a time period, and $e_{w,s}(t_i)$ [Θ] and $e_{w,o}(t_i)$ [Θ] are simulated and observed temperatures at BH2 at the i^{th} time point, respectively. The mean relative error $\langle \varepsilon^{rel} \rangle$ [%] is calculated as:

$$\langle \varepsilon^{rel} \rangle = \frac{100}{N_t} \sum_{i=1}^{N_t} \frac{\mid e_{w,o}(t_i) - e_{w,s}(t_i) \mid}{e_{w,o}(t_i)}. \tag{4.14}$$

The fluid temperature in BH1 is monitored to confirm that the suggested best-fit parameters do not result in thermal breakthrough, which was not observed during the testing period.

The constructed model has the ability to calibrate several parameters, while others are fixed/prescribed; Γ is calibrated to capture the degree of LTNE between fracture and matrix temperatures, the constant temperature of injected fluid is altered to account for the temperature fluctuations that may be present in the period of missing data, α_L and α_T are calibrated to account for a difference between solute and thermal dispersion properties (Bandai et al., 2017), H_1 is varied from H_{EC} to investigate the role of a second layer, and $\hat{Q}$ is varied to account for low confidence in reported flow rates. The duration of the injection period prior to decay is determined by the average pumping rate, injection temperature and reported total energy injected (194.1 MWh).

4.3 Thermal Calibration

Efforts to calibrate the thermal properties of RFH by simulating the thermal decay illustrated in Figure 4.2 took three main approaches: a calibration varying conduction characteristics, a calibration varying dispersion characteristics and a calibration splitting the EC into two layers. It was found that conductive and dispersive characteristics could not be identified independently given the available data, and thus one of these sets of characteristics had to be assumed. Several studies have discussed the identifiability of dispersion and diffusion/conduction, their relationship, and their contributions to solute and thermal transport (e.g., Mathias et al., 2009; Rau, Andersen, and Acworth, 2012; Park, Bae, and Lee, 2015; Tang and Zee, 2021; Bandai et al., 2017; Zhou, Oldenburg, and Rutqvist, 2019). Mathias et al. (2009) highlight that greater time-scales of tracer tests and the use of multiple tracers of differing characteristics would provide necessary additional constraints to aid independent identification of dispersive/diffusive properties within a fractured porous media. Park, Bae, and Lee (2015) evaluate the specific contribution and importance of thermal dispersivity in a context of GSHS design and operation.

The calibration efforts allowed for LTNE due to the physical properties of the EC. It is widely agreed that the fracture network provides the primary permeability of the EC (Allen et al., 1997; Price, Downing, and Edmunds, 1993; Barker, 1993; Bloomfield, 1996). The relatively low effective porosity established in Chapter 2 strongly supports this idea. For matrix blocks of size 3 to 30 m, the time to thermal half-equilibrium is expected to be days to years (see Appendix B). We therefore allow for LTNE, hypothesizing that the thermal front within the fracture network is likely to advance ahead of the front in the rock matrix.

To assess the effect of assuming LTNE within the simulation domain, simulation was conducted with varying values of Γ. The simulation focused on the final temperature difference between the water and the rock after 10 days of constant rate injection using the domain settings as described in Section 4.2.2 and $H_1 = H_{EC}$. The results are presented in Figure 4.4 and show that, for $\Gamma > 100$, the $\langle \varepsilon^{abs} \rangle$

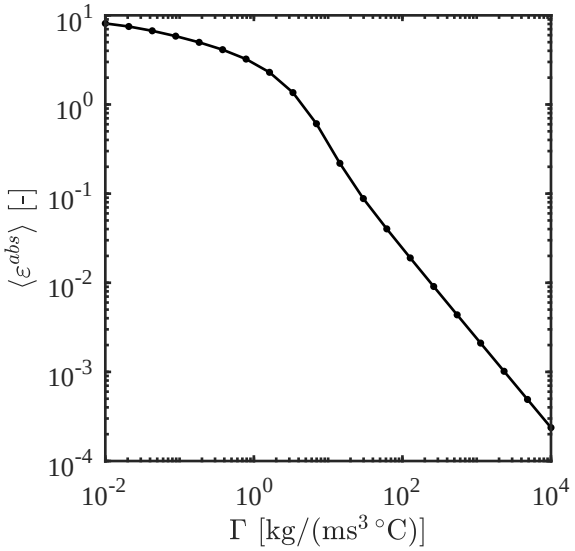

Figure 4.4: Effect of LTNE on the mean absolute difference ($\langle \varepsilon^{abs} \rangle$) between fracture fluid and matrix temperatures. Plot shows $\langle \varepsilon^{abs} \rangle$ within a 250 m square domain at the conclusion of 10 days of injection at a rate of 10 L/s and at a temperature of 10 °C above baseline.

between the two continua decreases below approximately 0.01 °C. The analysis identified that $\Gamma \geqslant 1E-2$ was a suitable range for investigations adopting LTNE.

The three calibration approaches simulate the pre-decay period dependent on their core assumptions. The first two calibrations assume a single-layer domain ($H_1 = H_{EC}$) with varying degrees of thermal dispersion and conduction. Thermal energy is injected into the domain by

$$e_w(\frac{L_x}{2}, \frac{L_y}{2}, 1, t) = e_{w,inj}, \tag{4.15}$$

where $e_{w,inj}$ [Θ] is the constant temperature condition at BH2. The third calibration assumes a two-layer domain and thus applies this temperature condition to the second layer which houses the thermal sensor

$$e_w(\frac{L_x}{2}, \frac{L_y}{2}, 2, t) = e_{w,inj}. \tag{4.16}$$

4.3.1 Calibration 1: Strong Conduction

In the first calibration effort, the well radius (r_w), aquifer height (H), porosities (ϕ_e and ϕ_m), density (ρ_w and ρ_m), longitudinal dispersion (α_L), transverse dispersion

Parameter	Value	Unit
ρ_w	1000	[kg/m^3]
ρ_s	1800	[kg/m^3]
λ_w	0.6	[W/(m.C)]
λ_s	1.67	[W/(m.C)]
C_w	4179	[J/(kg.C)
C_s	800	[J/(kg.C)
ϕ_m	0.3	[-]
$\phi_e H_{EC}$ [m]	2.20E-02	[m]
H_{EC}	68	[m]
α_L	$L_{BH}/15.6$	[m]
α_T	$L_{BH}/230$	[m]
L_{BH}	150	[m]
Q_1	8.3	[L/s]
Q_2	8.3	[L/s]

Table 4.1: Summary of parameters adopted in thermal modelling efforts

(α_T), thermal conductivity (λ_w and λ_m), specific heat capacity (C_w and C_m), and average pumping rates (Q_1 and Q_2) were fixed. A summary of parameters is provided in Table 4.1. The conductive exchange (Γ), matrix thermal diffusivity (D_m) and injection temperature ($e_{w,inj}$) were then calibrated to achieve a best-fit thermal decay curve.

Results of this analysis are summarised in Table 4.2, including the elected upper- and lower-bound values for the bounded minimising function. The simulated decay is shown in Figure 4.5(a). The results of the calibration show agreement between the observed and simulated thermal-decay curves at BH2, and no response at BH1 in agreement with the observation that thermal breakthrough was not detected. The best-fit value of Γ suggests that the calibration effort does not benefit from LTNE, and rather is trending toward local thermal equilibrium (LTE). The analysis allowed the matrix thermal diffusivity to vary between 1 and 1000 times its nominal value, with the best-fit value being $207.56\tilde{D}_m$. These results suggest substantially more thermal conduction within the rock matrix than initially expected. The nominal matrix conduction value is insufficient to spread the injected thermal plume and LTNE hinders rather than helps this decay. A conduction value greater than 200 times its nominal value is unlikely to be physically correct.

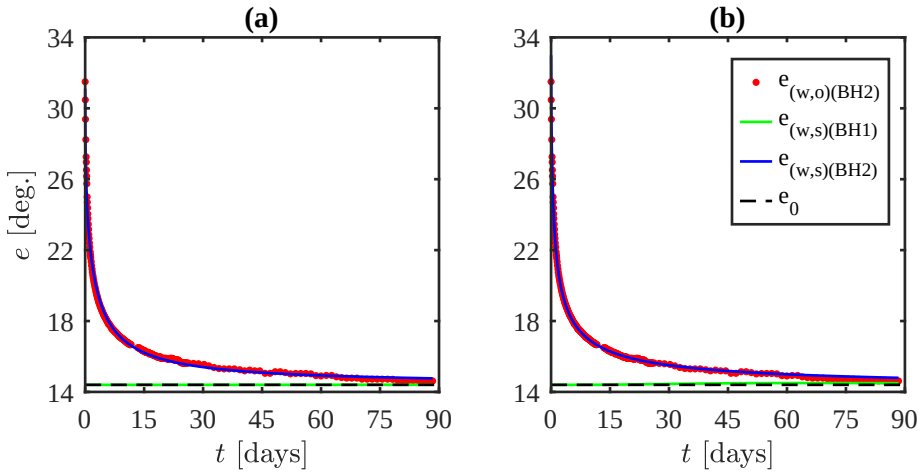

Figure 4.5: Results of (a) strong conduction and (b) strong dispersion calibrations. Panels show the simulated and observed thermal decay curves.

Calibration	Parameter	Suggested Best-fit	Lower Bound	Upper Bound	Unit
1	Γ	9.30E+05	1E-2	1E+6	[kg/(ms^3 °C)]
	T_{max}	31.1	30.0	50.0	[°C]
	D_m	207.56 $\tilde{D}_m$	$\tilde{D}_m$	1000 $\tilde{D}_m$	[m^2/s]
	$\langle \varepsilon^{abs} \rangle$	0.144			[°C]
	$\langle \varepsilon^{rel} \rangle$	0.75			[%]
2	Γ	9.99E+05	1E-2	1E+6	[kg/(ms^3 °C)]
	α_L	$L_{BH}/0.054$	$L_{BH}/0.01$	$L_{BH}/100$	[m]
	α_T	$L_{BH}/2.79$	$L_{BH}/(0.1\alpha_L)$	$L_{BH}/(100\alpha_L)$	[m]
	$e_{w,inj}$	33.01	30.0	50.0	[°C]
	$\langle \varepsilon^{abs} \rangle$	0.041			[°C]
	$\langle \varepsilon^{rel} \rangle$	0.22			[%]
3	Γ	9.93E+05	1E-2	1E+6	[kg/(ms^3 °C)]
	H_1	50.1	1	67	[m]
	H_2	17.90			[m]
	D_m	3.3471$\tilde{D}_m$	$\tilde{D}_m$	1000 $\tilde{D}_m$	[m^2/s]
	$\langle \varepsilon^{abs} \rangle$	0.0983			[°C]
	$\langle \varepsilon^{rel} \rangle$	0.56			[%]

Table 4.2: Summary of best-fit parameters, lower and upper bound for the three calibration efforts: allowing strong thermal conduction, strong thermal dispersion and two layers. The nominal matrix conduction is taken to be $\tilde{D}_m = 4.8E-7$ m^2/s.

4.3.2 Calibration 2: Strong Dispersion

In the second calibration, the thermal diffusivity (D_m) was fixed and the dispersivities (α_L and α_T) were calibrated; other parameters were treated the same as in Section 4.3.1. The results are summarised in Table 4.2, including the upper- and lower-bound values for the bounded minimising function. The simulated decay curve is shown in Figure 4.5(b). Similar to calibration 1, the results show good agreement between observed and simulated thermal decay curves, with marginally smaller errors for calibration 2. The simulation again avoids thermal breakthrough at BH1 and the best-fit values of Γ again indicate that LTE is preferred. The longitudinal and transverse dispersivities were allowed to vary above or below the values calibrated through the solute tracer test. The best-fit value of longitudinal and transverse dispersivities are 273 and 113 times larger, respectively, than the values suggested by the tracer calibration, in both cases indicating substantially more dispersion than initially expected.

With a fixed matrix conduction (D_m) value, the second calibration adopts significantly larger dispersivities to spread the injected thermal plume. Specifically, the calibration requires the larger values to increase dispersion at BH2 in response to ongoing abstraction at BH1. The similar magnitude of parameter adjustment in calibration 1 and 2 (i.e., more than 200 times nominal value) suggests the need for a substantially enhanced Fickian spreading, whether diffusive or dispersive.

4.3.3 Calibration 3: Two-layer scenario

The results of the prior calibrations, as outlined in Section 4.3.1 and 4.3.2, indicate stronger-than-expected thermal conduction or dispersion characteristics. Both would imply characteristics outside of typically adopted and reported ranges (Gelhar, 1993; Clarkson et al., 2009; Arthur and Streetly, 2009; Arthur et al., 2010; Bandai et al., 2017; Tang and Zee, 2021; Park, Bae, and Lee, 2015; Rau, Andersen, and Acworth, 2012; Mathias et al., 2009).

It was initially assumed that flow within the aquifer was uniform throughout its height and that the previously adopted dual-porosity approach was appropriate.

However, several studies report a higher permeability zone within the upper 5–10 m of the EC and much lower permeability with depth (Allen et al., 1997; Bloomfield, 1996; Ellison et al., 2004). The thermal sensors and pump-diffuser ensembles of both wells are reported to have been installed at 90 m below ground level, which would place them below the high-permeability zone of the EC. It is therefore envisaged that the sensors may be located in a section of the well that lacks horizontal flow, and where fluid instead flows vertically up or down within the well until it reaches a permeable zone. If true, this situation suggests that the sensors would respond rapidly during injection or abstraction but more slowly during quiescent periods. In the absence of flow, the thermal evolution of the fluid surrounding the sensor would be due predominantly to conduction through the water in the well. The surrounding aquifer matrix would remain close to the background temperature due to a lack of permeation, and would therefore communicate with the well via conduction during the entire period.

To explore this hypothesis, a third calibration was conducted using a two-layer model to represent two horizontal layers within the aquifer: the upper, high-permeability zone and a lower, negligible-permeability zone, both of unknown height (see Figure 4.3). The upper layer is modelled as described above; the lower layer is taken to be impermeable (conduction only). The governing equations are the same as in Section 4.2, as are the assumptions. Specific attention is drawn to points of difference with the previous calibrations:

- The total height of the aquifer (H_{EC}) is divided amongst the layers: $H_2 = H_{EC} - H_1$ (where $H_{EC} = 68$ m and $H_1 \leqslant 67$ m).

- The steady-state flow field is applied to the upper layer. No flow is permitted within the lower layer, with the exception of the numerical cell that corresponds to the well.

- The lower layer is assumed to comprise entirely aquifer matrix, again with the exception of the well.

- The thermal source (Eq.(4.9)) is applied to the well in the lower layer.
- Thermal exchange between the layers is through matrix conduction, again with the exception of the well.

In the third calibration effort, the well radius (r_w), aquifer height (H), porosities (ϕ_e and ϕ_m), densities (ρ_w and ρ_m), thermal conductivities (λ_w and λ_m), specific heat capacities (C_w and C_m), and average pumping rates (Q_1 and Q_2) were fixed and the conductive exchange (Γ), the thickness of the upper layer (H_1), and the matrix diffusivity (D_m) were calibrated to achieve a best-fit thermal decay curve. The duration of the injection period was determined as above.

A summary of the best-fit parameters is provided in Table 4.2. The simulated and observed thermal decay curves and the thermal footprints in both layers at the end of injection (start of decay) are illustrated in Figure 4.6. As per the previous two calibrations, calibration 3 achieves good agreement between the simulated and observed thermal decay curves. The decay curves of all three calibrations are relatively indistinguishable. The calibrated value of Γ is again representative of LTE. The calibrated H_1 is approximately 50 m. This is larger than the suggested 5–10 m high-permeability zone, but it is ultimately a single effective value representing a geologically complex layer. The calibrated matrix thermal conduction (D_m) is about 3.35 times larger than the nominal value, significantly closer than the strong-thermal-conduction value above.

4.3.4 Parameter Identifiability and Sensitivity

The identifiability of each calibrated parameter in the first two calibration efforts was investigated. The third was not investigated as its conceptualisation was based on the physical problem being poorly constrained. As in previous chapters, a progressive Monte-Carlo analysis was conducted. The analysis incorporated one stage per free parameter, as described in Chapter 2.4.4. Again, each stage comprised 20,000 simulations with uniform prior distributions for each parameter within the bounds specified in Table 4.2.

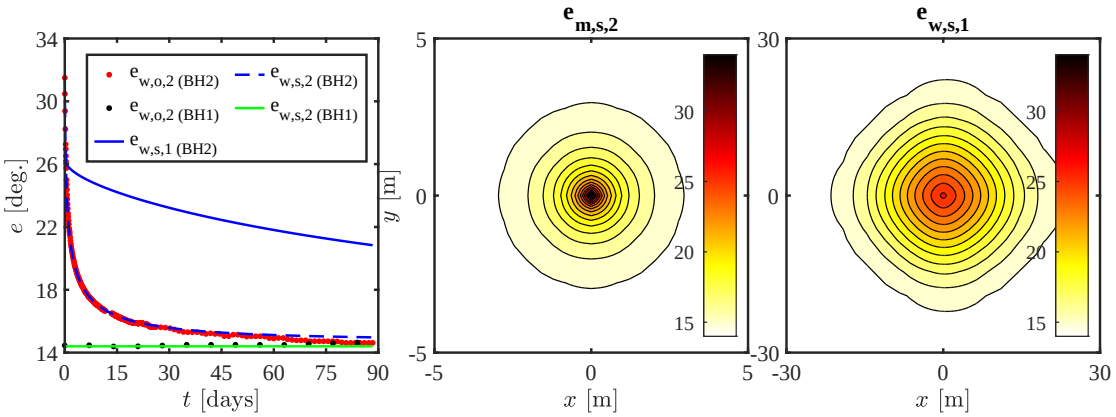

Figure 4.6: Two-layer calibration. Left panel shows the simulated and observed thermal decay in BH2, against baseline and BH1 simulated temperatures. Middle and right panel show temperature distribution in the lower and upper layers, respectively, at the end of injection.

Figure 4.7 shows the posterior CDFs of the various states for both calibration approaches, having normalised the parameter values by their upper- and lower-bounds. The corresponding K-S scores are summarised in Table 4.3. Calibration 1 (strong thermal conduction) shows a strong sensitivity to D_m. Both calibrations produce a decay curve that initiates at the first observed data point, indicating a sensitivity to $e_{w,inj}$ venturing away from its lower bound. As noted above, both calibrations show a strong preference for $\Gamma \geqslant 100$, which corresponds to LTE (Figure 4.4). Calibration 2 (strong dispersion) shows a primary sensitivity to α_L, followed by α_T. Across the two calibration methods, D_m, α_L and α_T are responsible for the greatest error reduction between simulated and observed decay curves.

4.4 Simulation of operational data

Following the calibration efforts of Sections 4.3.1 to 4.3.3, the three sets of calibrated parameters are used to simulate the operational data shown in Figure 4.1. The domain is reconfigured to match that used for solute transport and discretised with a uniform grid (see Figure 3.2) to capture the thermal evolution of both

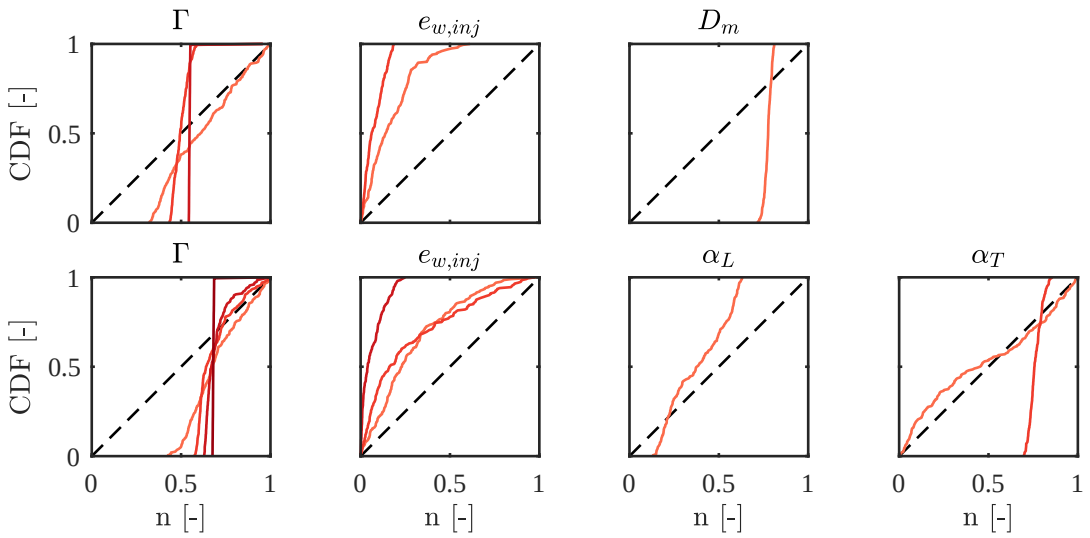

Figure 4.7: Staged prior and posterior CDFs for calibrations 1 (top row) and 2 (bottom row). Parameter ranges are normalised (n [-]) by their upper and lower bounds. Darker shades of red correspond to later stages.

Calibration	Stage:	1	2	3	4
1	Γ	0.32	0.44	***0.542***	
	$e_{w,inj}$	0.57	***0.81***		
	D_m	***0.72***			
	$max(\langle\varepsilon^{abs}\rangle)$	0.32	0.14	0.13	
2	Γ	0.45	0.58	0.63	***0.68***
	α_L	***0.37***			
	α_T	0.13	***0.70***		
	$e_{w,inj}$	0.36	0.37	***0.77***	
	$max(\langle\varepsilon^{abs}\rangle)$	0.38	0.28	0.15	0.13

Table 4.3: Summary of K-S scores for a progressive Monte-Carlo analysis of calibrations 1 (strong conduction) and 2 (strong dispersion), showing the calculated maximum $\langle\varepsilon^{abs}\rangle$ of the top 1% of results.

wells. Additional conditions are applied:

$$\begin{aligned} e_{w,inj} &= e_{w,o(BH2)} \quad t \geqslant 0, \\ e_{w,abs} &= e_w(\frac{L_x}{2} - \frac{L_{BH}}{2}, \frac{L_y}{2}, 1, t) \quad t \geqslant 0, \\ Q_{BH2} &= Q_{o,t,BH2} \quad \text{and} \quad Q_{BH1} = Q_{o,t,BH1} \end{aligned} \tag{4.17}$$

where $e_{w,o(BH2)}$ [Θ] is the observed temperature of the injected fluid during operation (Figure 4.1, bottom panel, red markers), and $Q_{o,BH1}$ [L^3T^{-1}] and $Q_{o,BH2}$ [L^3T^{-1}] are the observed pumping rates for BH1 and BH2, respectively (Figure 4.1, top panel, solid lines). Temperatures and flow rates are linearly interpolated as required.

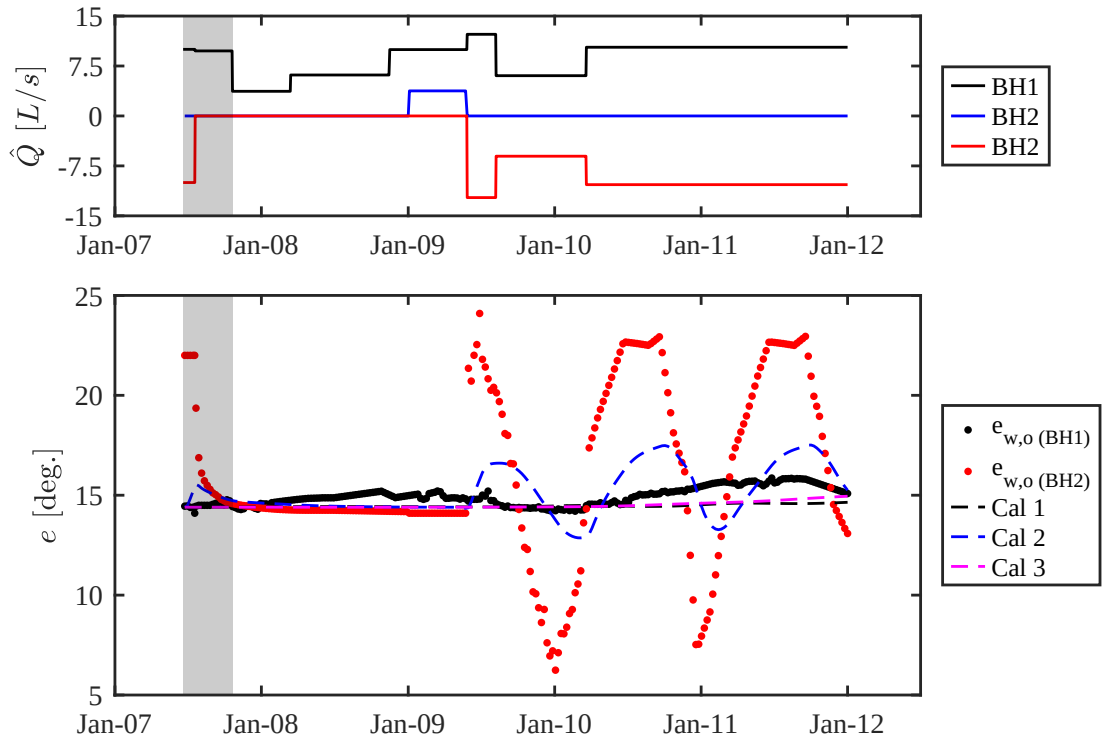

Figure 4.8: Comparison of calibrated simulations with operational data. Top panel shows the applied average flow rates, with BH1 abstracting and BH2 both injecting and abstracting. Bottom panel shows reported average temperatures for both wells and the resultant simulation temperatures for BH1. Calibration window shown (grey shaded area).

The results are shown in Figure 4.8, which displays the average pumping rates, the injection temperatures ($e_{w,inj} = e_{w,o(BH2)}$) and the simulated temperatures at BH1 ($e_{w,s(BH1)}$). The simulations are unsuccessful in reproducing the low, undulating temperature fluctuations observed at BH1. Calibration 1 (strong conduction) parameters result in negligible thermal influence at BH1, whereas calibration 2 (strong dispersion) parameters cause strong influence of a completely different magnitude and character to the observations. Calibration 3 (two layers) parameters result in a small influence that becomes stronger at later times.

Further investigation was conducted, but was unable to reproduced the observed fluctuations. This investigation included attempting a calibration directly with the operational data, as well as exploring conduction through additional layers above and below. These results are inconclusive with regard to the cause of the

unexpected thermal fluctuations at BH1, but suggest that the cause is unlikely to be miscalibration. Calibration 2 (strong dispersion) predicts behaviour at BH1 that is clearly incorrect. Calibrations 1 and 3 result in partial or negligible influence at BH1, but within the bounds of what was observed. It is possible that the observed behaviour is wholly or partially due to fluctuations in the background temperature of the aquifer, rather than thermal breakthrough.

Rather than nominal fluctuations in background temperature, the observed temperature variations may potentially be attributed to interference from a nearby GSHS. An open-loop GSHS does not appear to be in relative proximity to RFH, however it remains possible that a closed-loop GSHS is present. Closed-loop GSHS do not face the same regulation and licensing requirements as open-loop schemes, making their locations and thermal effects difficult to identify (see Abesser et al., 2018, for insight on regulatory conditions). Herbert, Arthur, and Chillingworth (2013) identified unexplained temperature fluctuations and suspected interference from a nearby closed-loop scheme, with their suggestion equally remaining speculative due to absent records.

4.5 Discussion and Conclusions

Research into observed thermal behaviour at RFH has been conducted in an effort to calibrate the apparent thermal properties of the aquifer and provide operational insights. Hydraulic and solute transport characteristics acquired from the previous two chapters, were adopted and used to constrain a study of thermal transport. The study constructed a model for thermal transport within a horizontal aquifer domain, capable of one and two-layer configurations.

The attempt to simulate the observed thermal behaviour in BH1 at RFH took a unique route of isolating a thermal-decay event within an operational system's historical data, but was inconclusive, despite demonstrating the ability to simulate said event. This failure raises several points of discussion and implications for further assessments, chiefly highlighting the limitations modelling faces when under-constrained. Firstly, the three calibration efforts (strong conduction, strong

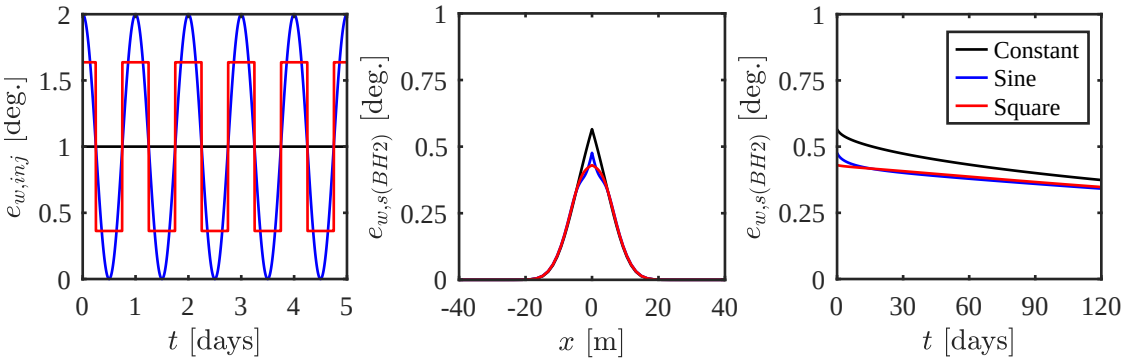

Figure 4.9: Investigation of injection mode on resultant thermal plume within the aquifer. Left panel shows injection temperature profiles following constant, sinusoidal and square-wave profiles (each an alternative idealisation of daily operation). Middle panel shows cross-section through x-axis of BH2 after 5 days of constant-rate injection at 10 L/s for a given mode of injection — all temperature profiles correspond to the same total energy injected. Right panel shows corresponding thermal decay curves for a 120 day period of no pumping.

dispersion and two-layers) were all conducted by injecting the same reported total thermal energy into the aquifer via a constant injection temperature and a constant flow rate. This approach was necessitated by the gap in temperature records immediately preceding the decay period (Clarkson et al., 2009). The true thermal plume at the end of the injection period is likely to have differed from the simulated one due to fluctuating injection temperatures during the 29 days of injection. To assess whether the nuances of the real operational characteristics have a strong impact on the shape of the decay curve, an additional sensitivity analysis was conducted. The results are shown in Figure 4.9. Three different modes of injection were trialled (constant, sinusoidal and square wave), all injecting the same quantities of thermal energy. The results show near-well differences, but similar plume characteristics in the wider domain. Despite the wider similarity, the localised effect of the operational nuances appear to influence early-time behaviour in the decay curves. The difference is not expected to account for the rapid decay observed within the operational data, lending confidence to the approach adopted by calibrations.

It is not known whether the simplifying assumptions of averaging flowrate and temperature data on weekly or longer intervals causes a critical reduction in

the ability to simulate observed behaviours. Weekly averages were necessitated in this study due to the large quantity of operational data that was gathered at inconsistent intervals (spanning resolutions of seconds to years). Weekly averages mitigate poorly constrained periods of less-dense data while sacrificing higher time resolution in other periods.

The ability of the three calibrations to replicate an observed thermal decay curve highlights a lack of constraint within the physical problem and/or a lack of distinguishability in individual thermal characteristics. In the first two calibration efforts, it was assumed that the horizontal injection flux is uniformly distributed along the thickness of the aquifer and that the water in the well equilibrates nearly instantaneously to the temperature of the injected fluid. It was also assumed that the temperature readings from the installed sensor are representative of the temperature along the entire height of the fluid column within the well. As a result, the thermal-decay period begins with the sensor surrounded by a plume of relatively high temperature. The calibrations then rely heavily on either conduction in the matrix or dispersion due to weak flow toward BH1 to dissipate the thermal energy surrounding BH2. The resulting best-fit conductive and dispersive properties deviate significantly from expected values.

In the third calibration effort, the EC was split into two layers to allow the sensor to be modelled within a portion of the well that was not in direction hydraulic communication with the aquifer. As a result, the initial condition surrounding the sensor (in the horizontal plane) at the commencement of the decay period was produced through conductive exchange only. This placement significantly reduced the thermal energy requiring dissipation and the resulting matrix thermal diffusivity was much closer to the expected value, although still elevated. This somewhat elevated value could be explained by variability in the thermal conductivity, specific heat capacity and density of the EC (Ellison et al., 2004; Allen et al., 1997; Bloomfield, 1996). For example, Busby (2018) notes a thermal-conductivity range of 1.53–2.77 [W/(m.C)]. The results indicate that the physical conditions of the aquifer and sensors are likely to be similar to those

described by calibration 3. Despite the more palatable parameter values, the inconclusive nature of the operational simulations makes it difficult to comment on the accuracy of the calibrated parameters for RFH.

To adequately constrain future thermal calibration tests of the type presented here, further assessment and investigation is required. Results suggest that the calibration is sensitive to the thermal storage and flow characteristics of the well. Geophysical and geotechnical investigation should seek to identify the vertical heterogeneity of horizontal flow and temperatures within the well (as observed in Boon et al., 2020; Law, 2010; Law and Mackay, 2010). Consideration should be given to the thermal-sensor placement so that readings target the desired environment; the installation of multiple sensors may be appropriate. In the absence of site-scale, single-well thermal tests, laboratory-scale tests can be conducted to evaluate the apparent thermal properties of representative core samples, provided that drilling procedures allow for the recovery of samples (Law, 2010; Law and Mackay, 2010). These various investigative efforts aim to constrain the material and transport properties of the aquifer so that the remaining thermal calibration efforts can more readily identify thermal dispersion, fracture-matrix interactions and potentially 3D effects.

The observed behaviour at BH1 remains unexplained. It is possible that the behaviour is the result of GSHS operation, but that the thermal evolution was not adequately captured by the constructed models. However, the behaviour could also be attributed wholly or partially to fluctuations and regional trends in the background temperature of the EC (Headon et al., 2009; Environment Agency, 2018). Both regional and operational factors are expected to influence the thermal behaviour of BH1, but their degrees of contribution remain unknown. As highlighted by Herbert, Arthur, and Chillingworth (2013) and the present study, it is also possible that the observed behaviour is partially or wholly caused by interference from an unidentified GSHS. The inability to confirm the presence, or lack thereof, of additional thermal sources within the proximity of the RFH site contributes to further lack of constraint in the adopted models. While speculative

due to a lack of evidence, these results support the argument for structured and regulated management of heat as a resource, which would aid the clear identification of heat sources/sinks within an aquifer.

In the interest of understanding and optimising the operation of RFH and similar systems, it remains concerning that the cause of the thermal behaviour observed at BH1 is yet to be conclusively identified. It is hoped that future studies will either be able to identify the behaviour as thermal breakthrough, along with its contributory mechanism, or rule out thermal breakthrough in favour of regional temperature fluctuations in the EC aquifer. This might potentially be achieved through the acquisition of regional temperature data that this study did not acquire, as well as information about nearby GSHS installations / other heat sources within the aquifer. In general, the results suggest that GSHS operators should be continually monitoring regional temperature as both a calibration and operational metric. Further understanding in this area, and the ability to accurately capture, constrain and model thermal behaviour, will undoubtedly aid the design and management of open-loop ground source heating systems as they are increasingly installed in proximity to other systems.

5

Operational Strategies and Thermal Transport Properties

Contents

5.1 Introduction

Open-loop GSHSs are increasingly being installed within the aquifers of the United Kingdom to provide heating and cooling to buildings and for use as regional heating-cooling networks (Younger, 2008; Boon et al., 2019; Boon et al., 2020; Monaghan et al., 2022). Many installations already exist within prominent aquifers such as the EC (Environment Agency, 2018; Clarkson et al., 2009; Arthur and Streetly, 2009;

Arthur et al., 2010; Birks, 2019; Birks et al., 2022; Law and Mackay, 2010; Law, 2010). Systems exist and operate in a variety of configurations: single well, doublet or multiple wells, heating-only, cooling-only or heating-cooling. Fundamentally, all involve the abstraction of groundwater from one or more wells; an increasing fraction involve re-injection ('injection') of effluent fluid back into the aquifer.

The advantages of injection are that it avoids the need to dispose of effluent fluid elsewhere (e.g., into a river or lake) and that it mitigates the net hydraulic impact on the aquifer. The disadvantage is that the flow field will eventually carry injected fluid back to the abstraction well (i.e., thermal breakthrough), potentially negatively impacting system performance. The GSHS at the Royal Festival Hall, for example, was installed in the EC in 2006 and was originally operated via abstraction-only with discharge to the River Thames. It was reconfigured to inject effluent fluid a year later, necessitating engineers model and evaluate the expected rate and severity of thermal breakthrough at the abstraction well (see Clarkson et al., 2009, and Chapter 4).

Wells are typically dedicated to either injection or abstraction. Recognising this conventional unidirectional configuration, several studies have been conducted analytically and numerically to evaluate the between-well travel time of injected fluid (Molz et al., 1983; Barker, 2012; Barker, 2010; Banks, 2011b; Banks, 2009b; Clyde and Madabhushi, 1983), the thermal impact of injected fluid, and cyclic injection/feedback patterns (Milnes and Perrochet, 2013; Piga et al., 2017; Casasso and Sethi, 2015). Barker (2010), Banks (2011b), and Clyde and Madabhushi (1983) provide useful analytical derivations, simplified into 'back-of-the-envelope' equations for front-end indications of between-well travel times, but which neglect potentially significant transport mechanisms such as dispersion. Several of the studies highlight the idea of relying on regional groundwater movement to mitigate thermal breakthrough by carrying injected plumes downstream. Beyond respecting the stipulations of the Environment Agency (EA), which include peak warmed fluid temperatures and abstraction volumes, sustainable operational practises have focused on maintaining and prolonging system life rather than impact on other systems (e.g., those located downstream).

The notion of impact on/from adjacent systems in increasingly crowded aquifers raises the matters of system interaction/interference, sustainable operational practises, resource management, liability, licensing levels and environmental impacts (Abesser, 2010; Abesser et al., 2014; Garcia-Gil et al., 2020; Abesser et al., 2018; Abesser et al., 2021). The EA has reported on the EC aquifer, its licensing levels, regional groundwater levels and ambient background temperatures (Environment Agency, 2018). Some assessment of regional thermal impact has been conducted by Arthur and Streetly (2009), Arthur et al. (2010), and Abesser et al. (2021). Further research and experience is required to understand the complexity of increasingly crowded aquifers and manage them effectively in the interest of permitting further installations.

An alternative to unidirectional operation is seasonally reversed operation, in which the wells switch directions seasonally to make use of previously injected thermal energy. Banks (2009b) highlights the parallels between seasonally reversed operation and the practice of so-called aquifer thermal energy storage (ATES), in which excess thermal energy from a surface-based industry (e.g., a power plant) is injected into an aquifer for storage and later recovered via abstraction (Andersson, 1998; Andersson, 2007; Vos, 2007; Bakema and Snijders, 1998; Snijders and Drijver, 2016). In the context of GSHSs, seasonally reversed operation is thought to provide greater operational efficiency and sustainability for an individual system by making beneficial use of effluent fluid rather than leaving it to migrate downstream. Seasonally reversed operation may also help to mitigate the risk of thermal breakthrough. Thus, greater adoption of this operational mode could potentially increase the lifetime of isolated systems and allow for hosting a higher density of installations within an aquifer before encountering adverse interactions.

In this chapter, an analysis is undertaken to assess and compare unidirectional and seasonally reversible operational modes in an RFH-sized system. The analysis considers variable peak energy load, prescribed limits on injection temperature and unbalanced seasonal loading. The two modes are compared to quantify the benefits of seasonal reversibility. Further to this comparison, and considering the outcomes of

Chapter 4, the effects of variable matrix conduction, dispersion and LTNE are also investigated and quantified. The study aims to understand how all of these effects impact thermal breakthrough and the migration of the injected thermal plume.

5.2 Governing Equations

To investigate the operational considerations discussed above, we use the single-layer 2D thermal transport model of Chapter 4. This model represents the horizontal plane of a uniform aquifer with two wells. Figures 3.2 and 4.3 illustrate plane and cross-sectional views of the domain, respectively. The assumptions and conditions mentioned in Section 4.2 still apply, as do Eq. (4.1) to (4.9).

The flow conditions and power inputs/outputs are prescribed as idealised operational curves representing summer cooling and winter heating. The cooling/heating load E [$\mathrm{ML^2T^{-3}}$] is defined as:

$$E(t) = E_p \sin\left(\frac{2\pi t}{t_{yr}}\right) \tag{5.1}$$

where E_p [$\mathrm{ML^2T^{-3}}$] is the peak load and t_{yr} [T] is one year. The polarity of this function represents a cooling load in the summer ($E(t) > 0$, effluent fluid warmer than abstracted fluid) and a heating load during winter ($E(t) < 0$, effluent fluid cooler than abstracted fluid). Operational simulations will assume constant flow rates $\hat{Q}$ [$\mathrm{L^3T^{-1}}$] throughout the year that are defined by the peak load,

$$\hat{Q} = \frac{E_p}{\rho_w C_w \Delta T_{max}}, \tag{5.2}$$

where ΔT_{max} [Θ] is the maximum permitted change in temperature relative to initial background temperature e_0. For convenience, temperatures are measured relative to the background temperature so that $e_0 = 0$. To meet the varying E with a fixed $\hat{Q}$, the difference $\Delta T = e_{w,inj}(t) - e_{w,abs}(t)$ will vary according to

$$\Delta T(t) = \frac{E(t)}{\rho_w c_w \hat{Q}} = \left(\frac{E(t)}{E_p}\right) \Delta T_{max}. \tag{5.3}$$

In the absence of thermal interference at the abstraction well ($e_{w,abs} = 0$), the design injection temperature is simply $e_{w,inj}(t) = \Delta T(t)$. The difference

between actual and design conditions highlights the presence of thermal interference, which can help or hinder operation. Whether interference is helpful or harmful depends on whether it increases or decreases the available temperature difference. The maximum allowable value of $|e_{w,inj}|$ is ΔT_{max}, but the maximum available temperature difference ΔT_a [Θ] is

$$\Delta T_a = \begin{cases} \Delta T_{max} - e_{w,abs} & \text{in summer} \quad (E(t) > 0), \\ \Delta T_{max} + e_{w,abs} & \text{in winter} \quad (E(t) < 0). \end{cases} \tag{5.4}$$

As a result, $e_{w,abs} < 0$ is helpful in summer and harmful in winter, and the reverse is true for $e_{w,abs} > 0$. To measure the degree of thermal interference, we introduce the thermal efficiency η [-]:

$$\eta = \frac{\Delta T_a}{\Delta T_{max}}. \tag{5.5}$$

Values of η greater than one indicate that interference has increased the available energy, while values below one indicate thermal breakthrough, which is counter-productive. Installed building management systems that are coupled with variable-rate pumps are able to exploit $\eta \geqslant 1$ by reducing $\hat{Q}$ and/or increasing ΔT. The present analysis does not model this additional complexity, in order to make unidirectional and seasonally reversed systems more directly comparable. The problem is subject to initial and boundary conditions

$$\begin{gathered} e_w(x, y, 0) = e_m(x, y, 0) = 0, \\ e_w(0, y, t) = e_w(L_x, y, t) = e_m(0, y, t) = e_m(L_x, y, t) = 0, \\ e_w(x, 0, t) = e_w(x, L_y, t) = e_m(x, 0, t) = e_m(x, L_y, t) = 0, \end{gathered} \tag{5.6}$$

The above system is solved numerically as in Chapter 4, with the same domain, discretisation, and numerical method.

5.3 Unidirectional and Seasonally Reversed Operational Modes

The model is used to simulate and compare unidirectional and seasonally reversed systems. Simulations provide insight into the operating characteristics of each mode independently prior to comparison.

5.3.1 Unidirectional Operation

For unidirectional operation, the two wells operate with singular purposes, one abstracting and one injecting. The constant flow rates are

$$Q_{BH1} = \hat{Q} \quad \text{and} \quad Q_{BH2} = -\hat{Q}, \tag{5.7}$$

such that both warmed fluid and cooled fluid are injected in BH2 over the operational year. The thermal efficiency depends solely on abstraction temperatures at BH1.

The characteristics of the unidirectional mode were investigated for the following conditions: $E_p = 800$ kW, $\Delta T_{max} = 4$ °C and a simulated period of two years. The resulting system conditions and simulated performance/temperatures are illustrated in Figure 5.1. Three key events occur in the simulated period, marked by numbered event boxes. The first event [1] is the first temperature increase at the abstraction well, which is thermal breakthrough, and is accompanied by a reduction in η. The second event [2] is the full propagation of the thermal breakthrough at the abstraction well. However, since the system is in heating mode, the thermal interference manifests as an increase in η (warmer abstraction temperatures increase ΔT_a for heating). Finally, the third event [3] occurs as the system switches back to cooling mode. The abstracted fluid temperature is still elevated due to thermal breakthrough, decreasing ΔT_a for cooling and resulting in a drop in η. A failure criterion of 90% efficiency is marked in Figure 5.1 (bottom right) as a nominal failure point for a system experiencing adverse thermal interference. The long-term consequence of a system dropping below 100% efficiency is not immediately evident from the figure, but can be deduced from Eq. (5.3): the system injects fluid at a higher temperature than initially designed, potentially leading to cascading thermal interference at future times. Milnes and Perrochet (2013), Casasso and Sethi (2015), and Piga et al. (2017) study the evolution of this cascading interference, which they term 'thermal recycling', but focus predominantly on evaluating and defining its evolution in time rather than managing or mitigating it.

Note, the present study will adopt the terminology of *thermal interference* over the more common term of *thermal breakthrough*, due to the default negative

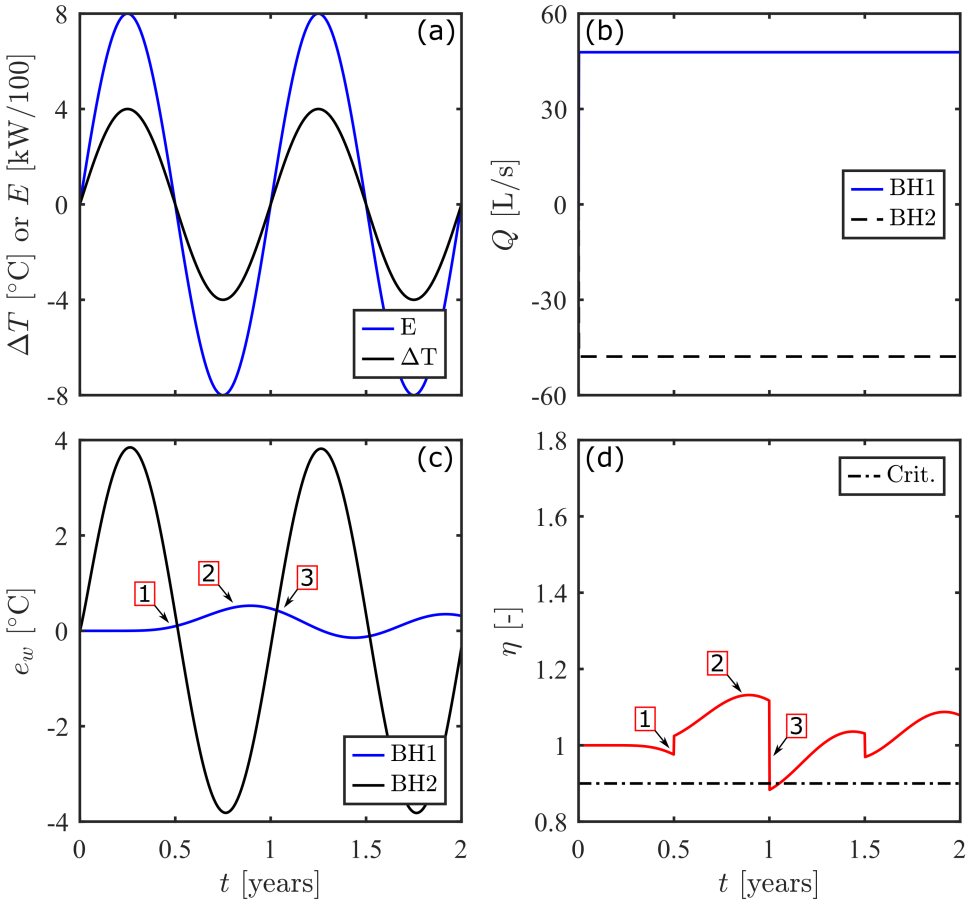

Figure 5.1: Example of unidirectional operational: (a) Prescribed energy load (E) and corresponding ΔT, (b) Design well flowrates $\hat{Q}$, (c) simulated temperatures at each well (e_w), and (d) system efficiency with nominal failure criterion ('Crit.', $\eta < 90\%$). Key events highlighted by numbers: [1] First thermal interference and reduced ΔT_a, [2] increased ΔT_a due to positive use of breakthrough thermal energy, and [3] reduced thermal efficiency due to prolonged thermal breakthrough

connotations of the latter. As shown by the events in Figure 5.1, thermal interference can have both positive and negative impacts on operation. This distinction becomes increasingly important when navigating the deliberate use of injected thermal stores via seasonally reversed operation. Hence, η is used to convey the positive or negative nature of thermal interference.

5.3.2 Seasonally Reversed Operation

For seasonally reversed operation, the two wells switch between abstraction and injection from season to season. The flow rates are

$$Q_{BH1} = \text{sign}(E(t))\hat{Q} \quad \text{and} \quad Q_{BH2} = -\text{sign}(E(t))\hat{Q}, \tag{5.8}$$

such that warmed fluid is injected into BH2 during summer months and cooled fluid is injected into BH1 during winter months. The thermal efficiency is calculated through Eq. (5.4), recognising the changing well assignments.

A seasonally reversed system is investigated under the same conditions. The results are illustrated in Figure 5.2. Four key events occur during the simulated period. The first event [1] is thermal interference at the abstraction well, as seen in Figure 5.1 and again corresponding to a loss of efficiency. The second event [2] occurs as the system reverses flow direction, such that previously injected thermal energy is withdrawn from BH2, thereby increasing ΔT_a and η. This behaviour matches the design principles of ATES: the temporary storage of thermal energy within the ground. The third event [3] occurs as the system switches direction again. The temperature in BH1 has been elevated due to the injection of warm fluid reducing η when BH1 suddenly becomes the abstraction well. Unlike the third event of the unidirectional system, this inefficiency is short-lived as the renewed abstraction at BH1 pulls the wider plume of cooled fluid back through the well. After events [1] and [3], the additional efficiency follows a pattern of peaking and then decaying throughout the seasons, reaching an end-of-season low as seen at event [4]. Overall, the seasonally reversed system predominantly operates in high-efficiency ranges for the simulated period.

5.3.3 Comparison of operational modes

A comparison of the two operational modes was conducted, exploring several key system characteristics and their implications. The following conditions are explored:

- Varying E_p for a given ΔT_{max},

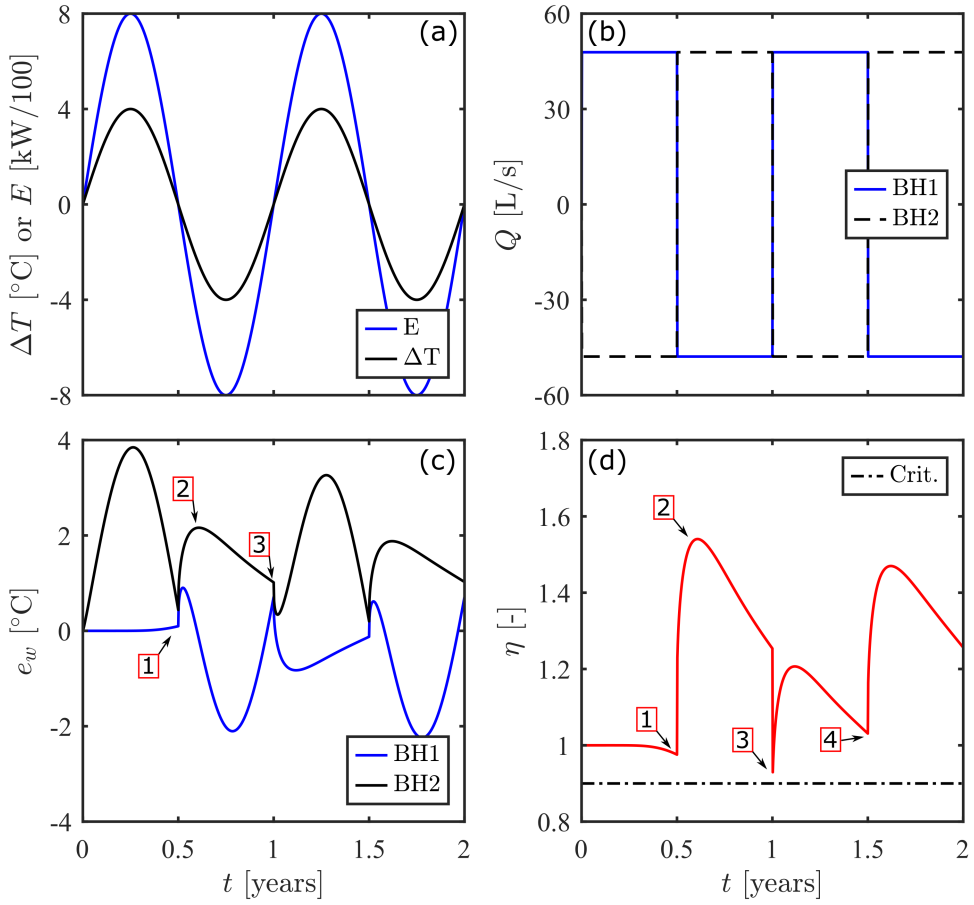

Figure 5.2: Example of seasonally reversed operation: (a) Prescribed energy load (E) and corresponding ΔT, (b) Design well flowrates $\hat{Q}$, (c) simulated temperatures at each well (e_w), and (d) system efficiency with nominal failure criterion ($\eta < 90\%$). Key events highlighted by numbers: [1] First thermal interference and reduced ΔT_a, [2] increased ΔT_a due to positive use of stored thermal energy, [3] momentary reduced thermal efficiency due to switching flow directions and [4] the late-season η which acts as a better indicator of overall thermal interference than [3]

- Varying ΔT_{max} for a given E_p, and
- Introducing seasonal imbalance for a given E_p and ΔT_{max}.

The various comparisons assume local thermal equilibrium (LTE). Total simulation time varies as appropriate for each comparison.

Varying E_p

The effect of varying E_p was explored by simulating a 10 year period, assuming $\Delta T_{max} = 8$ °C, and $E_p = 100$ to 800 kW. The results are shown in Figure 5.3.

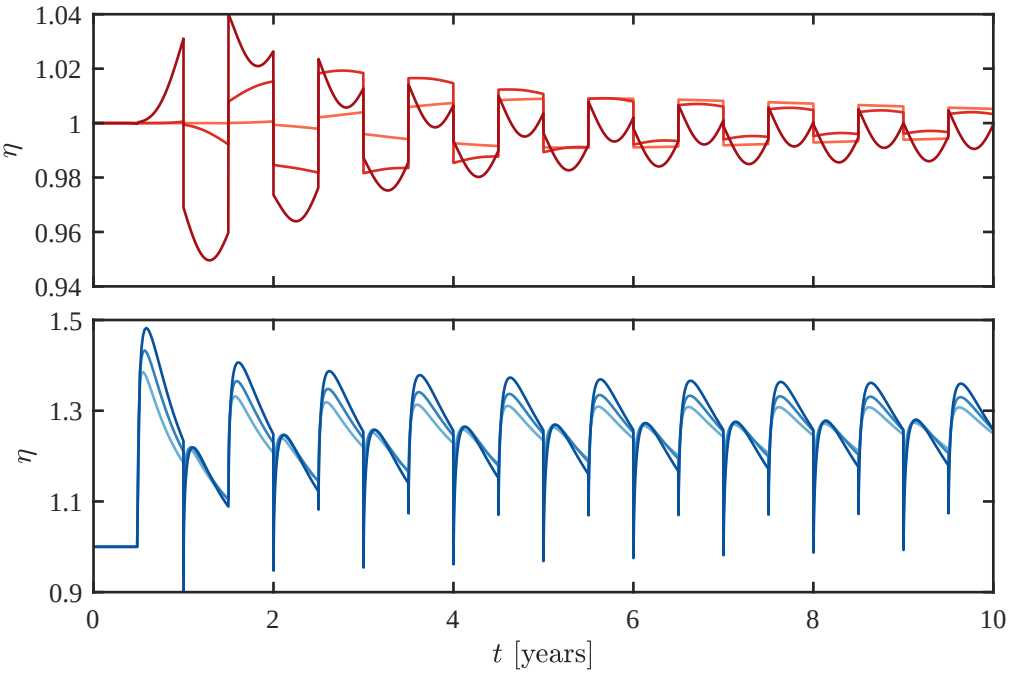

Figure 5.3: Effect of variable E_p on η for unidirectional (top) and seasonally reversed systems (bottom). Darker shades represent increased E_p ($E_p = 200, 400$ and 800 kW, respectively)

Increased E_p for a given ΔT_{max} is accommodated through changes in $\hat{Q}$, and results in a more dynamic system with larger peaks and troughs in η. On average, the unidirectional system experiences significantly lower η in comparison to the seasonally reversed one and experiences thermal interference for prolonged periods of time. The range of η for each system type narrows with increased simulation time, suggesting that the system is evolving toward a quasi-steady state following the initial thermal disturbance of operational activation.

The maximum, mean and minimum η of each mode for the period of operation are shown in Figure 5.4. The minimum η of the seasonally reversed system is misleading as it results from a brief effect detailed in Section 5.3.2. The larger peaks and troughs of increased ΔT_a are evident through the plot. Overall, the maxima and minima continue to evolve as E_p increases, while the means appear to plateau. For this scenario, a seasonally reversed system is approximately 25% more efficient (in the sense of η) than its unidirectional counterpart.

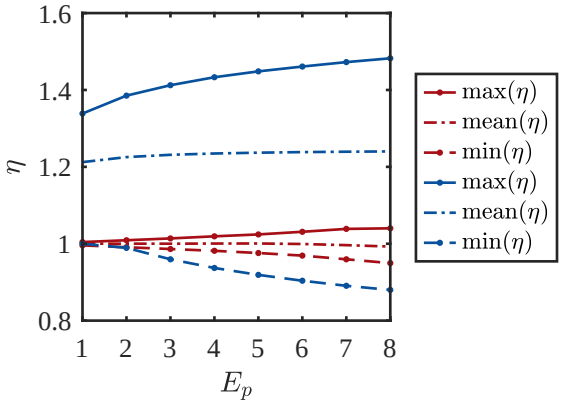

Figure 5.4: Maximum, mean and minimum η for unidirectional (red) and seasonally reversed (blue) systems for a 10 year operating period with respect to E_p.

Varying ΔT_{max}

The effect of varying ΔT_{max} was explored by simulating a 10 year period with $E_p = 400$ kW and $\Delta T_{max} = 1$ to 8 °C. The results are shown in in Figure 5.5. As above, the change in ΔT_{max} for a given E_p is accommodated through changes in $\hat{Q}$. More dynamic systems are associated with lower ΔT_{max} (higher $\hat{Q}$). Again, the unidirectional system experiences significantly lower η than the seasonally reversed system.

Similar η relationships are observed to those when varying E_p: seasonally reversed systems have momentary low η, while unidirectional systems experience prolonged periods of low η. Both systems appear to narrow and stabilise their η ranges over time. The maximum, mean and minimum η of each mode over the simulation period are shown in Figure 5.6. Clearly, seasonally reversed systems have a greater mean η than unidirectional systems for all values of ΔT_{max}. For this scenario, the seasonally reversed system is again approximately 25% more efficient than its unidirectional counterpart.

Seasonal Imbalance

Open-loop GSHSs commonly have balanced energy loads between the summer and winter seasons (Banks, 2009a). To investigate the effects of seasonal imbalance, the

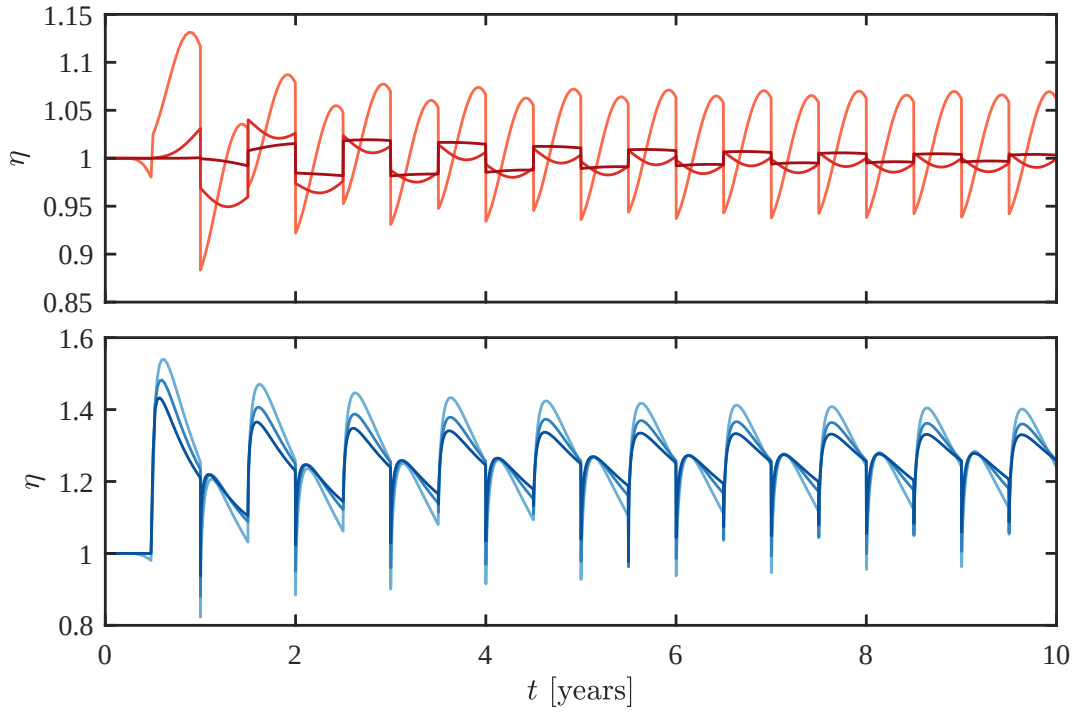

Figure 5.5: Effect of variable ΔT_{max} on η for unidirectional (top) and seasonally reversed systems (bottom). Darker shades represent increased ΔT_{max} ($\Delta T_{max} = 2, 4$ and 8 °C, respectively)

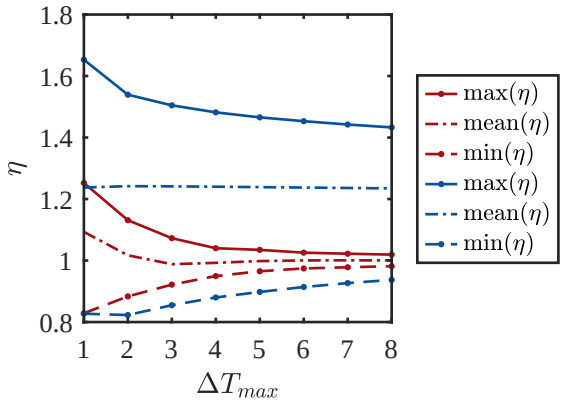

Figure 5.6: Maximum, mean and minimum η for unidirectional (red) and seasonally reversed (blue) systems for a 10 year operating period with respect to ΔT_{max}.

winter heating load is varied while keeping the summer cooling load fixed. To do so, the following additional condition on Eq. (5.1) is introduced:

$$E(t) = \begin{cases} E_p \ \sin\left(\frac{2\pi t}{t_{yr}}\right) \ \text{if} \ \sin\left(\frac{2\pi t}{t_{yr}}\right) \geqslant 1 \\ (1-a_r)E_p \ \sin\left(\frac{2\pi t}{t_{yr}}\right) \ \text{if} \ \sin\left(\frac{2\pi t}{t_{yr}}\right) < 1 \end{cases}, \tag{5.9}$$

where a_r [-] is a load-reduction factor between 0 and 1. Simulations were run for both systems for $E_p = 400$ kW, $\Delta T_{max} = 8$ °C, and with a failure (stopping) condition of $\eta \leqslant 0.9$ for more than 10 consecutive days. The latter is intended to avoid misdiagnosis of thermal interference in the seasonally reversed system (see event [3], Figure 5.2) during the season switch.

The results are summarised in Figures 5.7 and 5.8. Figure 5.7 shows simulations for $a_r = 0, 0.25, 0.5, 0.75$ and 1. From Figure 5.7, both systems appear to trend toward failure unless the thermal load is near perfectly balanced. An imbalance in the seasonal demand results in a net injection of warmed fluid, which causes failure rates proportional to the imbalance. This is attributed to the continual increase in total injected thermal energy, which makes interference at the abstraction well inevitable. The balanced systems (lightest shades) are in-line with the trends observed in previous analyses. The two systems are identical for $a_r = 1$.

Figure 5.8, illustrates simulated and estimated system failure times (t_f) as functions of a_r, as well as the relative difference between the two estimated failure times. Note that simulated failure time was capped at 100 years of operation. Estimated results were calculated by linearly extrapolating the downward trending minimum values of η to $\eta = 0.9$. Good agreement is observed between the simulated and estimated results. The relative difference (ϵ^{rel}) between estimated failure times shows the distinct efficiency advantage of seasonally reversed systems over the unidirectional systems. The change in ϵ^{rel} trend for lower a_r ($a_r = 0.1$ to 0.3) is potentially due to the estimation process adopted.

5.4 Parameter Influences

The scale of matrix conduction, dispersion and LTNE are all of interest when predicting thermal interference and the migration characteristics of injected thermal

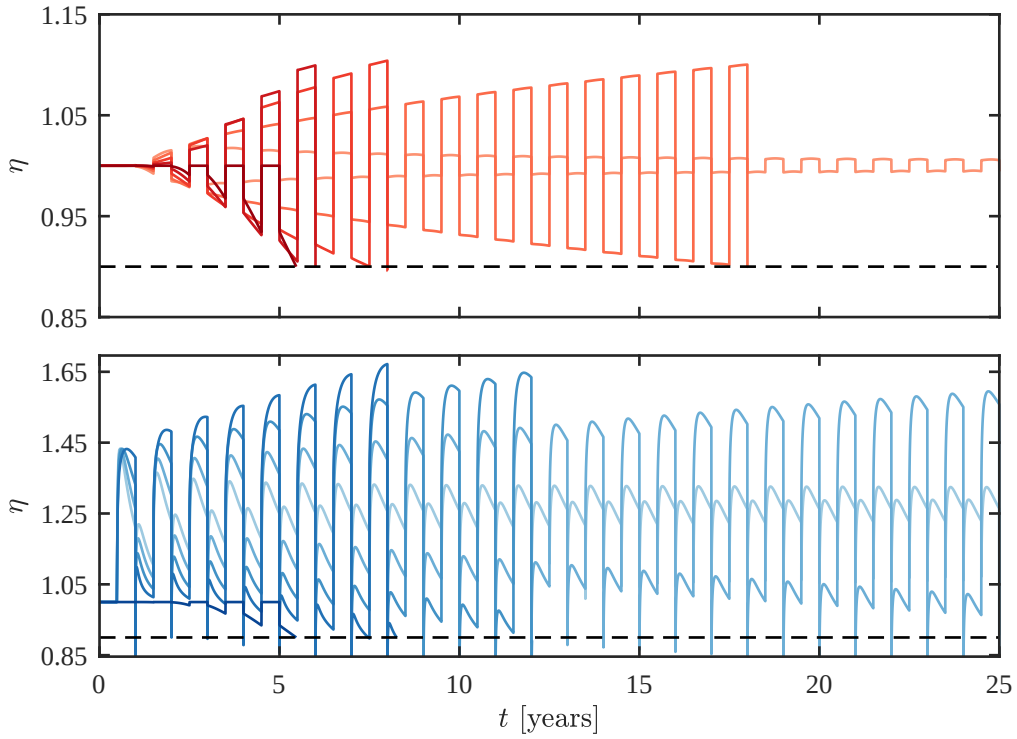

Figure 5.7: Comparison of unidirectional (red) and seasonally reversed (blue) operational modes for varying a_r, incorporating a nominal system failure criteria of 0.9η. Darker shades indicate larger values of a_r ($a_r = 0, 0.25, 0.5, 0.75, 1$).

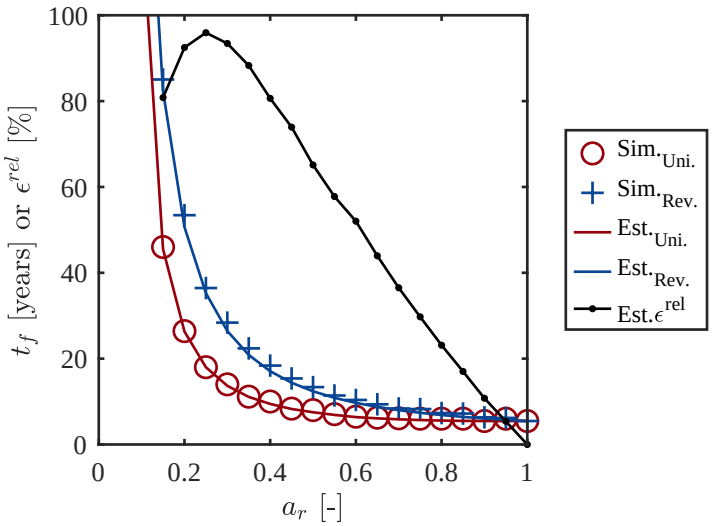

Figure 5.8: Comparison of failure times (t_f) for varying a_r given a system failure criterion of η <0.9 for 10 consecutive days. Markers indicate failure experienced within the simulated time span of 100 years; solid lines indicate estimated failure times. The relative error between estimated failure times for the unidirectional and seasonally reversed systems is also shown.

energy. Chapter 4 aimed to calibrate the scale of each of these effects at RFH, but with inconclusive results. Understanding how each of these transport mechanisms may independently impact the speed and scale of thermal interference remains important and could assist interpreting future thermal events at RFH.

To investigate the influence of other thermal transport parameters on system performance, the applied conditions are further simplified. The time-dependent nature of energy demand, flow rates and injected fluid temperature is removed in favour of constant values, such that the following conditions apply in addition to Eq (5.6):

$$E = E_p, \quad \hat{Q} = \frac{E_p}{\rho_w c_w \Delta T_{max}}, \quad e_{w,inj} = \frac{E}{\rho_w c_w \hat{Q}}, \tag{5.10}$$

thus providing a continuous injection rate and injection temperature at BH2, having removed the cyclic nuance of standard operation.

5.4.1 LTNE

The impact of varying degrees of LTNE was explored for a doublet system experiencing continuous injection at a constant injection temperature. Despite the studies of Chapter 4 suggesting LTE conditions, the impact of LTNE is investigated due to the study in Appendix B which suggests thermal equilibrium between fracture fluid and rock matrix blocks of various sizes can take several days. It therefore remains of concern that the thermal behaviour at RFH could be a result of the thermal front rapidly advancing in the fracture fluid, ahead of the rock matrix. As per Eq. (5.10), a system with $E_p = 400$ kW and $T_{max} = 8$ °C was simulated for 5 years with the same failure condition used above. To explore LTNE, simulations were conducted for Γ ranging from 1E-2 to 1E2 kg/ms^3°C in semi-logarithmic intervals.

Figure 5.9 shows the resulting η with respect to time and the corresponding failure time with respect to Γ. The results indicate that lower values of Γ result in earlier failure, representative of the injected thermal energy increasingly remaining within the fracture fluid instead of conducting to the rock matrix. In this regime, the thermal breakthrough time is governed by the effective flow velocity. A steep transition between highly advective and advective-conductive behaviour is observed

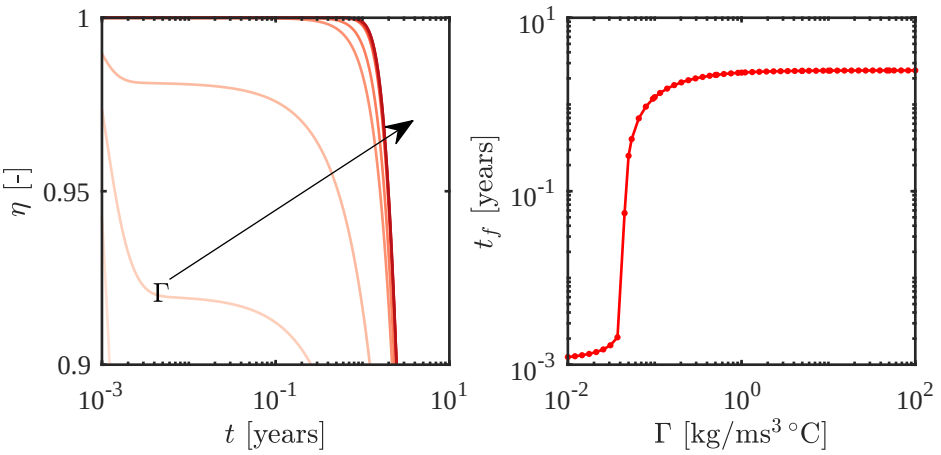

Figure 5.9: Effect of variable conductive exchange between fracture fluid and rock matrix on thermal efficiency and failure time in an RFH-sized system ($E_p = 400$ kW and $\Delta T_{max} = 8$ °C). Left panel shows time evolution of thermal efficiency for Γ increasing semi-logarithmically with darker shades of red. Right panel shows the failure time t_f against Γ.

in the log-log plot of Γ with respect to failure time, approximately between $\Gamma = 0.04$ and 0.1. This transition marks a steep change between LTNE (low Γ) and near-LTE (high Γ). Figure 5.10 shows the thermal energy distribution in fracture fluid and rock matrix continua at the moment of failure for $\Gamma = 0.05$ and 0.1, highlighting the distinct differences between these thermal regimes.

The results indicate that, if RFH were operating under a LTNE regime of $\Gamma < 0.04$ due to its in-situ matrix block size distribution, thermal interference at the abstraction well would be detected in less than a day of continuous injection. As this is not observed at any point in RFH historical data, it is inferred that RFH is under either near-LTE ($\Gamma = 0.05$ to 1) or LTE ($\Gamma >$1E0) conditions, as also suggested by the calibrations in Chapter 4.

5.4.2 Variable Dispersion

As discussed, the calibration results in Chapter 4 suggest exploring the impact of dispersion on thermal evolution and breakthrough. Therefore, the impact of varying degrees of longitudinal and transverse dispersion were explored for a doublet system experiencing continuous injection at a constant injection temperature and

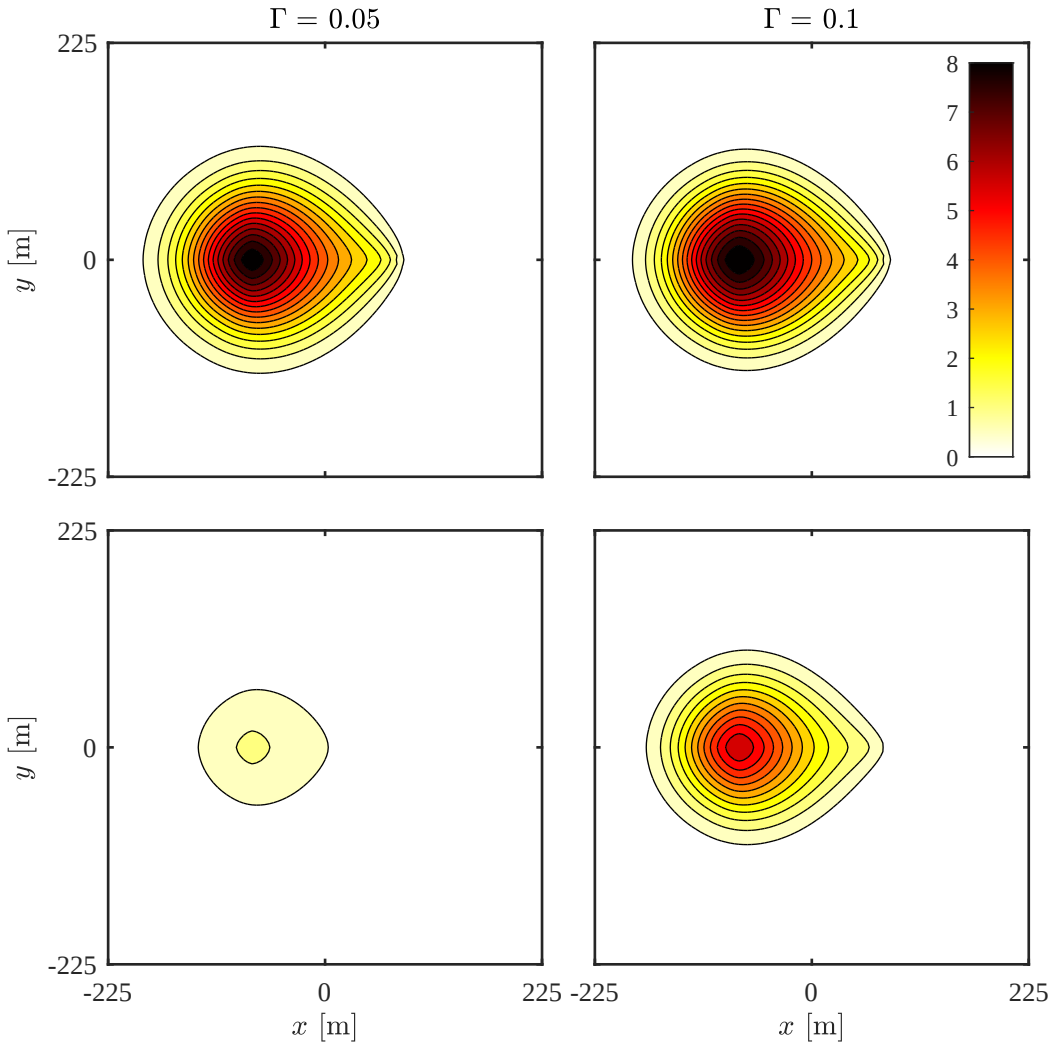

Figure 5.10: Comparison of the thermal energy accumulation within the simulated aquifer at failure, for $\Gamma = 0.05$ and $\Gamma = 0.1$. The top row shows fracture fluid temperature and the second row shows the rock matrix temperature. Contours are at 0.5 °C intervals from 0 to 8 °C.

under LTE. As per Eq. (5.10), a system with $E_p = 400$ kW and $T_{max} = 8$ °C was simulated for 5 years with the same failure condition used above. The impact of dispersion was explored by taking $\alpha_L = a_D \alpha_L^0$ and $\alpha_T = a_D \alpha_T^0$ (where $\alpha_L^0 = 7.4$ m and $\alpha_T^0 = 0.47$ m), as in Table 3.1, and a_D [-] ranging from 1E-2 to 1E2.

Figure 5.11 summarizes the results of this analysis. For $a_D \leqslant 0.1$, the failure time is relatively insensitive to dispersion, marking a predominantly advective transport regime. Dispersion begins to noticeably contribute to the failure for $a_D \geqslant 0.1$. At $a_D \geqslant 30$, the greatly increased dispersion leads to the dissipation of the thermal

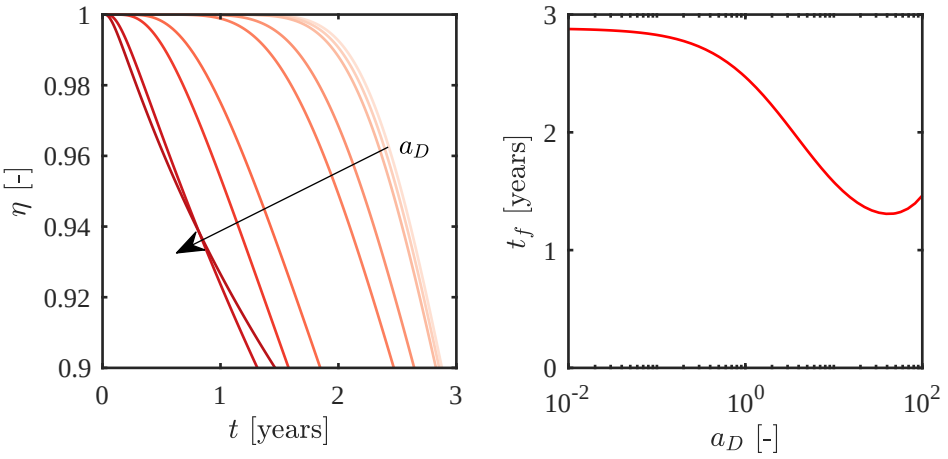

Figure 5.11: Effect of variable dispersion on an RFH-sized system (E_p =400 kW and $\Delta T_{max} = 8$ °C). Left panel shows evolution of thermal breakthrough at the abstraction well for a_D increasing logarithmically with darker shade reds. Right panel shows the failure time against a_D

front before it reaches the abstraction well, thus mitigating failure.

Figure 5.12 shows the thermal footprint at failure for $a_D = 1$, 10 and 100 (same for water and rock in LTE). For $a_D = 1$, thermal contours are tightly grouped and dispersion contributes to the evolution of the thermal plume but does not necessarily dominant the transport characteristics. For $a_D = 10$, the footprint shows a thermal plume of similar size to $a_D = 1$, but more widely spread and with less total energy within the borders of the plume (due to shorter injection duration before failure). Results for $a_D = 100$ show dispersion and boundary effects having distorted the shape of the plume. A wider domain would be necessary to capture the migration of the full plume, but the portion of the plume responsible for failure is captured by the current domain.

5.4.3 Variable Conduction

Finally, the effect of matrix conduction on the migration of the injected thermal energy and failure time is investigated. The impact of varying degrees of conduction was explored for a doublet system experiencing continuous injection, constant injection temperature and LTE.

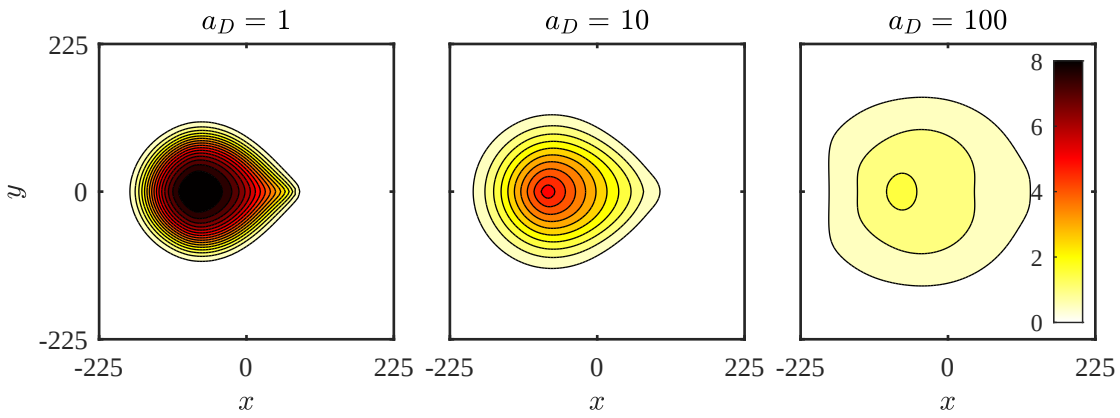

Figure 5.12: Qualitative comparison of the thermal plume within the aquifer at failure for varying amounts of dispersion. Contours at 0.5 °C intervals.

As per Eq. (5.10), a system with $E_p = 400$ kW and $T_{max} = 8$ °C was simulated for 5 years with the same failure condition used above. The impact of matrix conduction was explored by taking $D_m = a_D D_m^0$ with $D_m^0 = 4.79\text{E-}7$ m^2/s as in Table 3.1 and a_D [-] ranging from 1E-1 to 1E3. Figure 5.13 summarises the resulting evolution of η and t_f with respect to time. Failure appears insensitive to $a_D \leqslant 10$, marking a predominantly advective transport regime. Conduction begins noticably contributing to failure at $10 \leqslant a_D \leqslant 100$. For $a_D > 100$, failure is mitigated by rapid dissipation of the thermal front.

Figure 5.14 illustrates the thermal footprint within the aquifer at the time of failure, for $a_D = 10$, 100 and 1000. The increasingly conductive system is reflected in the increasing spread of the thermal contours and the larger coverage area of the plume. For $a_D = 1000$, the plume does not experience the same degree of boundary influence seen for high dispersion in Figure 5.12. The difference between dispersive and conductive footprints observed is attributed to the nature of the two effects: conduction is uniform throughout the domain, whereas dispersion is proportional to the fluid velocity, which is greatest near and between the two wells. Again, while boundary influences are observed in the results presented, the portion of the plume responsible for failure is not compromised.

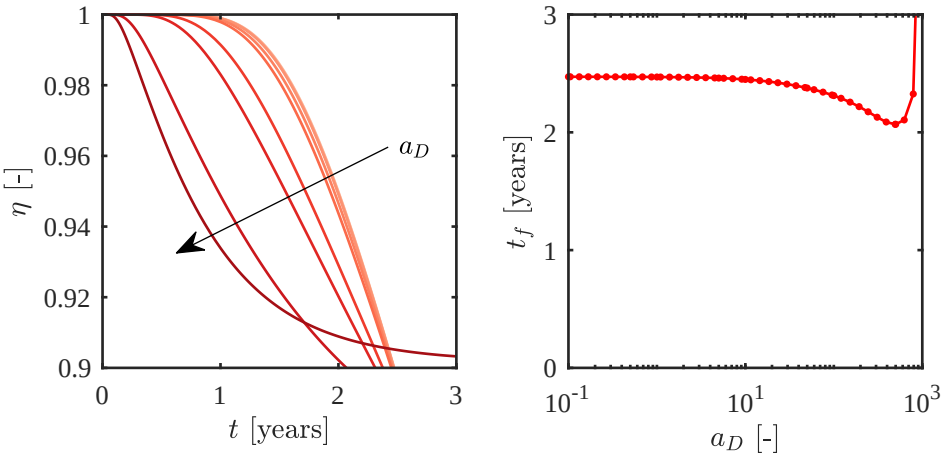

Figure 5.13: Effect of variable matrix conduction on an RFH-sized system ($E_p = 400$ kW and $\Delta T_{max} = 8$ °C). Left panel shows evolution of thermal breakthrough at abstraction well for a_D increasing logarithmically with darker shades reds. Right panel shows the failure time with respect to a_D

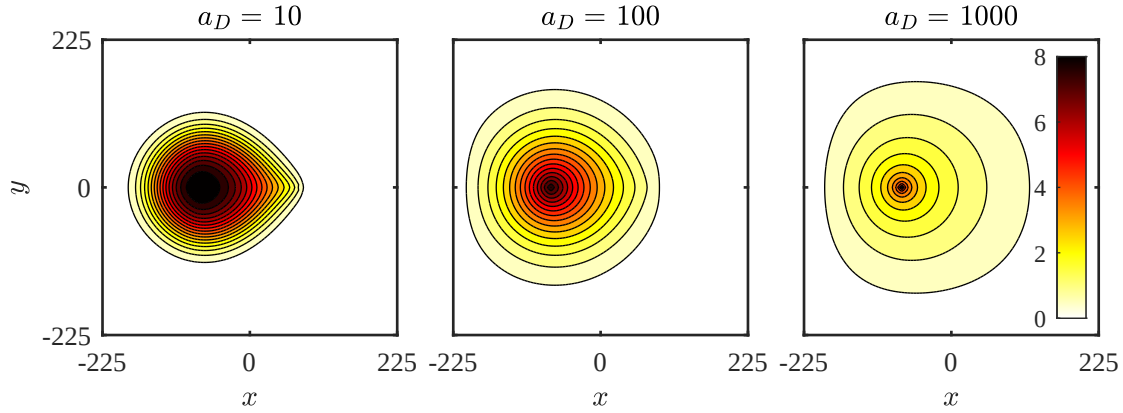

Figure 5.14: Qualitative comparison of the thermal plume within the aquifer at failure for varying amounts of matrix conduction. Contours at 0.5 °C intervals.

5.5 Discussion and Conclusions

An investigation was conducted into the simulated performance differences of unidirectional and seasonally reversed open-loop GSHS. The investigation, which reviewed the impacts of energy demand, maximum injection temperatures and demand imbalance between operating seasons, points to seasonally reversed systems having greater efficiency than unidirectional systems in all instances. This fact was established despite the reversed system operating in a fixed manner rather

than adapting to benefit from the additional thermal stores. In practise, reversed systems would reduce their flow rates and further increase their lifetimes, even further surpassing their unidirectional counterparts.

Typically, unidirectional systems are unable to benefit from adaptability. For a prescribed injection temperature, the system would increase flow rate upon negative thermal interference, which would only increase the severity of the interference. For this reason, unidirectional systems typically adapt their prescribed injection temperatures upon thermal breakthrough and it has been necessary to evaluate the long-term effects of thermal recycling (Milnes and Perrochet, 2013; Casasso and Sethi, 2015; Piga et al., 2017). Periods of thermal efficiency greater than unity did occur at times within the simulated unidirectional system (see event [2], Figure 5.1), but their existence is due to coincidentally timed thermal breakthrough rather than the strategic storage of thermal energy. It is theoretically possible to operate a unidirectional system in a manner that benefits from breakthrough in this way, but doing so would severely constrain operating conditions and would be impractical for a variety of reasons (e.g., the required level of calibration and predictability would be beyond the current state-of-the-art).

The benefit of the seasonally reversed system is clear from a performance perspective, but should equally be noted with respect to broader regional impact. In particular, the interactions of adjacent open-loop GSHSs installed within the same aquifer are increasingly of concern as more systems are being installed within the EC aquifer (Younger, 2008; Environment Agency, 2018; Fry, 2009) as well as other aquifers across the world. The proximity of systems foreseeably leads to more complex thermal interactions and the ability for adjacent systems to cause negative thermal interference. Some such complex thermal interactions are explored by Arthur and Streetly (2009) and Arthur et al. (2010). Seasonally reversed systems operate in a manner that is more likely to localise their thermal plumes, rather than encouraging migration away from or between wells. Neglecting the impact of regional groundwater flows, which would cause a degree of migration, reversed systems are arguably a more responsible and sustainable operational mode.

Following the Chapter 4 suggestions to improve management of thermal sources within an aquifer, it appears naively intuitive from present results to suggest that regulators additionally emphasize more sustainable operating practises, such as the adoption of the seasonally reversed systems.

Finally, the investigation analysed the impacts of dispersion, matrix conduction and local thermal equilibrium on system failure time. The analyses were simulated with energy demands and prescribed injection temperatures similar to RFH (Clarkson et al., 2009)(see also Figure 4.1). In the absence of a clear thermal calibration from Chapter 4, it was of interest to evaluate how the strength of these physical effects would manifest within the operation of a system like RFH. Increased conduction and dispersion typically accelerated thermal interference at the abstraction well, while faster thermal exchange rates between fracture fluid and rock matrix slowed thermal interference. The analysis indicated that RFH likely operates in near-LTE or LTE conditions, as previously suggested by the calibration efforts in Chapter 4. Given the nominal values in Table 3.1 (tracer calibration) and Table 4.1 (material properties), the analyses predict that dispersion makes a notable contribution to the migration of the thermal plume at RFH, while matrix conduction is indiscernible compared with the dominating affects of dispersion and advection.

6

Summary, Discussion & Conclusions

Contents

6.1 Summary, Discussion and Conclusions

Several studies have been conducted into an open-loop GSHS installed in the EC aquifer at RFH, including hydraulic properties, transport properties and operational simulations. The primary motivation of these studies was to potentially explain the thermal events within the system's operational data. These events may be evidence of premature thermal breakthrough. Explaining these events was attractive due to the learnings it would provide industry (regarding modelling and testing assumptions), as well as the confidence it would lend to the industry's ability to accurately predict thermal behaviour. Accurately predicting thermal breakthrough is fundamental to mitigating risk and arguing the economic and functional feasibility of an open-loop GSHS. Therefore, the primary hypothesis of this thesis was that the observed events were thermal breakthrough and that an incorrect assumption or error within the original testing, modelling and/or calibration efforts may have

underpinned the incorrect predictions times. It was further hypothesized that the ability to effectively re-simulate operational data would act to reinforce appropriate testing and modelling assumptions.

Preliminary analysis of the system included the construction of a 2D coupled transient pressure-thermal transport model, which was used to simulate the system's operation by adopting hydraulic and solute-transport characteristics from Clarkson et al. (2009) and Gale, Williams, and Mansour (2006). That model is not documented in the present thesis and was unable to reproduce the observed thermal events. It did however highlight drawdown under pumping conditions that deviated from those reported at RFH. This observation prompted an investigation of both the modelling assumptions and the available pump test data. A 1D radial pressure diffusion model was constructed and used to simulate pump tests. Following unsuccessful attempts to simulate the observed pump tests with the parameters of Gale, Williams, and Mansour (2006) or via calibration assuming a linear flow regime (i.e., Darcy flow), non-linear flow behaviour was incorporated. This model and associated results are reported and discussed in Chapter 2 of the present thesis.

In Chapter 2, the pump tests of RFH and Clark (1977) were investigated. A 1D radial pressure-diffusion model was constructed, adopting Darcy-Forchheimer flow as suggested by Mathias and Todman (2010). An error-minimising approach between simulated and observed data was adopted to calibrate hydraulic parameters for both case studies. Due to the proximity of the two wells at RFH (150 m) the constructed model was used to investigate a grouped-well characterisation of the aquifer, permitting the wells individual expression within a singular parameter — the Forchheimer parameter. The resultant calibration had comparable calibrated parameters with those acquired through calibrating wells individually. The constructed model was also used to calibrate parameters for additional aquifer layers above the EC, but without direct connection to the installed wells. The resultant calibrated parameters were comparable to the single-layer aquifer model and suggested negligible volumetric contribution and error reduction from the additional layers. Good agreement was found between the simulated and observed

pump test data of RFH, concluding calibrated parameters that differed from those suggested by initial design efforts.

The identifiability of parameters for single- and grouped-well calibrations, for both single- and double- layer aquifers, was then evaluated. A progressive Monte-Carlo method coupled with K-S tests was used to identify the sensitivity of the simulated results to each of the free parameters. The simulated curves were most sensitive to a well's Forchheimer parameter and to the horizontal permeability of the primary aquifer. For single-layer models, the storativity, well radius and well casing radius parameters followed with lower degrees of sensitivity and lower overall contribution to the simulation's accuracy. For a double-layer aquifer, the progressive analysis highlighted additional sensitivity to the hydraulic diffusivity of the second layer. The model was least sensitive to the vertical permeabilities and to the Forchhiemer parameter of the second layer, the latter suggesting minimal non-linear flow within the additional layer. The Monte-Carlo analysis indicated the same best-fit parameters that were acquired through the error-minimizing approach, confirming the uniqueness of calibrated parameters.

The constructed pump testing model was adapted from Mathias and Todman (2010) and applied in several novel ways. Firstly, a new boundary condition was utilised to permit the holistic use of pumping data which exhibited sections of flawed data. Flaws within pumping data can occur due to human-error and uncontrollable external factors. These effects can cause the operation of the pump to vary from prescribed standard testing methods. Calibrating hydraulic parameter from the data poses difficulties and inherently faces scrutiny. Through recognising that the pressure-diffusion model can be driven by either a flow rate or pressure level within the well, the new boundary condition switched from a standard prescribed flow condition to a pressure condition, and simulated the observed drawdown. Once the flawed region of data was surpassed, the well flow condition was reapplied. This is an attractive calibration technique as it simulates the observed physical condition of the well and arguably overcomes the aforementioned scrutiny. Further acknowledging the ability to apply a pressure condition within the simulated well, the model was

also used to back-calculate average pumping rates for pump tests based on observed drawdown — a reversal of the typical calibration method. Finally, additional pump testing was conducted at RFH a year following the initial pump tests and calibrations. The model was used to evaluate these additional tests: comparing, re-calibrating and evaluating their behaviour in light of an elapsed year in time. Re-calibration was achieved and the merits of assuming which parameters have changed in time were discussed. The analysis indicated that the well's performance was most sensitive to changes in the near-well region of the aquifer and that re-calibration of the regional aquifer properties was unjustified.

In Chapter 3, a tracer test was used to investigate the transport characteristics of the EC aquifer at RFH. Chapter 2 found that the hydraulic parameters at RFH likely differed from those assumed in the initial transport calibration efforts and 3D `MODFLOW/MT3D` model. A 2D model was constructed to simulate a fluorescein tracer test, assuming a single-layer aquifer, advective-dispersive-diffusive transport with sorption, and a steady flow field. The steady-state flow field was justified following a comparison between the transient and steady-state fluxes. An error-minimising approach was adopted to match simulated and observed tracer breakthrough curves. The model calibrated parameters for effective porosity, longitudinal dispersion, transverse dispersion, average flow rate, rock surface sorption and tracer injection duration.

The calibrated best-fit parameters simulated a tracer breakthrough curve which resulted in lower mean absolute and mean relative error to the previous calibration by Clarkson et al. (2009). Similar to Clarkson et al. (2009), the calibrated effective porosity was relatively low and suggested a fracture network. Calibrated longitudinal and transverse dispersion coefficients were of a similar magnitude to literature suggestions (Gelhar, 1993). The rock surface sorption component was attributed with manipulating the tail of the breakthrough curve. The mathematical similarity of surface sorption to additional aquifer layers or matrix diffusion was noted. A study into the time-scale and contribution of matrix diffusion concluded it was not likely to be significant for the calibration of the tracer test (see Appendix B). As

seen in Chapter 2, a progressive Monte-Carlo analysis coupled with K-S tests was conducted to investigate the sensitivity of the simulation to calibrated parameters. Effective porosity and longitudinal dispersion were found to be the most sensitive and identifiable parameters, responsible for producing the early-time peak of the breakthrough curve. Transverse dispersion was shown to have low sensitivity, while the calibration was found to be insensitive to injection time duration. Ultimately, investigations identified differing yet plausible hydraulic and transport properties to those initially used by RFH designers.

Chapter 4 adopted the learnings and calibrated parameters of the previous two chapters and focused on two core tasks: attempting to isolate an early thermal event to perform a thermal parameter calibration and simulating observed operational data with the benefit of all prior calibrations. A 2D thermal transport model was constructed, which assumed an advective-dispersive-conductive domain, conduction within the rock matrix, and steady flow within the fracture fluid. A pump-testing period at RFH was isolated for calibration efforts due to data showing the injection of warmed fluid and a clear period of thermal decay within the injection well. As per previous chapters, an error-minimising approach between observed and simulated results was adopted to calibrate parameters. Initial calibration attempts (not presented in this thesis) strictly adopted the acquired hydraulic and solute-based calibrated parameters and constrained remaining free parameters to physically feasible limits. Under these conditions, a calibration could not be achieved; simulations indicated that the reported total energy injected (194.1 MWh) could not be adequately dissipated. Potential explanations for this disagreement included that the continuum approach was insufficient to model the discrete thermal behaviour in the EC aquifer, that the reported figures in Clarkson et al. (2009) were somehow incorrect or unintentionally misleading, or that key assumptions regarding flow and temperature distribution were inappropriate.

An answer was sought by exploring each of the explanations for their merit. Three 2D model variants were constructed to calibrate against the thermal event: one which allowed strong conduction, one which allowed strong dispersion (therein

ignoring solute calibration efforts) and a two-layer model to represent dormant-in-horizontal-flow regions of a well. Each of the three models reproduced the observed thermal decay behaviour with reasonable error tolerances. The plausibility of each of the models was then scrutinised. The strong-dispersion model was considered least plausible since it varied considerably from expected dispersion characteristics and predicted much stronger thermal interference at the abstraction well than was observed in the operational data. The strong-conduction model suggested diffusion parameters that were two orders of magnitude greater than physically expected, again unlikely to be physically plausible. Finally, the dual-layer calibration yielded physically plausible parameters and its physical conceptualisation (the idea that the thermal sensor was not positioned within a horizontally flowing region) was again plausible when accounting for studies of the fracture network and heterogeneity of the EC aquifer (see Allen et al., 1997; Bloomfield, 1996; Ellison et al., 2004, etc.). Despite the acquisition of a plausible calibration and scenario, the procedure unfortunately highlighted the under-constrained nature of thermal calibration at RFH.

The operational history of RFH between June 2007 and January 2012 was collated by combining, cleaning, and merging data from multiple reports and publications on the site. Collation efforts involved isolating the weekly averaged flow rates and temperature readings of both wells. As first highlighted by Birks (2019), several inferred thermal breakthrough events were noted and visible within the data. The operational period was then simulated with the three 2D model variants and their calibrated parameters. The simulations applied the reported flow rates and injection (BH2) temperatures, while monitoring abstraction (BH1) temperatures. The three separate approaches were unable to reproduce the observed temperature fluctuations in BH1. An additional calibration effort was conducted by omitting prior thermal calibrations and using the error-minimising approach directly on the operational history data. These results highlighted the need to thoroughly consider the application and positioning of thermal sensors to permit the derivation of various behaviours. It is perceived that clear delineation of injected fluid temperature and

well temperature would aid modelling, as would the placement of multiple vertically-spaced well temperature sensors. While discrete fracture models are expected to more actually account for thermal diffusion within the EC's fractures and rock matrix, it is not known whether they offer considerable modelling advantages with respect to the large time-scale investigated at RFH. The lack of a conclusive finding in operational calibrations and back-analysis is disheartening but informative in its own right. Further work on the topic is considered in Section 6.2.

Finally, an investigation into several operational considerations was conducted. A comparison of unidirectional and seasonally reversed operational strategies was conducted on a RFH-sized system. The analysis used a 2D model which assumed steady-state flow, advective-dispersive-conductive thermal transport in fractures, conduction-only transport in the rock matrix and local thermal equilibrium. Calibrated hydraulic and solute-transport parameters were adopted. Idealised seasonal energy load curves were applied and various configurations of injection temperature, peak energy demands and seasonal imbalances were explored. The analysis clearly outlined the operational benefits of assuming a seasonally reversed strategy for an open-loop GSHS. Previously the strategy's benefit has only been theoretically highlighted (e.g., see Banks, 2009b), while the present study has quantified the benefit through numerical methods, while also accounting for practical operational factors. Further work to extend the implications of this study to various alternative configurations is discussed in Section 6.2.

With the use of the constructed 2D model, the impact of matrix conduction, dispersion and LTNE scales was investigated under continuous unidirectional flow and injection conditions. The investigation of matrix conduction found that conduction began to notably contribute to failure times at 3–100 times its nominal value. Dispersion between 0.1 and 30 times the solute-calibrated values greatly contributed to earlier failure times, indicating that dispersion is likely a non-negligible transport mechanism for the fracture fluid at RFH. Finally, LTNE was investigated with Γ values of 1E-2 to 1E2. A steep transition period between distinct LTE and LTNE behaviour was observed at approximately $\Gamma = 0.04$ to 0.1, with

LTNE leading to substantially earlier failure times. Failure times were insensitive to Γ values greater than 1, indicating LTE. Unlike in granular porous media, which have been the subject of several studies (Rees, Bassom, and Siddheshwar, 2008), the applicability of LTNE remains a point of discussion for fractured media. A study of thermal conduction rates in varying matrix block sizes bound by fractures was conducted (see Appendix B) and indicated that, at small time-scales (less than a few days) LTE is not expected for the EC. However, calibration and operation analysis strongly suggested that RFH was operating under LTE. Use of LTNE in multi-continuum modelling of the EC aquifer may 'effectively' capture the conductive behaviours explicitly captured by discrete fracture model approaches, but has not been studied. The time-scale of the operational thermal events and the sensitive range of Γ in the study above, potentially indicates LTNE is an unnecessary constraint/complexity on the conducted model and calibration efforts.

The presented studies have collectively worked to express the importance of geotechnical, geophysical, hydrogeological and thermogeological investigative testing and instrumentation, accompanied by detailed and appropriate calibration and modelling efforts, to support the design and operation of open-loop GSHS. Confidence in the physical interpretation of the ground conditions and instrumentation readings during testing and operation are crucial to accurately constraining modelling approaches and supporting the simulation of systems and their isolated events. The ability of several models, highly simplified in comparison to commercially available 3D equivalents, to reproduce a number of observed behaviours (at times through several differing approaches) has been shown in the presented studies. This highlights both the potentially unmerited complexity of commercial equivalents, given the negligible gain in value, and that such complexity isn't able to overcome fundamentally under-constrained problems.

A key theme of this thesis has been the investigation of parameter sensitivity and contributory significance within calibration efforts. Progressive Monte-Carlo and K-S analyses were able to identify the parameters chiefly responsible for simulation accuracy and those which made comparatively smaller contributions. By considering

the inclusion or exclusion of possible mechanisms, each of the constructed models was simple and computationally efficient yet met the needs of the analysis. The benefit of such models extended beyond calibration efforts and grants the ability to relatively inexpensively explore a large spectrum of parameter ranges and derive broader learnings from their results. The inexpensive nature of calibration efforts using these tools potentially warrants their use to complement `MODFLOW/MT3D` and `FEFLOW` modelling efforts with site-specific parameter values from physical tests, instead of literature-based assumptions.

It is hoped that the open-loop GSHS industry will benefit from the insights presented in this thesis. Open-loop GSHS shows amazing potential for sustainable and environmentally responsible provision of home, building and regional heating and cooling needs — a necessity for the journey away from fossil-fuel dependency.

6.2 Future Work

The studies presented here have highlighted areas for continued research which would contribute toward greater understanding in the open-loop GSHS field. Several examples are:

1. Calibrating the thermal properties of RFH through its operational data remains of interest but requires the acquisition of additional data to allow potential progress. In order to assess the likelihood that regional temperature fluctuations are responsible for the observed abstraction well temperatures, historical regional temperature data is required. Environment Agency (2018) demonstrates the presence of temperature monitoring within the EC aquifer, but the existence and dependability of data in proximity of RFH is not known. The physical distributions of horizontal flow and vertical temperature gradients within the EC aquifer at RFH are not known and have not been investigated. A down-hole flowmeter, geophysical, and temperature investigation under pumping and non-pumping conditions is expected to yield insight into the distribution of flow and temperature heterogeneity, as well as the physical

domain (e.g., fracture frequency and cross-well fracture persistence). This information would greatly assist constraining investigative models. So too would increased thermal instrumentation and any possible further monitoring of the regional groundwater temperatures. Effectively constraining and understanding one EC-based open-loop GSHS could provide critical understanding for other systems (both present, pending and future).

2. The application of the DF flow regime to the characterisation of well and aquifer-based parameters implicitly associates head-loss with the aquifer rather than with the well. The evolution of the drawdown curve, subject to a given flowrate, is a direct consequence of the pressure profile throughout the aquifer and as such of both permeability and storativity. Traditionally, head-loss is attributed to both the well and the aquifer, resulting in an inability to independently calibrate the storativity of the aquifer without the use of an observation/monitoring well to constraint the physical problem (Jacob, 1947; Clark, 1977). However, the DF approach does not hold this limitation, and sensitivity analyses in this thesis suggested parameter uniqueness without an observation well. It is of keen interest to the author to apply the DF approach to several pump testing data sets which obtain distinct drawdown behaviour in an observation well, addressing whether the explicit determination of storativity remains restricted in said approach, and whether DF-based calibrations remain indifferent with the additional constraint.

3. The three fundamental domains of study within this thesis (hydraulic, solute and thermal) could yield additional learnings through the application of dimensionless analysis. Preliminary dimensionless analysis was conducted on each at varying points throughout work on the dissertation. However, the key output motivating analyses was dimensional (drawdown and breakthrough quantities) and therefore presented difficulties in associating and communicating dimensionless-based learnings. Dimensionless analysis of pump tests and solute breakthrough curves have been studied widely, but the thermal

evolution of systems under differing operation strategies (unidirectional and seasonally reversed) has not. This is a future research area of keen interest to the author.

4. Several additional open-loop GSHS research interests exist; research into 'thermally responsive' operational strategies, performance of seasonal system under varying parameter scales, thermal recovery rates of reversed systems, critical system density for given domain sizes, and the time-scale significance of 3D diffusion.

References

Abesser, C (2010). "Open-loop ground source heat pumps and groundwater systems: A literature review of current applications, regulations and problems". *British Geological Survey, Report, OR/10/045*.

— (2012). "Technical Guide - A screening tool for open-loop ground source heat pump schemes (England and Wales)". *British Geological Survey, Report, OR/12/060*.

Abesser, C, M Lewis, A Marchant, and A Hulbert (2014). "Mapping suitability for open-loop ground source heat pump systems: a screening tool for England and Wales, UK". *Quarterly Journal of Engineering Geology and Hydrogeology* Vol. 47.4, pp. 373–380.

Abesser, C, R.A. Schincariol, J Raymond, A Garcıéa-Gil, R Drysdale, A Piatek, N Giordano, Nand Jaziri, and J Molson (2021). "Case studies of geothermal system response to perturbations in groundwater flow and thermal regimes". *Groundwater*.

Abesser, C, D Schofield, H Bonsor, and R Ward (2018). "Who owns (geothermal) heat?" *British Geological Survey, Science Briefing Paper*.

Adams, M, J Beall, S Enedy, P Hirtz, P Kilbourn, B Koenig, R Kunzman, and J Smith (2001). "Hydrofluorocarbons as geothermal vapor-phase tracers". *Geothermics* Vol. 30.6, pp. 747–775.

Adams, M and J Davis (1991). "Kinetics of fluorescein decay and its application as a geothermal tracer". *Geothermics* Vol. 20.1-2, pp. 53–66.

Allen, D, L Brewerton, L Coleby, B Gibbs, M Lewis, A MacDonald, S Wagstaff, and A Williams (1997). "The physical properties of major aquifers in England and Wales". *Quarterly Journal of Engineering Geology and Hydrogeology*.

Ampofo, F, G Maidment, and J Missenden (2006a). "Groundwater cooling systems in London". *International Journal of Low-Carbon Technologies* Vol. 1.4, pp. 336–342.

— (2006b). "Review of groundwater cooling systems in London". *Applied Thermal Engineering* Vol. 26.17-18, pp. 2055–2062.

Andersson, O (1998). "Heat pump supported ATES applications in Sweden". *IEA Heat Pump Center Newsletter* Vol. 16.

— (2007). "Aquifer thermal energy storage (ATES)". In: *Thermal energy storage for sustainable Energy Consumption*. Springer, pp. 155–176.

Arthur, S, H Streetly, S Valley, M Streetly, and A Herbert (2010). "Modelling large ground source cooling systems in the chalk aquifer of central London". *Quarterly Journal of Engineering Geology and Hydrogeology* Vol. 43.3, pp. 289–306.

Arthur, S. and H. Streetly (2009). "Modelling of groundwater cooling schemes in London". In: *International FEFLOW conference*.

Atkinson, T, R Ward, E O'Hannelly, and A Dassargues (2000). "Radial-flow tracer test in Chalk: comparison of models and fitted parameters". *IAHS Publication(International Association of Hydrological Sciences)* 262, pp. 7–15.

Axelsson, G, G Bjornsson, and F Montalvo (2005). "Quantitative interpretation of tracer test data". In: *Proceedings world geothermal Congress*, pp. 24–29.

Bakema, G and A Snijders (1998). "ATES and ground-source heat pumps in the Netherlands". *IEA Heat Pump Center Newsletter* Vol. 16.

Bandai, T, S Hamamoto, G Rau, T Komatsu, and T Nishimura (2017). "The effect of particle size on thermal and solute dispersion in saturated porous media". *International Journal of Thermal Sciences* Vol. 122, pp. 74–84.

Banks, D (2009a). "An introduction to 'thermogeology' and the exploitation of ground source heat". *Quarterly Journal of Engineering Geology and Hydrogeology* Vol. 42.3, pp. 283–293.

— (2009b). "Thermogeological assessment of open-loop well-doublet schemes: a review and synthesis of analytical approaches". *Hydrogeology Journal* Vol. 17.5, pp. 1149–1155.

— (2011a). "Site investigation (ground conditions/licences and permits)". *Geotrainet 2011 Geotrainet Training Manual for Designers of Shallow Geothermal Systems*, pp. 71–92.

— (2011b). "The application of analytical solutions to the thermal plume from a well doublet ground source heating or cooling scheme". *Quarterly Journal of Engineering Geology and Hydrogeology* Vol. 44.2, pp. 191–197.

Barker, J (1985). "Block-geometry functions characterizing transport in densely fissured media". *Journal of Hydrology* Vol. 77.1-4, pp. 263–279.

Barker, J et al. (1985). "Modelling the effects of matrix diffusion on transport in densly fissured media". In: *Congress of the International Association of Hydrogeologists, 18.* IAH, pp. 250–69.

Barker, J (1991). "Transport in fractured rock". In: *Applied groundwater hydrology. A British perspective*, pp. 199–216.

— (1993). "Modelling groundwater flow and transport in the Chalk".

— (2010). "Modelling doublets and double porosity". *Quarterly Journal of Engineering Geology and Hydrogeology* Vol. 43.3, pp. 259–268.

— (2012). "Discussion on 'The application of analytical solutions to the thermal plume from a well doublet ground source heating/cooling scheme'Quarterly Journal of Engineering Geology and Hydrogeology Vol. 44, 191–197". *Quarterly Journal of Engineering Geology and Hydrogeology* Vol. 45.1, pp. 123–123.

Barker, J, R Downing, and D Gray (1986). "Modelling of low enthalpy geothermal schemes". *Geothermal Energy: The Potential in the UK. HMSO, London* Vol. 111, p. 123.

Barker, J and R Herbert (1992). "A simple theory for estimating well losses: with application to test wells in Bangladesh". *Applied Hydrogeology*, pp. 20–31.

Bear, J (1961). "On the tensor form of dispersion in porous media". *Journal of Geophysical Research* Vol. 66.4, pp. 1185–1197.

Bear, J, C Tsang, and G De Marsily (2012). *Flow and contaminant transport in fractured rock*. Academic Press.

Beirschenk, W and G Wilson (1961). "The exploration and development of ground-water resources in Iran". In: *Symposium of Athens: Groundwater in arid zones.* Vol. Vol. 2. Internat. Assoc. Sci.Hydrology, p. 607.

Bell, F (1977). "A note on the physical properties of the chalk". *Engineering Geology* Vol. 11.3, pp. 217–225.

BenBarka, A (1982). "Aspects of aquifer test error analysis".

Berry, F (1979). "Late Quaternary scour-hollows and related features in central London". *Quarterly Journal of Engineering Geology and Hydrogeology* Vol. 12.1, pp. 9–29.

Bevan, T and P Hancock (1986). "A late Cenozoic regional mesofracture system in southern England and northern France". *Journal of the Geological Society* Vol. 143.2, pp. 355–362.

Beven, K and A Binley (1992). "The future of distributed models: model calibration and uncertainty prediction". *Hydrological processes* Vol. 6.3, pp. 279–298.

Bibby, R (1977). "Characteristics of pumping tests in heterogeneous clastic sediments, Edmonton, Alberta". *Alberta Research Council Bulletin* Vol. 35, pp. 31–39.

— (1979). *Estimating sustainable yield to a well in heterogeneous strata.* Vol. Vol. 37. Alberta Research Council.

Bierschenk, W (1963). *Determining well efficiency by multiple step-drawdown tests.* International Association of Scientific Hydrology.

Birks, D (2019). "Groundwater heating and cooling-an evaluation of resilience in the context of recharge and temperature". PhD thesis. University of Glasgow.

Birks, D, C Adamson, M Woods, and G Holmes (2022). "Evaluation of measures to improve the performance of an open loop ground source heat pump system in the chalk aquifer: a case study". *Quarterly Journal of Engineering Geology and Hydrogeology* Vol. 55.2.

Birks, D, C Coutts, P Younger, and G Parkin (2015a). "Development of a groundwater heating and cooling scheme in a Permo-Triassic sandstone aquifer in South-West England and approach to managing risks". *Geoscience in South-West England* Vol. 13.4, pp. 428–436.

Birks, D, P Younger, L Tavendale, C Coutts, G Parkin, P Button, and S Whittall (2015b). "Groundwater reinjection and heat dissipation: lessons from the operation of a large groundwater cooling system in Central London". In: Geological Society of London.

Bloomfield, J (1996). "Characterisation of hydrogeologically significant fracture distributions in the chalk: an example from the Upper Chalk of southern England". *Journal of hydrology* Vol. 184.3-4, pp. 355–379.

Boon, D, A Butcher, B Townsend, and M Woods (2020). "Geological and Hydrogeological Investigations in the Colchester Northern Gateway Boreholes: February 2020 survey". *BGS Open Technical Report.*

Boon, D, G Farr, C Abesser, A Patton, D James, D Schofield, and D Tucker (2019). "Groundwater heat pump feasibility in shallow urban aquifers: experience from Cardiff, UK". *Science of the Total Environment* Vol. 697.

Bristow, R, R Mortimore, and C Wood (1997). "Lithostratigraphy for mapping the Chalk of southern England". *Proceedings of the Geologists' Association* Vol. 108.4, pp. 293–315.

BSI (2003). *BS ISO 14686: 2003: Hydrometric determinations. Pumping tests for water wells. Considerations and guidelines for design, performance and use.*

— (2012). *BS EN ISO 22282-4: 2012: Geotechnical investigation and testing. Geohydraulic testing. Pumping tests.*

Busby, John (2015). "UK shallow ground temperatures for ground coupled heat exchangers". *Quarterly Journal of Engineering Geology and Hydrogeology* Vol. 48.3, pp. 248–260.

— (2018). "A modelling study of the variation of thermal conductivity of the English Chalk". *Quarterly Journal of Engineering Geology and Hydrogeology* Vol. 51.4, pp. 417–423.

Busby, John, M Lewis, H Reeves, and R Lawley (2009). "Initial geological considerations before installing ground source heat pump systems". *Quarterly Journal of Engineering Geology and Hydrogeology* Vol. 42.3, pp. 295–306.

Butler, A, S Mathias, A Gallagher, D Peach, and A Williams (2009). "Analysis of flow processes in fractured chalk under pumped and ambient conditions (UK)". *Hydrogeology Journal* Vol. 17.8, pp. 1849–1858.

Casalini, T, M Salvalaglio, G Perale, M Masi, and C Cavallotti (2011). "Diffusion and aggregation of sodium fluorescein in aqueous solutions". *The Journal of Physical Chemistry B* Vol. 115.44.

Casasso, A and R Sethi (2015). "Modelling thermal recycling occurring in groundwater heat pumps (GWHPs)". *Renewable Energy* Vol. 77, pp. 86–93.

Clark, L (1977). "The analysis and planning of step drawdown tests". *Quarterly Journal of Engineering Geology and Hydrogeology* Vol. 10.2, pp. 125–143.

Clarkson, M, D Birks, P Younger, A Carter, and S Cone (2009). "Groundwater cooling at the Royal Festival Hall, London". *Quarterly Journal of Engineering Geology and Hydrogeology* Vol. 42.3, pp. 335–346.

Clyde, C and G Madabhushi (1983). "Spacing of wells for heat pumps". *Journal of Water Resources Planning and Management* Vol. 109.3, pp. 203–212.

Cooper, A, A Farrant, and S Price (2011). "The use of karst geomorphology for planning, hazard avoidance and development in Great Britain". *Geomorphology* Vol. 134.1-2, pp. 118–131.

Cooper Jr, H and C Jacob (1946). "A generalized graphical method for evaluating formation constants and summarizing well-field history". *Eos, Transactions American Geophysical Union* Vol. 27.4, pp. 526–534.

Da Costa, J and R Bennett (1960). "The pattern of flow in the vicinity of a recharging and discharging pair of wells in an aquifer having areal parallel flow". *Internat. Association of Scientific Hydrology. IUGG General Assembly of Helsinki* 52, pp. 524–536.

Data.org (2022). *Data.org*. URL: `https://en.climate-data.org/europe/united-kingdom/england/london-1/#temperature-graph`.

De Jong, G and M Bossen (1961). "Discussion of paper by Jacob Bear,"On the tensor form of dispersion in porous media"". *Journal of Geophysical Research* Vol. 66.10, pp. 3623–3624.

Dickinson, JS, N Buik, MC Matthews, and A Snijders (2009). "Aquifer thermal energy storage: theoretical and operational analysis". *Geotechnique* Vol. 59.3, pp. 249–260.

Dickson, M and M Fanelli (2013). *Geothermal energy: utilization and technology*. Routledge.

Dietrich, P, R Helmig, M Sauter, H Hotzl, J Kongeter, and G Teutsch (2005). *Flow and transport in fractured porous media*. Springer.

Domenico, P, F Schwartz, et al. (1998). *Physical and chemical hydrogeology*. Vol. Vol. 506. Wiley New York.

Eden, R and C Hazel (1973). *Computer and graphical analysis of variable discharge pumping tests of wells*. Institution of Engineers Australia.

Ellison, R, M Woods, D Allen, A Forster, T Pharaoh, and C King (2004). *Geology of London: special memoir for 1: 50000 geological sheets 256 (north London), 257 (Romford), 270 (south London), and 271 (Dartford)(England and Wales)*. British Geological Survey.

Entwisle, D, P Hobbs, K Northmore, J Skipper, M Raines, S Self, R Ellison, and L Jones (2013). "Engineering geology of British rocks and soils: Lambeth Group". *Engineering Geology Directorate*.

Environment Agency (2005). *Chalk groundwater licensing policy for London*.

— (2011). *Environmental Good Practice Guide for Ground Source Heating and Cooling*.

— (2018). *London Basin Chalk Aquifer Annual Status Report, 2018*.

Fick, A (1855). "Ueber diffusion". *Annalen der Physik* Vol. 170.1, pp. 59–86.

Forchheimer, P (1901). "Wasserbewegung durch Boden". *Z. Ver. Deutsch, Ing.* Vol. 45.17, pp. 82–88.

Foster, S (1975). "The Chalk groundwater tritium anomaly—a possible explanation". *Journal of Hydrology* Vol. 25.1-2, pp. 159–165.

Foster, S and V Milton (1974). "The permeability and storage of an unconfined Chalk aquifer".

— (1976). *Hydrological basis for large-scale development of groundwater storage capacity in the East Yorkshire Chalk*. HM Stationery Office.

Freeze, R and J Cherry (1979). *Groundwater*. Prentice-Hall.

Fry, V (2009). "Lessons from London: regulation of open-loop ground source heat pumps in central London". *Quarterly Journal of Engineering Geology and Hydrogeology* Vol. 42.3, pp. 325–334.

Gale, I, A Williams, and M Mansour (2006). "Royal Festival Hall - An assessment of the impacts of recharging the Chalk aquifer". *BGS Technical Report*.

Garcia-Gil, A, G Goetzl, M Klonowski, S Borovic, D Boon, C Abesser, M Janza, I Herms, E Petitclerc, M Erlstrom, et al. (2020). "Governance of shallow geothermal energy resources". *Energy Policy* Vol. 138.

Gelhar, L (1993). *Stochastic subsurface hydrology*. Prentice-Hall.

Gropius, M (2010). "Numerical groundwater flow and heat transport modelling of open-loop ground source heat systems in the London Chalk". *Quarterly Journal of Engineering Geology and Hydrogeology* Vol. 43.1, pp. 23–32.

Grove, D and W Beetem (1971). "Porosity and dispersion constant calculations for a fractured carbonate aquifer using the two well tracer method". *Water Resources Research* Vol. 7.1, pp. 128–134.

Grove, D, W Beetem, and F Sower (1970). "Fluid travel time between a recharging and discharging well pair in an aquifer having a uniform regional flow field". *Water Resources Research* Vol. 6.5, pp. 1404–1410.

Hacker, J and M Holmes (2007). "Thermal comfort: climate change and the environmental design of buildings in the United Kingdom". *Built Environment* Vol. 33.1, pp. 97–114.

Hancock, J (1975). "The petrology of the Chalk". *Proceedings of the Geologists' Association* Vol. 86.4, pp. 499–535.

Hazel, C (1973). "Lecture notes: Groundwater Hydraulics". In: Australian Water Resources Council. Groundwater school Adelaide. Unpublished.

Headon, J, D Banks, A Waters, and VK Robinson (2009). "Regional distribution of ground temperature in the Chalk aquifer of London, UK". *Quarterly Journal of Engineering Geology and Hydrogeology* Vol. 42.3, pp. 313–323.

Helweg, O (1994). "A general solution to the step-drawdown test". *Groundwater* Vol. 32.3, pp. 363–366.

Herbert, A, S Arthur, and G Chillingworth (2013). "Thermal modelling of large scale exploitation of ground source energy in urban aquifers as a resource management tool". *Applied Energy* Vol. 109, pp. 94–103.

Hight, D, R Ellison, D Page, Construction Industry Research, Information Association Staff, Great Britain. Department of Trade, Industry, Construction Industry Research, and Information Association (2004). *Engineering in the Lambeth Group*. CIRIA Series. CIRIA. URL: https://books.google.co.uk/books?id=vwraAAAACAAJ.

Hight, D, F McMillan, J Powell, R Jardine, and C Allenou (2003). "Some characteristics of London clay". *Characterisation and engineering properties of natural soils* Vol. 2, pp. 851–946.

Hoopes, J and D Harleman (1965). "Wastewater recharge and dispersion in porous media". *Journal of the Hydraulics Division* Vol. 93.5, pp. 51–72.

Houben, G (2015). "Hydraulics of water wells—head losses of individual components". *Hydrogeology journal* Vol. 23.8, pp. 1659–1675.

Houben, G and C Treskatis (2007). *Water well rehabilitation and reconstruction*. McGraw-Hill.

Hutchinson, J (1980). "Possible late Quaternary pingo remnants in central London". *Nature* Vol. 284.5753, p. 253.

Jacob, C (1947). "Drawdown Test to Determine the Effective Radius of an Artesian Well, Trans". In: *ASCE*. Vol. Vol. 112, pp. 1047–1070.

Jenkins, L (2019). "Fluid injection and migration in layered aquifers". PhD thesis. University of Oxford.

Jones, H, B Morris, C Cheney, L Brewerton, P Merrin, M Lewis, A MacDonald, L Coleby, J Talbot, A McKenzie, et al. (2000). *The physical properties of minor aquifers in England and Wales*.

Klavan, S (2019). "Melody and meaning: the semiotics of ancient Greek music in the late classical and early Hellenistic eras". PhD thesis. University of Oxford.

Kohl, T, K Evans, R Hopkirk, R Jung, and L Rybach (1997). "Observation and simulation of non-Darcian flow transients in fractured rock". *Water Resources Research* Vol. 33.3, pp. 407–418.

Kolditz, O (2001). "Non-linear flow in fractured rock". *International Journal of Numerical Methods for Heat & Fluid Flow*.

Kruseman, G, N De Ridder, and J Verweij (1970). *Analysis and evaluation of pumping test data*. Vol. Vol. 11. International institute for land reclamation and improvement The Netherlands.

La Bernardie, J de, O Bour, T Le Borgne, N Guiheneuf, E Chatton, T Labasque, H Le Lay, and M Gerard (2018). "Thermal attenuation and lag time in fractured rock: Theory and field measurements from joint heat and solute tracer tests". *Water Resources Research* Vol. 54.12, pp. 10–53.

Law, R (2010). "Geothermal systems in the Chalk of the south east of England: methods of predicting thermal transport in a fractured aquifer". PhD thesis. University of Birmingham.

Law, R and R Mackay (2010). "Determining fracture properties by tracer and thermal testing to assess thermal breakthrough risks for ground source heating and cooling in the chalk". *Quarterly Journal of Engineering Geology and Hydrogeology* Vol. 43.3, pp. 269–278.

Law, R, D Nicholson, K Mayo, and Arup Geotechnics (2007). "Aquifer thermal energy storage in the fractured London Chalk. A thermal injection/withdrawal test and its interpretation". In: *Proceedings of the 32nd Workshop on Geothermal Reservoir Engineering*.

Le Brun, M, V Hamm, S Lopez, P Ungemach, M Antics, J Ausseur, E Cordier, E Giuglaris, P Goblet, and P Lalos (2011). "Hydraulic and thermal impact modelling at the scale of the geothermal heating doublet in the Paris Basin, France". In: *Proceedings of the 36 Workshop on Geothermal Reservoir Engineer*.

Le Feuvre, P (2007). "An investigation into ground source heat pump technology, its UK market and best practice in system design". *Mechanical Engineering, University of Strathclyde. MSc* Vol. 180.

Lexicon, BGS (n.d.). *The BGS Lexicon of Named Rock Units*. URL: `https://www.bgs.ac.uk/Lexicon/`.

Lippmann, M (1980). "Ground water use for cooling: Associated aquifer temperature changes".

Ltd, Minerva (Holland Park) (2015). *The Kensington, 263 Kensington High Street: 9.18 Subterranean Construction Method Statement*.

Luo, J, M Dentz, O Cirpka, and P Kitanidis (2007). "Breakthrough curve tailing in a dipole flow field". *Water Resources Research* Vol. 43.9.

Luo, J and P Kitanidis (2004). "Fluid residence times within a recirculation zone created by an extraction–injection well pair". *Journal of Hydrology* Vol. 295.1-4, pp. 149–162.

Luo, J, J Rohn, W Xiang, D Bertermann, and P Blum (2016). "A review of ground investigations for ground source heat pump (GSHP) systems". *Energy and Buildings* Vol. 117, pp. 160–175.

MacDonald, A and D Allen (2001). "Aquifer properties of the Chalk of England". *Quarterly Journal of Engineering Geology and Hydrogeology* Vol. 34.4, pp. 371–384.

Mathias, S, A Butler, T Atkinson, S Kachi, and R Ward (2006). "A parameter identifiability study of two chalk tracer tests". *Hydrology and Earth System Sciences Discussions* Vol. 3.4, pp. 2437–2471.

— (2009). "A parameter sensitivity analysis of two Chalk tracer tests". *Quarterly Journal of Engineering Geology and Hydrogeology* Vol. 42.2, pp. 237–244.

Mathias, S, A Butler, and H Zhan (2008). "Approximate solutions for Forchheimer flow to a well". *Journal of Hydraulic Engineering* Vol. 134.9, pp. 1318–1325.

Mathias, S, S Reaney, and P Kenabatho (2021). "Transmission loss estimation for ephemeral sand rivers in Southern Africa". *Journal of Hydrology* Vol. 600.

Mathias, S and L Todman (2010). "Step-drawdown tests and the Forchheimer equation". *Water Resources Research* Vol. 46.7.

Maurice, L, T Atkinson, J Barker, J Bloomfield, A Farrant, and A Williams (2006). "Karstic behaviour of groundwater in the English Chalk". *Journal of Hydrology* Vol. 330.1-2, pp. 63–70.

Maurice, L, J Barker, T Atkinson, A Williams, and P Smart (2011). "A tracer methodology for identifying ambient flows in boreholes". *Groundwater* Vol. 49.2, pp. 227–238.

Mazumder, Sandip (2015). *Numerical methods for partial differential equations: finite difference and finite volume methods*. Academic Press.

Menkiti, C, J Davis, K Semertzidou, C Abbireddy, D Hight, J Williams, and M Black (2015a). "The geology and geotechnical properties of the Thanet Sand Formation – an update from the Crossrail Project". In:

Menkiti, C, J Davis, K Semertzidou, C Abbireddy, D Hight, J Williams, and M Black (2015b). "The geology and geotechnical properties of the Thanet Sand Formation–an update from the Crossrail Project". *Crossrail Project: Infrastructure design and construction*, pp. 63–77.

Milnes, E and P Perrochet (2013). "Assessing the impact of thermal feedback and recycling in open-loop groundwater heat pump (GWHP) systems: a complementary design tool". *Hydrogeology journal* Vol. 21.2, pp. 505–514.

Molz, F, J Melville, A Parr, D King, and M Hopf (1983). "Aquifer thermal energy storage: a well doublet experiment at increased temperatures". *Water Resources Research* Vol. 19.1, pp. 149–160.

Monaghan, A, V Starcher, H Barron, K Shorter, K Walker-Verkuil, J Elsome, T Kearsey, S Arkley, S Hannis, and E Callaghan (2022). "Drilling into mines for heat: geological synthesis of the UK Geoenergy Observatory in Glasgow and implications for mine water heat resources". *Quarterly Journal of Engineering Geology and Hydrogeology* Vol. 55.1.

Mortimore, R, T Newman, K Royse, H Scholes, and U Lawrence (2011). "Chalk: its stratigraphy, structure and engineering geology in east London and the Thames Gateway". *Quarterly Journal of Engineering Geology and Hydrogeology* Vol. 44.4, pp. 419–444.

Mortimore, R and B Pomerol (1997). "Upper Cretaceous tectonic phases and end Cretaceous inversion in the Chalk of the Anglo-Paris Basin". *Proceedings of the geologists' association* Vol. 108.3, pp. 231–255.

Muskat, M (1938). "The flow of homogeneous fluids through porous media". *Soil Science* Vol. 46.2, p. 169.

Nield, D, A Bejan, et al. (2006). *Convection in porous media*. Vol. Vol. 3. Springer.

Odling, N, L West, S Hartmann, and A Kilpatrick (2013). "Fractional flow in fractured chalk; a flow and tracer test revisited". *Journal of contaminant hydrology* Vol. 147, pp. 96–111.

Osiensky, J, R Williams, B Williams, and G Johnson (2000). "Evaluation of drawdown curves derived from multiple well aquifer tests in heterogeneous environments". *Mine Water and the Environment* Vol. 19.1, pp. 30–55.

Papadopulos, I and H Cooper Jr (1967). "Drawdown in a well of large diameter". *Water Resources Research* Vol. 3.1, pp. 241–244.

Park, B, G Bae, and K Lee (2015). "Importance of thermal dispersivity in designing groundwater heat pump (GWHP) system: Field and numerical study". *Renewable Energy* Vol. 83, pp. 270–279.

Patsoules, M and J Cripps (1990). "5 Survey of macro and micro-fracturing in Yorkshire chalk". In: *Chalk*. Thomas Telford Publishing, pp. 87–93.

Paul, S (1993). "Ground Water Issue: Suggested Operating Procedures for Aquifer Pumping Tests". *United States Environmental Protection Agency*.

Piga, B, A Casasso, F Pace, A Godio, and R Sethi (2017). "Thermal impact assessment of groundwater heat pumps (GWHPs): Rigorous vs. simplified models". *Energies* Vol. 10.9.

Pollack, H, S Hurter, and J Johnson (1993). "Heat flow from the Earth's interior: analysis of the global data set". *Reviews of Geophysics* Vol. 31.3, pp. 267–280.

Price, M (1987). "Fluid flow in the Chalk of England". *Geological Society, London, Special Publications* Vol. 34.1, pp. 141–156.

Price, M, M Bird, and S Foster (1976). "Chalk pore-size measurements and their significance". *Water Services* Vol. 80.968, pp. 596–600.

Price, M, R Downing, and W Edmunds (1993). "The Chalk as an aquifer". *The hydrogeology of the Chalk of north-west Europe*, pp. 35–58.

Rau, G, M Andersen, and R Acworth (2012). "Experimental investigation of the thermal dispersivity term and its significance in the heat transport equation for flow in sediments". *Water Resources Research* Vol. 48.3.

Rees, D, A Bassom, and P Siddheshwar (2008). "Local thermal non-equilibrium effects arising from the injection of a hot fluid into a porous medium". *Journal of Fluid Mechanics* Vol. 594, pp. 379–398.

Reeves, M (1979). "Recharge and pollution of the English Chalk: some possible mechanisms". *Engineering Geology* Vol. 14.4, pp. 231–240.

Renard, P, D Glenz, and M Mejias (2009). "Understanding diagnostic plots for well-test interpretation". *Hydrogeology Journal* Vol. 17.3, pp. 589–600.

Rorabaugh, M (1953). "Graphical and theoretical analysis of step-drawdown test of artesian well". In: *Proceedings of the American Society of Civil Engineers*. Vol. Vol. 79. 12. ASCE, pp. 1–23.

Royse, K, M de Freitas, W Burgess, J Cosgrove, R Ghail, P Gibbard, C King, U Lawrence, R Mortimore, H Owen, et al. (2012). "Geology of London, UK". *Proceedings of the Geologists' Association* Vol. 123.1, pp. 22–45.

Scheidegger, A (1961). "General theory of dispersion in porous media". *Journal of Geophysical Research* Vol. 66.10, pp. 3273–3278.

Semiond, H and F Gonzalez (2005). *Water, Sanitation and Hygiene for Populations at Risk*.

Şen, Z (1988). "Analytical solution incorporating nonlinear radial flow in confined aquifers". *Water Resources Research* Vol. 24.4, pp. 601–606.

Shampine, L and M Reichelt (1997). "The matlab ode suite". *SIAM journal on scientific computing* Vol. 18, pp. 1–22.

Sherlock, R (1935). *British Regional Geology: London and Thames Valley*. HMSO.

Shook, G, S Ansley, and A Wylie (2004). *Tracers and tracer testing: design, implementation, and interpretation methods*. Citeseer.

Snijders, A and B Drijver (2016). "Open-loop heat pump and thermal energy storage systems". In: *Advances in ground-source heat pump systems*. Elsevier, pp. 247–268.

Snow, D (1968). "Rock fracture spacings, openings, and porosities". *Journal of Soil Mechanics & Foundations Div.*

Soley, R, T Power, R Mortimore, P Shaw, J Dottridge, G Bryan, and I Colley (2012). "Modelling the hydrogeology and managed aquifer system of the chalk across southern England". *Geological Society, London, Special Publications* Vol. 364.1, pp. 129–154.

Streltsova, T (1987). *Well testing in heterogeneous formations*. John Wiley and Sons Inc., New York, NY.

Sumbler, M (1996). "London and the Thames Valley, British regional geology series". *British Geological Survey*.

Tang, D and S van der Zee (2021). "Dispersion and recovery of solutes and heat under cyclic radial advection". *Journal of Hydrology* Vol. 602.

Theis, C (1935). "The relation between the lowering of the piezometric surface and the rate and duration of discharge of a well using ground-water storage". *Eos, Transactions American Geophysical Union* Vol. 16, pp. 519–524.

Thiem, G (1906). *Hydrologische Methoden: Dissertation zur Erlangung der Wurde eines...* JM Gebhardt.

Toth, J (1966). *Groundwater geology, movement, chemistry, and resources near Olds, Alberta*. Research Council of Alberta.

Upton, K, A Butler, C Jackson, and M Mansour (2019). "Modelling boreholes in complex heterogeneous aquifers". *Environmental Modelling & Software* Vol. 118, pp. 48–60.

Van Tonder, G, J Botha, and J Van Bosch (2001). "A generalised solution for step-drawdown tests including flow dimension and elasticity". *Water S.A* Vol. 27.3, pp. 345–354.

Ventouras, K (2005). "Engineering behaviour of Thanet sand". PhD thesis. Imperial College London (University of London).

Vos, L (2007). "Underground thermal energy storage in the Netherlands". *Groundwater: Opportunities and Pressures*.

Vourvoulias, A (2022). *Open loop ground source heat pumps*. URL: `https://www.greenmatch.co.uk/heat-pump/ground-source-heat-pumps-in-the-uk/open-loop-ground-source-heat-pumps`.

Wang, X, L He, X Zhao, and N Yu (2015). *Application of Geophysical Methods to the Geothermal Investigation*.

Ward, R, A Williams, and J Barker (1998). *Groundwater tracer tests: a review and guidelines for their use in British aquifers*. Environment Agency.

Wilson, E (1990). *Engineering hydrology*. Macmillan International Higher Education.

Yedidiah, S (2012). *Centrifugal pump user's guidebook: problems and solutions*. Springer Science & Business Media.

Younger, P (1989). "Devensian periglacial influences on the development of spatially variable permeability in the Chalk of southeast England". *Quarterly Journal of Engineering Geology and Hydrogeology* Vol. 22.4, pp. 343–354.

— (2008). "Ground-coupled heating-cooling systems in urban areas: how sustainable are they?" *Bulletin of Science, Technology & Society* Vol. 28.2, pp. 174–182.

Younger, P and T Elliot (1995). "Chalk fracture system characteristics: implications for flow and solute transport". *Quarterly Journal of Engineering Geology and Hydrogeology* Vol. 28.1, S39–S50.

Zhou, Q, C Oldenburg, and J Rutqvist (2019). "Revisiting the analytical solutions of heat transport in fractured reservoirs using a generalized multirate memory function". *Water Resources Research* Vol. 55.2, pp. 1405–1428.

Appendices

A

Finite Volume Methods

Throughout this thesis, a finite volume method (FVM) is adopted to discretise in space. An FVM is used to ensure the governing PDEs are satisfied over discrete control volumes, which may or may not be uniformly spaced (Mazumder, 2015). FVMs are popular for flow problems (such as here) as they are inherently flux conservative, unlike finite difference methods. Jenkins (2019) provides a concise summary of the FVM in 1D. We extend this work to acknowledge its application to 2D.

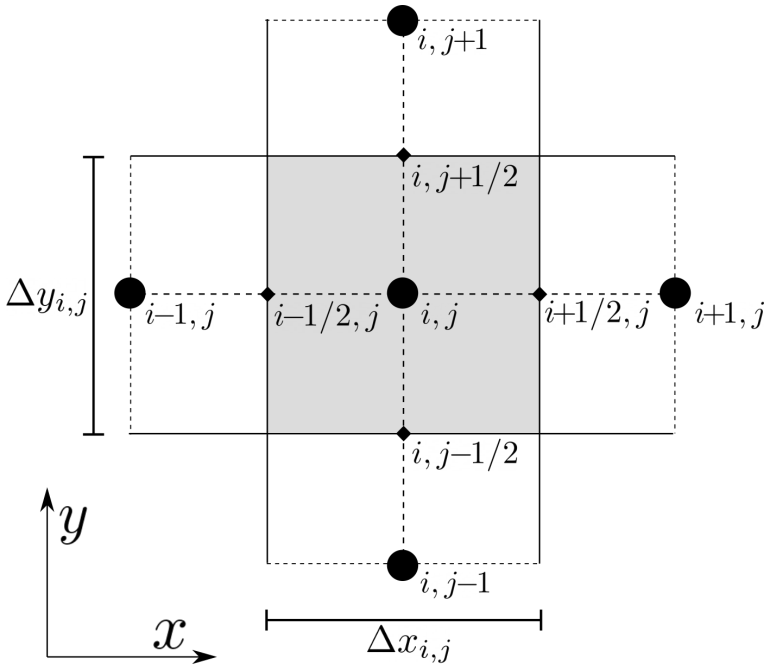

Figure A.1: Uniform 2D finite volume grid where cell centres are located on integer indicies, and cell interfaces/edges are positioned evenly between centers (e.g., i–1/2 and i+1/2).

We apply FVM in both 1D and 2D, to solve the integral form of

$$\frac{\partial M}{\partial t} + \frac{\partial F}{\partial x} + \frac{\partial F}{\partial y} = 0 \tag{A.1}$$

where F is a flux term and M is the quantity being conserved (e.g., mass, energy). Neglecting source and sink terms (e.g., abstraction and injection terms associated with wells), the governing 1D and 2D PDEs of this thesis can be written in this Cartesian formulation.

We define a staggered grid such that the nominal *grid cell* i, j is bounded by *cell interfaces* i–$1/2, j$, i+$1/2, j$, i, j–$1/2$ and i, j+$1/2$. The distance between cell edges is the cell width, defined as $\Delta x_{i,j} \equiv x_{i+1/2,j} - x_{i-1/2,j}$ and $\Delta y_{i,j} \equiv y_{i,j+1/2} - y_{i,j-1/2}$ (see Figure A.1). For a nominal time t_n, the average quantity in the i^{th}, j^{th} cell is given by

$$\langle M(x, y, t_n) \rangle = \frac{1}{\Delta x_{i,j} \Delta y_{i,j}} \int_{x_{i+1/2,j}}^{x_{i-1/2,j}} \int_{y_{i,j+1/2}}^{y_{i,j-1/2}} M(x, y, t_n) dx dy. \tag{A.2}$$

Similarly, at time $t = t_{n+1}$ the average quantity in the i^{th}, j^{th} cell is given by

$$\langle M(x, y, t_{n+1}) \rangle = \frac{1}{\Delta x_{i,j} \Delta y_{i,j}} \int_{x_{i-1/2,j}}^{x_{i+1/2,j}} \int_{y_{i,j-1/2}}^{y_{i,j+1/2}} M(x, y, t_{n+1}) dx dy \tag{A.3}$$

Integrating Eq.(A.1) with respect to time and arranging for $M(x, y, t_{n+1})$ gives

$$M(x, y, t_{n+1}) = M(x, y, t_n) - \int_{t_{n+1}}^{t_n} \frac{\partial F}{\partial x} dt - \int_{t_{n+1}}^{t_n} \frac{\partial F}{\partial y} dt \tag{A.4}$$

Substituting Eq.(A.4) into Eq.(A.3) gives an expression for the average quantity at t_{n+1} in the i^{th}, j^{th} cell

$$\begin{gathered} \langle M(x, y, t_{n+1}) \rangle = \\ \frac{1}{\Delta x_{i,j} \Delta y_{i,j}} \\ \int_{x_{i-1/2,j}}^{x_{i+1/2,j}} \int_{y_{i,j-1/2}}^{y_{i,j+1/2}} \left[M(x, y, t_n) - \int_{t_{n+1}}^{t_n} \frac{\partial F}{\partial x} dt - \int_{t_{n+1}}^{t_n} \frac{\partial F}{\partial y} dt \right] dx dy. \end{gathered} \tag{A.5}$$

Expanding and rearranging yields

$$\begin{gathered} \langle M(x, y, t_{n+1}) \rangle = \\ \frac{1}{\Delta x_{i,j} \Delta y_{i,j}} \int_{x_{i-1/2,j}}^{x_{i+1/2,j}} \int_{y_{i,j-1/2}}^{y_{i,j+1/2}} M(x, y, t_n) dx dy \\ - \frac{1}{\Delta x_{i,j}} \int_{t_{n+1}}^{t_n} \left\{ \int_{x_{i-1/2,j}}^{x_{i+1/2,j}} \frac{\partial F}{\partial x} dx \right\} dt \\ - \frac{1}{\Delta y_{i,j}} \int_{t_{n+1}}^{t_n} \left\{ \int_{y_{i,j-1/2}}^{y_{i,j+1/2}} \frac{\partial F}{\partial y} dy \right\} dt \end{gathered} \tag{A.6}$$

Substituting Eq.(A.2) into Eq.(A.6) and rearranging, having evaluated the spacial term of Eq.(A.6) at the cell interfaces, gives

$$\begin{gathered} \langle M(x, y, t_{n+1}) \rangle - \langle M(x, y, t_n) \rangle = \\ - \frac{1}{\Delta x_{i,j}} \int_{t_{n+1}}^{t_n} \left\{ F_{i+1/2,j} - F_{i-1/2,j} \right\} dt - \frac{1}{\Delta y_{i,j}} \int_{t_{n+1}}^{t_n} \left\{ F_{i,j+1/2} - F_{i,j-1/2} \right\} dt \end{gathered} \tag{A.7}$$

where $F_{i+1/2,j}$, $F_{i-1/2,j}$, $F_{i,j+1/2}$ and $F_{i,j-1/2}$ are the fluxes evaluated at cell interfaces $(x_{i+1/2}, y_j)$, $(x_{i-1/2}, y_j)$, $(x_i, y_{j+1/2})$ and $(x_i, y_{j-1/2})$, respectively. Differentiating with respect to time provides the finite volume discretisation for an average rate of change of M in cell (i,j), as a result of the flux divergence across the cell

$$\frac{d\langle M_{i,j}\rangle}{dt} + \frac{1}{\Delta x_{i,j}}\Big\{F_{i+1/2,j} - F_{i-1/2,j}\Big\} + \frac{1}{\Delta y_{i,j}}\Big\{F_{i,j+1/2} - F_{i,j-1/2}\Big\} = 0 \qquad \text{(A.8)}$$

FVMs are an approach to spacially discretising PDEs. To acquire the numerical solution of the governing PDE, the temporal derivative of Eq.(A.8) must be integrated in time. We use `MATLAB`'s built-in `ODE` solvers to perform the time integration.

B

Matrix Diffusion

Time- and potential contributory-scale of pressure, solute and thermal diffusion into the EC rock matrix at investigated. Taking the porosity of a fracture network to be distributed among a set of planar fractures with aperture a [L] and spatial frequency f [L^{-1}], the block width is $H_B = f^{-1} = a/\phi_e$ (Figure B.1).

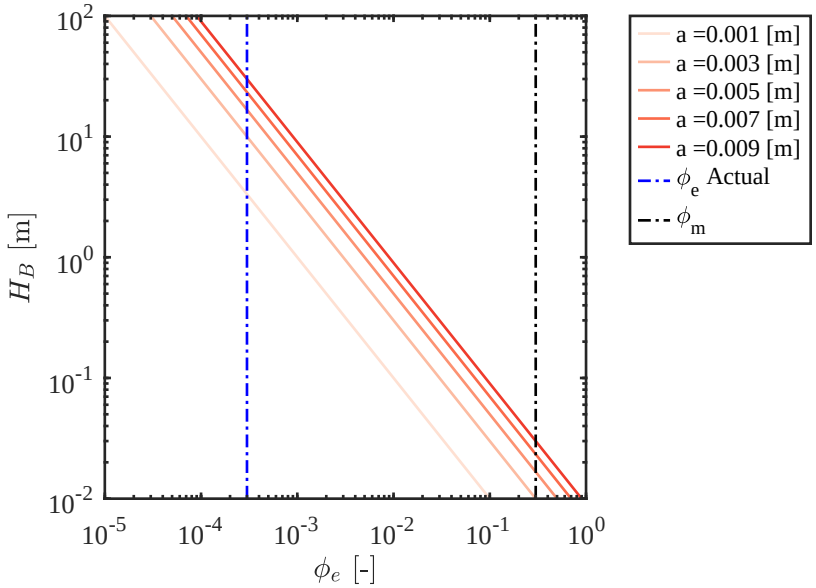

Figure B.1: Relationship between effective porosity, fracture aperture and effective width of matrix blocks (uniformly distributed over aquifer height). Calibrated ϕ_e and estimated ϕ_m shown.

A 1D model is constructed to simulate a block of rock matrix, bounded by fractures on either side (see Figure B.2 for illustration). Diffusion into the rock matrix can be expressed by the following continuity equation

$$\frac{\partial u}{\partial t} - D\frac{\partial u^2}{\partial x^2} = 0, \tag{B.1}$$

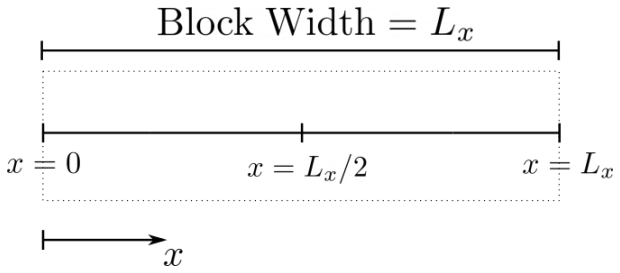

Figure B.2: Illustration of 1D matrix block domain

where u [$\mathrm{ML^{-1}T^{-2}}$, $\mathrm{ML^{-3}}$ or Θ] is the diffusive quantity being investigated, t [T] is time, x [L] is the distance in the x-axis of the matrix block, and D is the appropriate diffusivity. The selected diffusivities are expressed as

$$\begin{aligned} D_{hydro} &= \frac{k_h}{\mu\beta_t} = \frac{T}{S} = 1 \times 10^2 \\ D_{solute} &= 4.2 \times 10^{-10}, \\ D_{thermal} &= \frac{\lambda_m}{\rho_m c_m} = 4.8 \times 10^{-7} \end{aligned} \tag{B.2}$$

where D_{hydro} [$\mathrm{L^2T^{-1}}$] is the hydraulic diffusivity, β_t [$\mathrm{M^{-1}LT^2}$] is the total compressibility, D_{solute} [$\mathrm{L^2T^{-1}}$] is the molecular diffusivity of fluorescein (taken from Casalini et al. (2011)) and $D_{thermal}$ [$\mathrm{L^2T^{-1}}$] is the thermal diffusivity. The remaining parameters are defined in Sections 2.3, 3.2 and 4.2. The diffusion equation is subject to the following initial and boundary conditions:

$$\begin{aligned} u(x,0) &= 0 \\ u(0,t) &= u(L_x,t) = 1 \end{aligned} \tag{B.3}$$

where L_x [L] is the total width of a matrix block. We discretise the domain using a standard finite-volume method with $N = 500$ cells, and investigate $L_x = 1$ to 100 m. The point corresponding to the centre of the domain ($u(L_x/2,t)$) is monitored for 'half equilibrium'

$$t_{he} = t \quad \text{where} \quad u(L_x/2,t) = 0.5 \tag{B.4}$$

where t_{he} [T] is the 'half equilibrium' time. The results of the diffusive analysis are illustrated in Figure B.3. For $L_x = 3$ m, we observe approximate t_{he} of 0.01 seconds, 18 days and 18250 days for hydraulic, thermal and solute diffusivities, respectively. From these respectively time-scales, we infer the matrix diffusion within the hydraulic and solute models are suitable assumptions: hydraulic is sufficiently rapid to be expressed within the same continuum at the pressure diffusion of the fractures, and the solute diffusion is sufficiently slow to contribute negligible to the time-scale of the simulated tracer test. Given the time-scale of the thermal calibration and operational simulations (see Chapters 4 and 5) the results of the present analysis indicate rock matrix diffusion is a contributory thermal transport mechanism. Chapters 4 and 5 model rock matrix diffusion within a continuum but it remains to be seen whether this is a suitable approximation of transport behaviours and interactions within the fractured EC aquifer.

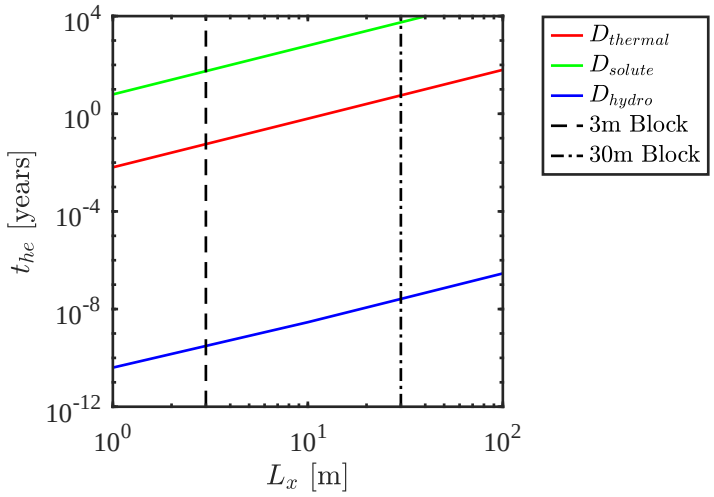

Figure B.3: Comparison of 'half equilibrium' rates as a function of block width and diffusivity. 3 m and 30 m sized blocks are marked